SOLAR PHOTOVOLTAIC PANEL AND ROOFING MATERIAL DETECTION USING WORLDVIEW-3 IMAGERY

by

Rakesh Kumar Mishra

MCA, U. P. Technical University, UP, India, 2005

A Dissertation Submitted in Partial Fulfillment
of the Requirements for the Degree of

Doctor of Philosophy

in the Graduate Academic Unit of Geodesy and Geomatics Engineering

Supervisor: Yun Zhang, PhD, Geodesy and Geomatics Eng.

Examining Board: David Coleman, PhD, Geodesy and Geomatics Eng.
Ian Church, PhD, Geodesy and Geomatics Eng.
Fan-Rui Meng, PhD, Forestry & Environment Mgt.

External Examiner: Jonathan Li, PhD, Department of Geography & Environmental Management, Faculty of Environment, University of Waterloo

This dissertation is accepted by the
Dean of Graduate Studies

THE UNIVERSITY OF NEW BRUNSWICK

August, 2017

©Rakesh K. Mishra, 2017

ABSTRACT

This PhD dissertation focuses on the development of new techniques to detect urban solar photovoltaic (PV) panel installations and roofing materials utilizing the commercially available WorldView-3 satellite imagery, consisting of 1 panchromatic (Pan) band with 0.3m resolution, 8 visible and near infrared (VNIR) bands with 1.2m resolution, and 8 short wave infrared (SWIR) spectral bands with 7.5m resolution. To accurately detect urban solar PV panels and roofing materials, it is necessary to analyze the spectral information in both the 8 VNIR bands and the 8 SWIR bands at the pixel level. However, the resolution difference between the VNIR bands and the SWIR bands is more than 6 times, which creates significant challenges for the spectral analysis and thus for the material detection. In order to increase the resolution of the SWIR bands from 7.5m to 1.2m, Fuze Go SWIR Sharp (FGSS) algorithm is used. The resulting high-resolution 1.2m SWIR bands are then combined with the original 1.2m VNIR bands to form a 16-band 1.2m (VNIR+SWIR) super spectral imagery. A method to detect solar PV panel installations and a method to detect roofing materials in the 16-band super spectral imagery are also developed.

In order to increase the resolution of WorldView-3 SWIR bands from 7.5m to 1.2m and take advantage of their capability for material identification, this research investigated the capacities of 9 popular, industry adopted pan-sharpening algorithms for pan-sharpening the WorldView-3 SWIR bands. The general principles of the pan-sharpening algorithms are reviewed. The WorldView-3 Pan images were down-sampled from 0.4m to 1.6m to fuse with the 7.5m SWIR image. Experiments demonstrate that the most commonly used algorithms are not suitable for pan-sharpening SWIR images, whereas the new pan-sharpening algorithm, Fuze Go SWIR Sharp (FGSS), can produce satisfactory results. The

reasons why most algorithms fail to produce quality pan-sharpened SWIR bands are also examined.

To detect solar PV panels, a new method is developed that can effectively analyze the spectral information in the newly formed high-resolution (HR) 16-band 1.2m super spectral (SS) imagery by adapting the spectral angle mapping (SAM) algorithm. The proposed method, named HR-SSF-SAM method, is tested on the WorldView-3 imagery of Brea, California, USA. The results demonstrate a true detection rate of 93.3% with 0% false detection. Even solar PV panels and glass roofs can be differentiated from each other.

To detect roofing materials, such as fiberglass, ethylene propylene diene monomer (EPDM), metal, and concrete, using WorldView-3 imagery, a novel method is proposed. The method utilizes the newly formed high-resolution 16-band 1.2m super spectral imagery and introduces a new approach to detect roofing materials. Experiments with the WorldView-3 imagery of Brea, California, USA, demonstrate that the proposed method achieves an overall accuracy of 97.59% and Kappa accuracy of 95.59% for roofing material detection in commercial areas, and an overall accuracy of 93.88% and Kappa accuracy of 88.98% for roofing material detection in residential areas with family houses.

Because of the complexity of using WorldView-3 imagery for solar PV panel detection and roofing material detection, very few publications can be found in this area. The literature review undertaken for this research confirms that the accuracies achieved are significantly better than those found in the literature.

DEDICATION

To my inspiring FATHER

To my lovely MOTHER

To my love of life RITA

And

My princess daughter PRIYA

ACKNOWLEDGEMENTS

This research has been accomplished by the help of several individuals and I would like to take this opportunity to thank them.

First, I would like to thank my supervisor Dr. Yun Zhang for providing research funding and his valuable guidance and advise throughout my PhD program. He taught me valuable lessons in research by patiently reviewing my papers, thesis, and presentations. Furthermore, he provided me many opportunities for teaching, attending conferences, industry R&D, and many other academic activities.

I am very grateful to Dr. David J. Coleman, Dr. Julian Meng, and Dr. Susan E. Nicolas, and for their help in my major and minor examinations, for reviewing my proposal, and dissertation.

I acknowledge Canada Research Chairs Program for providing financial support for this research. I would like to thank DigitalGlobe for providing me the WorldView-3 images used in this research.

Many thanks to staff at the Department of Geodesy and Geomatics Engineering, especially David Fraser, Sylvia Whitaker, and Lorry Hunt for their kind support. I would also like to thank the university writing centre, especially, Dr. Richard Spacek for his advice on my writing.

I am truly indebted to my family, especially my mother and father for their unconditional love, care, and motivation at every stage of my life.

Finally, I would like to thank my beautiful wife Rita and my princess daughter Priya for their unconditional love, understating, support, and patience during my PhD program.

Table of Contents

ABSTRACT ii
DEDICATION iv
ACKNOWLEDGEMENTS v
Table of Contents vi
List of Tables xi
List of Figures xiii
List of Symbols, Nomenclature or Abbreviations xix
Chapter 1 : INTRODUCTION 1
1.1 Dissertation Structure 2
1.2 Background 2
1.3 Selection of research topic 6
1.4 Review of existing solutions 7
1.4.1 WorldView-3 SWIR pan-sharpening 7
1.4.2 Solar PV panel detection 7
1.4.3 Roofing Material Detection 8
1.5 Problem statement 8
1.6 Research objectives 10
1.7 Data and Metrics 10
1.8 Overview of each chapter 12
1.9 References 14
Chapter 2 : Effects of Industry Adopted Fusion Methods on Pan-sharpening WorldView-3 SWIR Imagery 17

2.1 Introduction 18

2.2. Pan-sharpening algorithms 21

2.2.1 High Pass Filter (HPF) 21

2.2.2 Intensity-Hue-Saturation (IHS) 21

2.2.3 Principle Component Analysis (PCA) 21

2.2.4 Brovey 22

2.2.5 Wavelet 22

2.2.6 Gram Schmidt 22

2.2.7 Hyperspherical Color Space (HCS) 23

2.2.8 NNDiffuse 23

2.2.9 Fuze Go SWIR Sharp (FGSS) 23

2.3 SWIR fusion results 24

2.4 Quality evaluation and result analysis 25

2.4.1 Visual comparison 25

2.4.2 Statistical comparison 28

2.4.3 Result analysis 31

2.5 Conclusions 33

2.6 Acknowledgement 34

2.7 References 34

Chapter 3 : Solar Photovoltaic Panel Detection using WorldView-3 satellite imagery 38
3.1 Introduction 39
3.2 Study area and data set 42
3.3 Spatial and spectral information of the SWIR bands 44
3.3.1 Spatial resolution of the SWIR bands 44
3.3.2 Spectral analysis of solar PV panels 45
3.4 Methodology of solar PV panel detection 49
3.4.1 High-Resolution SWIR bands creation 50
3.4.2 Super spectral image formation 53
3.4.3 Solar PV panel detection 53
3.5 Results and discussions 55
3.5.1 Ground truth collection 55
3.5.2 Solar PV panel detection results 56
3.5.3 Methods for accuracy calculation 58
3.5.4 Accuracy comparison and analysis 59
3.6 Conclusions 62
3.7 Acknowledgement 63
3.8 References 64
Chapter 4 : Roofing Material Detection using WorldView-3 Satellite Imagery 66
4.1 Introduction 67

4.2 Study area and data set 70

4.3 Potential and limitation of VNIR and SWIR bands for roofing material detection 73

4.3.1 Spatial resolution of the SWIR bands 73

4.3.2 Spectral analysis of roofing materials 74

4.4 Methodology of roofing material detection 78

4.4.1 SNRO image creation 80

4.4.2 Super spectral image formation 83

4.4.3 Roofing material detection 86

4.5 Results and discussions 96

4.5.1 Ground truth collection 96

4.5.2 Roofing material detection results 98

4.5.3 Accuracy comparison and analysis 102

4.6 Conclusions 108

4.7 Acknowledgement 110

4.8 References 110

Chapter 5 : SUMMARY AND CONCLUSIONS 114

5.1 Summary of research 114

5.1.1 Chapter 2 114

5.1.2 Chapter 3 115

5.1.3 Chapter 4 115

5.2 Achievements of the research 115

5.2.1 WorldView-3 SWIR bands pan-sharpening 115

5.2.2 Solar PV panel detection 116

5.2.3 Roofing material detection 116

5.3 Suggestions for future work 117

5.3.1 Agriculture 117

5.3.2 Forestry 118

5.3.3 Mining/Geology 118

Appendix I From UNB PanSharp to Fuze Go – the success behind the pansharpening algorithm 119

Appendix II A review of optical imagery and airborne LiDAR data registration methods 147

Curriculum Vitae

List of Tables

Table 1-1 Characteristics of the WorldView-3 imagery 5

Table 1-2 Data and Metrics used for accuracy assessment 11

Table 2-1 Characteristics of the Pan, VNIR, and SWIR sensors of WV-3 satellite 20

Table 2-2 Interpolation methods used in different pan-sharpening methods 24

Table 2-3 Quality ranking of visual comparison 28

Table 2-4 Statistical comparison results 31

Table 3-1 Characteristics of the WorldView-3 imagery used in this study. 43

Table 3-2 The total number of pixels of the study area and the number of training pixels used in the solar PV panel detection from the original 1.2m VNIR, original 7.5m SWIR, produced 1.2m HR SWIR and combined 1.2m super spectral bands 55

Table 3-3 Solar PV panel detection results using original SWIR bands, HR SWIR bands, and super spectral bands. 59

Table 4-1 Characteristics of the WorldView-3 imagery used in this study. 72

Table 4-2 Jeffries-Matusita distance and Transformed Divergence separability measurements among different roofing materials ROI pixels. 89

Table 4-3 Total number of pixels of the study area and the number of ROI pixels used to generate reference spectrums of roofing materials and non-target materials from the original 1.2m VNIR, original 7.5m SWIR, and 1.2m super spectral bands. 95

Table 4-4 The total number of different roofing materials identified in the two test areas. 98

Table 4-5 PA, UA, OA, and Kappa of the Test Area-1 for VNIR bands, original SWIR bands, HR SWIR bands, super spectral bands and, the proposed method 103

Table 4-6 PA, UA, OA, and Kappa of the Test Area-2 for VNIR bands, original SWIR bands, HR SWIR bands, super spectral bands and, the proposed method..... 104

Table 4-7. Non-roofing object detection rates (NRODR) of the Test Area-1 and Test Area-2 for VNIR bands, original SWIR bands, HR SWIR bands, super spectral bands and, the proposed methods. 105

List of Figures

Figure 1.1 Organization of this dissertation..... 2

Figure 1.2 Two roofs (with different materials) in visible and SWIR bands of WorldView-3 imagery. (a) 1.2m VNIR bands 5, 3, 2 displayed in RGB at 1:1 ratio, (b) enlarged 7.5m SWIR bands 2, 1, 8 displayed in RGB. Roof-1 and Roof-2 are made with different materials. They have similar colors in visible bands; but, different colors in SWIR bands..... 6

Figure 2.1 Comparison between the original VNIR (1.6m), Pan (down-sampled to 1.6m), SWIR (7.5m) WV-3 images and the pan-sharped (1.6m) WV-3 images from different pan-sharpening algorithms (2 times enlarged subset). 26

Figure 2.2 Comparison of different band combinations of the original (7.5m) and FGSS pan-sharpened (1.6m) WV-3 SWIR images..... 26

Figure 3.1 Study area and a subsection with solar PV panels. (a) Overview of the study area in the 1.2m natural colour image of WorldView-3, and (b) solar PV panels (1), dark roofs (2), and a glass roof (3). 42

Figure 3.2 Solar PV panels in different spectral images of WorldView-3. (a) Available 7.5m SWIR bands 2, 1, 8 displayed in RGB at 1:1 ratio, (b) enlarged 7.5m SWIR bands, and (c) original 1.2m VNIR bands 5, 3, 2 displayed in RGB. (In the available SWIR bands small solar PV panel installations are not visible; however, they are clearly visible in the original VNIR bands.) 45

Figure 3.3 Comparison of the spectrums of a solar PV panel, dark roofs and a glass roof in VNIR and SWIR bands. (a) (b) (c) (d) solar PV panel, dark roof 1, dark roof 2, and glass roof in VNIR bands respectively, (e) the spectral curves of the pixels a,

b, c, and d (centtres of the crosses) in VNIR bands, (f) (g) (h) (i) solar PV panel, dark roof 1, dark roof 2, and glass roof in SWIR bands respectively, and (j) the spectral curves of the pixels f, g, h and i in SWIR bands. (The SWIR bands shown here are 1.2m high-resolution SWIR bands produced using Fuze Go SWIR Sharp to be discussed in the methodology section. The spectrums of solar PV panel, dark roof, and glass roof are similar in VNIR bands, but different in SWIR bands.)..... 46
Figure 3.4 Comparison of the spectrums of a solar PV panel and white roofs in VNIR and SWIR bands. (a) (b) (c) solar PV panel, white roof-1, white roof-2 in VNIR bands respectively, (d) the spectral curves of the solar PV panel pixel (centre of the cross) and the two white roof pixels in VNIR bands, (e) (f) (g) solar PV panel, white roof-1, white roof-2 in SWIR bands respectively, (h) the spectral curves of the solar PV panel pixel and the two white roof pixels in SWIR bands, and (i) the spectral curves of the solar PV panel pixel and the two white roof pixels in the 16 spectral bands (8 VNIR + 8 SWIR). (The solar PV panel and white roofs have similar spectral curves in SWIR bands, whereas they have different spectral curves in VNIR bands.)..... 48
Figure 3.5 Flowchart of the proposed HR-SSF-SAM method for solar PV panel detection. 50
Figure 3.6 Comparison between the available 7.5m SWIR image (a), the 1.2m HR SWIR image generated using FGSS (b), and the original 1.2m VNIR image (c). 52
Figure 3.7 Solar PV panel detection results and the comparison (red: detected solar PV panels; yellow circle: missed detection; blue circle: false detection). (a) Solar PV panel detected using the proposed HR-SSF-SAM method, (b) subsection of

Solar PV panel detected using VNIR bands, (c) subsection of solar PV panel detected using original (7.5m) SWIR bands, (d) subsection of solar PV panel detected using HR (1.2m) SWIR bands, and (e) subsection of solar PV panel detected using the proposed HR-SSF-SAM method in 16 super spectral (1.2m) bands. (SAM algorithm was used in all of the detections) 57

Figure 3.8 Comparison of solar PV panel true detection, miss detection, and false detection rates using VNIR 1.2m, original 7.5m SWIR, HR 1.2m SWIR and 16 super spectral 1.2m bands (HR-SSF-SAM method) respectively. 61

Figure 3.9 Glass roofs of Brea mall, Brea California. (a) 0.5m pan-sharpened natural color WorldView-3 image, (b) 3D view of the roof top in Google Earth image. 62

Figure 4.1 Study area and subsections with commercial and residential buildings. (a) Overview of the study area in the 1.2m natural colour image of WorldView-3, and (b) an enlargement showing the commercial and residential buildings. 71

Figure 4.2 Roofs in different spectral images of WorldView-3. (a) Available 7.5m SWIR bands 2, 1, 8 displayed in RGB at 1:1 ratio, (b) enlarged 7.5m SWIR bands, and (c) original 1.2m VNIR bands 5, 3, 2 displayed in RGB. (Small roofs are not visible in the available SWIR bands; however, they are clearly visible in the original VNIR bands.) 74

Figure 4.3 Comparisons of the spectrums of a fiberglass roof, a EPDM roof, a metal roof, and a concrete roof in VNIR and SWIR bands. (a) (b) (c) (d) fiberglass roof, EPDM roof, metal roof, and concrete roof in VNIR bands respectively, (e) the spectral curves of the pixels a, b, c, and d (centres of the crosses) in VNIR bands, (f) (g) (h) (i) fiberglass roof, EPDM roof, metal roof, and concrete roof in SWIR

bands respectively, and (j) the spectral curves of the pixels f, g, h and i (centres of the crosses) in SWIR bands. (The SWIR bands are 1.2m high-resolution SWIR bands produced using Fuze Go SWIR Sharp to be discussed in the methodology section. The spectrums of fiberglass roof, EPDM roof, metal roof, and concrete roof are similar in VNIR bands; but different in SWIR bands.)..... 76
Figure 4.4 Comparison of the spectrums of a road and a concretes roof in VNIR and SWIR bands. (a) and (b) road and concrete roof in VNIR bands respectively, (c) the spectral curves of the road pixel (centre of the cross) and the concrete roof pixels in VNIR bands, (d) and (e) road and concrete roof in SWIR bands respectively, (f) the spectral curves of the road and the concrete roof pixels in SWIR bands. (The road and the concrete roof have similar spectral curves in SWIR bands, whereas they have different spectral curves in VNIR bands.)..... 77
Figure 4.5 Flowchart of the proposed method for roofing material detection..... 79
Figure 4.6 Spectral angle between reference and test spectrums for a two-band image (Kruse et al., 1993)..... 81
Figure 4.7 SNRO image created using VNIR bands. Most of the non-roofing objects are suppressed in the SNRO image..... 83
Figure 4.8 Comparison between the available 7.5m SWIR image (a), the 1.2m HR SWIR image generated using FGSS (b), and the original 1.2m VNIR image (c). 85
Figure 4.9 Reference spectrums produced from the ROI pixels in the super spectral bands. 87
Figure 4.10 Comparison of the spectrums of a concrete roof, road and barren land in super spectral bands. (a) (b) (c) concrete roof, road, and bare earth in super

spectral bands respectively, (d) the spectral curves of the pixels a, b, and c (centres of the crosses) in super spectral bands. (The spectrums of concrete roof, road, and bare earth are similar in super spectral bands.) 90
Figure 4.11 Non-target reference spectrums produced from the ROI pixels of the non-target objects (road and bare earth). 91
Figure 4.12 Modified super spectral image 92
Figure 4.13 Texture and color of different roofing materials and ground truth image of two test areas. (a) textures of different types of roofing materials in the Test Area-1 (commercial) and ground truth image; (b) textures of different types of roofing materials in the Test Area -2 (residential) area and ground truth image. 97
Figure 4.14 Roofing material detection results and the comparison for the study area-1 (commercial buildings). (a) RGB image of the study area-1, (b) roofing materials detected using VNIR bands, (c) roofing materials detected using original (7,5m) SWIR bands, (d) roofing materials detected using HR (1.2m) SWIR bands, (e) roofing materials detected using 16 super spectral (1.2m) bands, and (f) roofing materials detected using the proposed framework. Results shown in (b), (c), (d), and e) were generated using the SAM algorithm; the result shown in (f) were generated using the proposed method. 99
Figure 4.15 Roofing material detection results and the comparison for the study area-2 (residential buildings). (a) RGB image of the study area-1, (b) roofing materials detected using VNIR bands, (c) roofing materials detected using original (7,5m) SWIR bands, (d) roofing materials detected using HR (1.2m) SWIR bands, (e) roofing materials detected using 16 super spectral (1.2m) bands, and (f) roofing

materials detected using the proposed framework. Results shown in (b), (c), (d), and e) were generated using the SAM algorithm, and the result shown in (f) was generated using the proposed method. 101

Figure 4.16 Comparison of overall accuracy and Kappa coefficients of roofing material detection in test area-1 (a) and test area-2 (b) using VNIR 1.2m, original 7.5m SWIR, HR 1.2m SWIR, 16 super spectral 1.2m bands and proposed method respectively. 108

List of Symbols, Nomenclature or Abbreviations

CSI: California Solar Initiative

EMS: Electromagnetic spectrum

EPDM: Ethylene propylene diene monomer

FDR: False detection rate

FGSS: Fuze Go SWIR Sharp

HCS: Hyperspectral Color Space

HR: High-resolution

HR-SSF-SAM: High-resolution, super spectral formation and spectral angle mapping

IHS: Intensity, hue, saturation

Int.Q: Integration quality

KC: Kappa coefficient

MDR: Missed detection rate

MS: Multispectral

NFD: Number of false detections

NMD: Number of missed detections

NRODR: Non-roofing object detection rate

NTD: Number of true detections

OA: Overall accuracy

PA: Producer accuracy

Pan: Panchromatic

PCA: Principal component analysis

PV: Photovoltaic

QUAC: Quick atmospheric correction

RGB: Red, Green, Blue

RMSE: Root-mean-square error

ROI: Region of interest

SAM: Spectral Angle Mapper

SNRO: Suppressed non-roofing objects

Spa.Q: Spatial quality

Spe.Q: Spectral quality

SS: Super spectral

SSI: Super spectral image

SSIM: Structural Similarity Index

SWIR: Short wave infrared

TD: Total number of detections

TDR: True detection rate

UA: User accuracy

VHR: Very high-resolution

VNIR: Visible and near infrared

WV-3: WorldView-3

Chapter 1 : INTRODUCTION

This PhD dissertation presents solutions for detecting solar photovoltaic (PV) panels and roofing materials in an urban environment using WorldView-3 imagery. This is an article-based dissertation which contains the following three papers:

Paper 1 (Peer Reviewed):

Mishra, R. K. and Y. Zhang (2017), Effects of industry adopted fusion methods on pan-sharpening WorldView-3 short wave infrared (SWIR) imagery, *Journal of Applied Remote Sensing - Letters* (under review)

Paper 2 (Peer Reviewed):

Mishra, R. K. and Y. Zhang (2017), Solar photovoltaic panel detection using WorldView-3 satellite imagery, *Journal of Photogrammetric Engineering & Remote Sensing* (under review)

Paper 3 (Peer Reviewed):

Mishra, R. K. and Y. Zhang (2017), Roofing material detection using WorldView-3 satellite imagery, *International Journal of Remote Sensing* (under review)

1.1 Dissertation Structure

This article-based dissertation consists of five chapters. Three peer reviewed journal papers are incorporated in the dissertation, which are under review. Chapter 1 provides an introduction to the research, chapters 2 to 4 present the three journal papers. Finally, Chapter 5 presents the summary of the work and conclusions. **Figure 1.1** illustrates the organization of this dissertation.

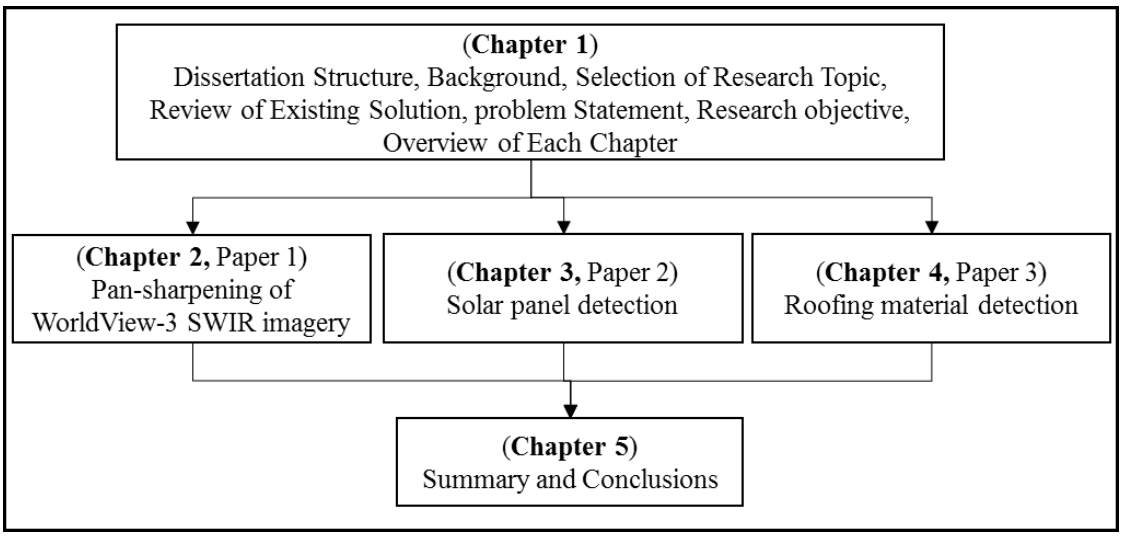

Figure 1.1 Organization of this dissertation

1.2 Background

In recent years, there has been rapid growth of solar PV panel installations around the world because of the technical advancement in PV and battery technologies, fast reduction in prices of solar PV panels, and government subsidies and encouragements for green energy. Hence, small scale solar power generation is quickly becoming a viable alternative to conventional sources of electricity. A report from the California Solar Initiative (CSI) shows that, in California alone the solar PV capacity has increased 12 times in the years

from 2006 to 2014 (Hallock and Kinman, 2015). Therefore, it is important to acquire information about solar PV panel installations, such as the number of solar PV panels installed in an area of interest. This information is crucial in quantifying the energy production of existing solar PV panels in order to make informed decisions, such as energy policies and regulations, system planning for capacity expansion, transmission and distribution upgrades, and operation adjustments to ensure grid reliability and resilience (Malof et al., 2015). However, the traditional methods, such as on-site surveys and information collection from solar PV vendors, are laborious, time consuming, and often yield insufficient data for government and utility decision makers. In addition, the data collected by traditional methods may quickly become outdated due to the rapid growth of solar PV installations. To overcome these challenges, there is a need for new technologies that can obtain accurate information on solar PV panel installation and distribution in a cost-effective fashion.

Urban areas have been rapidly growing in the last few decades around the world. Urban areas normally consist of a large variety land covers with different man-made and natural materials which influence the environment, climate, and energy conditions of a region (Taherzadeh and Shafri, 2013). Roofing materials are some of the important land covers that affect the environment and even the safety of an urban area. For example, information about roofing material is important for various applications such as determining fire prone areas, water flows, disaster preparedness, and pollution sources. In the fire prone areas, insurance companies need to know the roofing materials for their flammability. Hence, detection of roofing materials is one of the important tasks for urban management and planning. However, conventional on-site surveys for roofing material detection are

expensive, time consuming, and slower in coping with new construction. They are not practical for detecting roofing materials of a large area. Therefore, remote sensing technologies have become an attractive option for detecting roofing materials.

The launch of WorldView-3 satellite on August 13, 2014, brings new opportunities for solar PV panel and roofing material detection because it is the first high-resolution satellite to include 8 short wave infrared (SWIR) bands, 8 visible and near infrared (VNIR) bands, and 1 panchromatic (Pan) band in the data collection (DigitalGlobe, 2016a). **Table 1-1** shows the characteristics of the WorldView-3 imagery. The SWIR region of the electromagnetic spectrum (EMS) refers to non-visible light falling roughly between 1100nm and 3000nm. The availability of 8 SWIR bands, which capture the unique spectral signatures of certain ground materials, has opened up new opportunities for more high-resolution information extraction. In addition, because VNIR and SWIR bands measure the spectral information of different physical phenomena of the ground materials, the combination of VNIR and SWIR bands may offer additional information for solar PV panel and roofing material detections.

However, as shown in **Table 1-1**, the resolution of commercially available WorldView-3 SWIR bands is only 7.5m which is not sufficient for detecting small size solar PV panels and roofing materials of residential buildings. On the other hand, the resolution difference between the available WorldView-3 VNIR bands (1.24m) and SWIR bands (7.5m) is greater than a factor of 6. This large resolution difference makes it difficult to combine the VNIR and SWIR bands for effective and accurate spectral analyses. These opportunities and challenges motivate us to develop new methods to detect solar PV panels and roofing materials in an urban environment.

Table 1-1 Characteristics of the WorldView-3 imagery

Band		Spectral range (nm)	Spatial resolution (m)
	Pan	450 - 800	0.31
VNIR	Coastal	400 - 450	1.24
	Blue	450 - 510	1.24
	Green	510 - 580	1.24
	Yellow	585 - 625	1.24
	Red	630 - 690	1.24
	Red Edge	705 - 745	1.24
	NIR-1	770 - 895	1.24
	NIR-2	860 - 1040	1.24
SWIR	SWIR-1	1195 - 1225	7.5
	SWIR-2	1550 - 1590	7.5
	SWIR-3	1640 - 1680	7.5
	SWIR-4	1710 - 1750	7.5
	SWIR-5	2145 - 2185	7.5
	SWIR-6	2185 - 2225	7.5
	SWIR-7	2235 - 2285	7.5
	SWIR-8	2295 - 2365	7.5

1.3 Selection of research topic

Because of the unique way that many materials reflect in the SWIR EMS, it is often possible to discriminate among different materials which is not possible with reflectance only in the VNIR EMS. For example, as shown in **Figure 1.2**, Roof-1 and Roof-2 which are made with different materials have similar reflectance in the WorldView-3 visible bands; however, they are different in WorldView-3 SWIR bands. Therefore, WorldView-3 SWIR bands can be used to detect important land cover materials such as solar PV panels and roofing materials. However, the major challenge is the coarser resolution (7.5m) of the commercially available WorldView-3 SWIR bands which is not sufficient to identify small size solar PV panels and roofing materials of small size roofs because of the spectral mixing in the large size SWIR pixels.

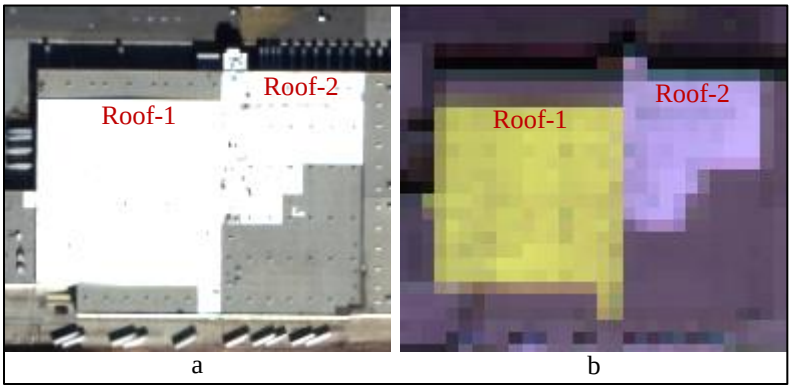

Figure 1.2 Two roofs (with different materials) in visible and SWIR bands of WorldView-3 imagery. (a) 1.2m VNIR bands 5, 3, 2 displayed in RGB at 1:1 ratio, (b) enlarged 7.5m SWIR bands 2, 1, 8 displayed in RGB. Roof-1 and Roof-2 are made with different materials. They have similar colors in visible bands; but, different colors in SWIR bands.

Therefore, this research intends to find a solution to increase the resolution of SWIR bands from 7.5m to 1.24m (equal to the resolution of VNIR bands) and develop new

methods to detect solar PV panels and roofing materials using the combined 1.24m VNIR and SWIR bands.

1.4 Review of existing solutions

1.4.1 WorldView-3 SWIR pan-sharpening

In order to utilize WorldView-3 VNIR and SWIR bands for solar PV panel and roofing material detections, there is a need to increase the resolution of SWIR bands equal to the VNIR bands. In the past, several pan-sharpening algorithms have been developed to increase the resolution of multispectral/VNIR bands. Also, several publications (Nikolakopoulos, 2008; Padwick et al., 2010; Zhang and Mishra, 2012; and Mercovich, 2015) have reported the qualities of popular algorithms for pan-sharpening VNIR images. However, in the literature review, no algorithm has been found that can increase the resolution of SWIR bands.

1.4.2 Solar PV panel detection

With the recent advancement of earth imaging satellite sensors, researchers have attempted to identify solar PV panels using high-resolution color satellite images. However, manual interpretation is time consuming, and it is difficult to differentiate solar PV panels from roofs with similar color. Malof et al. (2015) did a feasibility study, where a computer vision algorithm was tested to detect solar PV panels in a very high-resolution, visible (RGB) imagery. Only limited success was achieved, because the spectral information of solar PV panels is similar to that of dark roofs, parking lots, and roads.

1.4.3 Roofing Material Detection

Because most of the roofing materials have unique spectral signatures which can be recorded by hyperspectral bands, research has explored the potential of using hyperspectral data (including field spectroscopy data and hyperspectral imagery) for roofing material detection. For example, Cilia et al. (2015) used aerial hyperspectral images to detect asbestos cement roofs and their weathering status. Hamedianfar et al. (2014) combined data mining and object-based analysis together to classify urban surface materials in aerial hyperspectral images. Samsudin et al. (2016) applied feature selection algorithms to field spectroscopy data to detect roofing materials. These studies indicated that although aerial hyperspectral imagery and field spectroscopy data provide the best possible spatial and spectral resolutions for detecting roofing materials, they are expensive and have a limited ground coverage, compared to very high-resolution (VHR) satellite imagery.

Some research (Taherzadeh and Shafri, 2013; Taherzadeh and Shafri, 2014; Taherzadeh and Shafri, 2015; Taherzadeh and Shafri, 2016) utilized the state-of-the-art object-based classification methods to detect roofing materials in VHR satellite imagery. However, very limited success was achieved with high miss-classification errors, due to the lack of necessary spectral information in VHR multispectral imagery.

1.5 Problem statement

From the literature, it can be inferred that the remote sensing technologies can offer an efficient and cost-effective solution to detect solar PV panel installations and roofing materials in an urban environment. However, most of the VHR satellite imagery lacks necessary spectral information to differentiate solar PV panels and roofing materials from

other land cover objects. Aerial hyperspectral imagery and spectrometer data can provide necessary spatial and spectral information to detect roofing materials; however, they are expensive and have a limited ground coverage, compared to the VHR satellite imagery. The recently launched VHR satellite, WorldView-3, with additional 8 SWIR bands can be useful for solar PV panel and roofing material detection. However, the following specific problems were identified in solar PV panel and roofing material detections using WorldView-3 imagery.

a. SWIR bands with 7.5m resolution are not sufficient to effectively detect solar PV panels and roofing materials in an urban environment; a higher resolution SWIR bands are desired.
b. The experiments conducted for this research revealed that the spectral information in the SWIR bands is not sufficient to separate solar PV panels from some building roofs that have certain special materials.
c. The experiments conducted for this research revealed that the spectral information in the SWIR bands is not sufficient to separate roofing materials from some non-roof materials such as roads and parking lots.
d. The VNIR bands of WorldView-3 have a resolution of 1.2m, which is more than 6 times higher than that of the available SWIR bands. Therefore, it is not only difficult to detect solar PV panels and roofing materials using either the original VNIR bands or the available SWIR bands; but also difficult to combine the VNIR bands and the SWIR bands to collectively detect solar PV panels and roofing materials.

e. The experiments conducted for this research revealed that there are a few land cover objects such as roads and bare earth which have similar reflectance to that of some building roofs in both VNIR and SWIR bands.

This PhD dissertation covers the aforementioned problems and they are addressed in three journal papers mentioned in section 1.1.

1.6 Research objectives

The objectives of this research are to provide effective solutions to the problems mentioned in the section 1.5 that include:

a. Find an effective solution to increase the resolution of WorldView-3 SWIR bands from 7.5m to 1.2m (equal to the VNIR bands) and form a 16 band 1.2m super spectral imagery by combining 1.2m VNIR bands and 1.2m SWIR bands.
b. To develop a novel method to detect solar PV panel installations with more than 90% accuracy using WorldView-3 imagery.
c. To develop a novel method to detect four types (fiberglass, ethylene propylene diene monomer (EPDM), metal, and concrete) of roofing materials in an urban environment with more than 90% accuracy using WorldView-3 imagery.

1.7 Data and Metrics

The data and metrics used to evaluate methods presented in chapters 2 to 4 are summarized in **Table 1-2.**

Table 1-2 Data and Metrics used for accuracy assessment

No.	Data	Metrics Descriptions	Chapter
1.	WorldView-3 images covering 88 km^2 of Sebastopol, Ukraine, Europe. Pan GSD is 0.4m, VNIR GSD is 1.6m and SWIR GSD is 7.5m. Image acquisition date: October, 2014.	Spectral and spatial quality of each pan-sharpening method was evaluated both visually and most commonly used statistical evaluation methods such as ERGAS, SAM, Q, Q-8, and SSIM	Chapter 2[Mishra and Zhang, 2017]
2.	WorldView-3 imagery covering 20 km^2 of Brea, California, USA. Pan GSD is 0.5m, VNIR GSD is 1.2m and SWIR GSD is 7.5m. Image acquisition date: November, 2014.	The accuracy assessment of solar PV panel detection was done using True Detection Rate(TDR), Missed detection (MDR), and False Detection Rate (FDR) formulas. The ground truth was collected using Google Earth imagery (5cm spatial resolution).	Chapter 3[Mishra and Zhang, 2017]
3.	WorldView-3 imagery covering 20 km^2 of Brea, California, USA. Pan GSD is 0.5m, VNIR GSD is 1.2m and SWIR GSD is 7.5m. Image acquisition date: November, 2014.	The accuracy assessment of roofing material detections was done using the conventional error matrix and it elements including producer accuracy (PA), user accuracy (UA), overall accuracy (OA), kappa coefficient (KC), and non-roofing object detection rate (NRODR). The ground truth was collected using Google Earth imagery (5cm spatial resolution) and Google Street view.	Chapter 3[Mishra and Zhang, 2017]

1.8 Overview of each chapter

- **Chapter 1** is an introduction to this dissertation presenting a background of the study, selection of research topic, review of the existing solutions, statement of the problem, objectives of the study, and an overview of each chapter.
- **Chapters 2 to 5** comprise the three journal papers of this dissertation with the main contributions of this research included.
    - **Chapter 2** investigates the capacities of nine popular pan-sharpening algorithms adopted by industry for improving the resolution of WorldView-3 SWIR bands from 7.5m to 1.2m (equal to the resolution of the VNIR bands). A solution to increase the resolution of SWIR bands from 7.5m to 1.2m is proposed. The outcome of this research provides useful information to remote sensing researchers and practitioners for effectively utilizing WorldView-3 SWIR bands for advanced remote sensing applications.

      Note: Resolution of the WorldView-3 VNIR bands used in chapter-2 (paper-1) was 1.6m, therefore, resolution of the WorldView-3 SWIR bands was increased from 7.5m to 1.6m.
    - **Chapter 3** presents a high resolution, super spectral formation, and spectral angle mapping (HR-SSF-SAM) integrated method for solar PV panel detection using WorldView-3 imagery. First, the resolution of the 8 SWIR bands is increased from 7.5m to 1.2m using the Fuze Go SWIR Sharp algorithm. Then, the 8 1.2m SWIR bands are integrated with the 8 1.2m

VNIR bands to form a 16-band 1.2m super spectral image. At the end, the Spectral Angle Mapper (SAM) algorithm is adapted to identify solar PV panels in the 16-band super spectral image. The proposed HR-SSF-SAM method is tested on the WorldView-3 image of the Brea city, California, USA. The results demonstrate that a true detection rate of 93.3% is achieved with a 0% false detection rate. Even solar PV panels and glass roofs can be differentiated from each other.

- **Chapter 4** presents a novel method to detect four types of common roofing materials (fiberglass, ethylene propylene diene monomer (EPDM), metal, and concrete) using WorldView-3 imagery. To suppress non-roofing objects such as roads and parking lots, a suppressed non-roofing objects (SNRO) image is created using VNIR bands. Whereas, to solve the coarse-resolution problem of the available SWIR bands and spectral limitations of either the VNIR bands or the SWIR bands for roofing material detection, the Fuze Go SWIR Sharp algorithm (Fuze Go, 2016) is utilized to increase the resolution from 7.5m to 1.2m, and the 8 original 1.2m VNIR bands are integrated together with the 8 new 1.2m SWIR bands to form a 16-band 1.2m super spectral image set. Finally, SAM algorithm is modified to detect roofing materials by utilizing SNRO image, super spectral imagery, reference spectrums, and non-target reference spectrums. The proposed method was tested using WorldView-3 imagery over the city Brea, California, USA. A commercial area and a residential area were chosen to test the effectiveness of the proposed method. For the commercial area, the

overall accuracy and Kappa coefficient of 97.59% and 95.59 respectively were achieved; whereas, for the residential area, overall accuracy and Kappa coefficient of 93.99% and 88.98%respectively were achieved.

- **Chapter 5** presents the summary of the work accomplished in this research, concluding remarks, contributions of the research, and the future work.

1.9 References

Cilia, C., Panigada, C., Rossini, M., Candiani, G., Pepe, M., & Colombo, R. (2015). Mapping of asbestos cement roofs and their weathering status using hyperspectral aerial images. *ISPRS Journal of Photogrammetry and Remote Sensing* 4(2), 928–941.

DigitalGlobe, Inc. Exploring the benefits of SWIR satellite imagery, white paper. Accessed 22 February 2017: http://global.digitalglobe.com/sites/default/files/DG_SWIR_WP.pdf

DigitalGlobe, Inc. Moving from Pixels to Products… and data to insight, white paper. Accessed 22 February 2017: http://global.digitalglobe.com/sites/default/files/DG_Pixels_to_Products_forWeb.pdf

Hallock, L., Kinman, M., (2015). California's Solar Suc- cess Story: How the Million Solar Roofs Initiative Trans-formed the State's Solar Energy Landscape. *Environment California report*.

Hamedianfar, A., & Shafri, H. Z. M. (2014). Development of fuzzy rule-based parameters for urban object-oriented classification using very high resolution imagery. *Geocarto International.* 29(3), 268–292.

Hamedianfar, A., & Shafri, H. Z. M. (2015). Detailed intra-urban mapping through transferable OBIA rule sets using WorldView-2 very-high-resolution satellite images. *International Journal of Remote Sensing*. 36(13), 3380–3396.

Hamedianfar, A., & Shafri, H. Z. M. (2016). Integrated approach using data mining-based decision tree and object-based image analysis for high-resolution urban mapping of WorldView- 2 satellite sensor data. *Journal of Applied Remote Sensing*, 10(2), 025001.

Malof, J. M., Rui Hou., Collins, L. M., Bradbury, K., and Newell, R. (2015). Automatic solar photovoltaic panel detection in satellite imagery. *International Conference on Renewable Energy Research and Applications (ICRERA)*, Palermo. 1428-1431.

Marchisio, G. (2014). An Overview of the WorldView-3 Sensor. Geospatial World Forum, *Centre International Conference, Geneva, Switzerland*. May 05-09. Accessed 10 June 2017. https://geospatialworldforum.org/2014/presentation/Sensors/WGF%202014b%20-%20Giovanni%20Marchisio%20-%20DigitalGlobe_PDF.pdf

Nikolakopoulos, K. G. (2008). Comparison of nine fusion techniques for very high resolution data. *Photogrammetric Engineering & Remote Sensing*, 74 (5), 647–659.

Padwick, C., Deskevich, M., Pacifici, F. and Smallwood, S. (2010). Worldview-2 Pansharpening. *Proceedings of the American Society for Photogrammetry and Remote Sensing Annual Conference*, San Diego, CA. April 26–30.

Samsudin, S. H., Helmi, Z. M., Shafri & Hamedianfar, A. (2016). Development of spectral indices for roofing material condition status detection using field spectroscopy and WorldView-3 data. *Journal of Applied Remote Sensing*, 10(2), 025021.

Taherzadeh, E., & Shafri, H. Z. M. (2013). Development of a generic model for the detection of roof materials based on an object-based approach using WorldView-2 satellite imagery. *Advanced Remote Sensing*, 2(4), 312–321.

Taherzadeh, E., & Shafri, H. Z. M. (2013). Development of a generic model for the detection of roof materials based on an object-based approach using WorldView-2 satellite imagery. *Advanced Remote Sensing*, 2(4), 312–321.

Zhang, Y., & Mishra, R. K. (2012). A review and comparison of commercially available pan-sharpening techniques for high resolution satellite image fusion. Proceedings of the *IEEE International Geoscience and Remote Sensing Symposium*, Munich, July 22-27.

Chapter 2 : Effects of Industry Adopted Fusion Methods on Pan-sharpening WorldView-3 SWIR Imagery

Abstract

The launch of the WorldView-3 (WV-3) in August 2014 opened up new opportunities to use short wave infrared (SWIR) spectral bands for advanced and detailed remote sensing applications, which are beyond the capacity of visible and near infrared (VNIR) spectral bands. WV-3 SWIR sensor captures eight spectral bands with 3.7 m resolution; however, the commercially available resolution is limited to 7.5 m. In order to take advantage of the SWIR bands for their unique applications, such as smoke penetration, material identification, mineral mapping, and crop health identification, it is highly desired by the remote sensing community to find a way to increase the resolution of the SWIR bands to the resolution of the available VNIR bands; i.e. from 7.5m to 1.6m. This research investigates the capacities of 9 popular, industry adopted pan-sharpening algorithms for increasing the resolution of WV-3 SWIR bands. The general principles of the pan-sharpening algorithms are reviewed. The WV-3 panchromatic (Pan) images are down-sampled from 0.4m to 1.6m to fuse with the 7.5m SWIR image. Experiments demonstrate that most commonly used algorithms are not suitable for pan-sharpening SWIR images, whereas the new Fuze Go SWIR Sharp algorithm can produce satisfactory results. The reasons why most algorithms fail to produce quality pan-sharpened SWIR bands are also examined.

2.1 Introduction

The short wave infrared (SWIR) region of the electromagnetic spectrum (EMS) refers to non-visible light falling roughly between 1100 and 3000 nm. There are several benefits of collecting image bands within the SWIR region, including improving atmospheric transparency, smoke penetration, material identification, and crop health identification. Therefore, SWIR data can significantly improve applications in material identification, mineral/geology mapping, agriculture, and wildfire response, which are generally not possible for visible and near-infrared (VNIR) data. Further details about SWIR applications can be found in the references (DigitalGlobe, 2016a; DigitalGlobe, 2016b).

WorldView-3 (WV-3) is the first commercial satellite (launched on August 13, 2014) to include 8 SWIR bands in the data collection, (DigitalGlobe, 2016a). Together with the Pan band and 8 VNIR bands, the WV-3 satellite collects 1 Pan band and 16 spectral bands simultaneously (**Table 2-1**). The availability of 8 SWIR bands, which capture the unique spectral signatures of certain ground materials, has opened up new opportunities for more high-resolution information extraction which were not possible before. The native resolution of the SWIR bands is 3.7m; however, due to the US government regulation, the commercially available, maximum resolution of the SWIR bands is only 7.5m.

To utilize the advantages of SWIR bands for its unique applications, high-resolution SWIR imagery is desired. For example, it is not possible to accurately identify roof materials of buildings with a 7.5m resolution. It is also difficult for mineral mapping, understanding crop health conditions, and pinpointing the sites of active burning in a wildfire, when the resolution is 7.5m. Marchisio 2014 showed how much more information

a 3.7m SWIR image from WV-3 can provide compared to a 30m SWIR image from ASTER. The difference is significant.

To maximize the application potential of the available 16 spectral bands of WV-3 satellite, it will be ideal to obtain the same resolution for both VNIR and SWIR image bands. Because VNIR and SWIR bands measure different physical phenomena of the ground objects, the combination of VNIR and SWIR bands can offer additional information for remote sensing analytics (DigitalGlobe, 2016b). For example, the yellow, red edge, and two near-infrared bands of the VNIR data are sensitive to changes in green chlorophyll of crops and expose the carotenoids of leaves during crop stresses.The SWIR bands can measure crop moisture. The combination of these bands can increase the accuracy of crop growth analysis. However, the resolution difference between the available WV-3 VNIR bands (1.6m) and SWIR bands (7.5m) is greater than a factor of 4. This difference makes combined analyses difficult.

Because of the large demand for high-resolution SWIR images- which would preferably have the same resolution as that of the VNIR images- there is a need to investigate the potential of existing pan-sharpening algorithms for improving the resolution of WV-3 SWIR bands. Several publications (Nikolakopoulos, 2008; Padwick et al., 2010; Zhang and Mishra, 2012; and Mercovich, 2015) have reported the qualities of popular algorithms for pan-sharpening VNIR images. However, no publication has been found by this author that examines the capacities of existing algorithms for pan-sharpening SWIR imagery. Therefore, this paper aims to investigate the capacities of nine popular pan-sharpening algorithms adopted by industry for improving the resolution of WV-3 SWIR bands from 7.5 m to 1.6 m. The outcome will provide useful information to remote sensing researchers

and practitioners for effectively utilizing WV-3 SWIR bands for advanced remote sensing applications.

Table 2-1 Characteristics of the Pan, VNIR, and SWIR sensors of WV-3 satellite

Band	Spectral Range (nm)	Spatial Resolution (m)	Available Spatial Resolution (m)
Pan	450 - 800	0.31	0.4
Coastal	400 - 450	1.24	1.6
Blue	450 - 510	1.24	1.6
Green	510 - 580	1.24	1.6
Yellow	585 - 625	1.24	1.6
Red	630 - 690	1.24	1.6
Red Edge	705 - 745	1.24	1.6
NIR-1	770 - 895	1.24	1.6
NIR-2	860 - 1040	1.24	1.6
SWIR-1	1195 - 1225	3.7	7.5
SWIR-2	1550 - 1590	3.7	7.5
SWIR-3	1640 - 1680	3.7	7.5
SWIR-4	1710 - 1750	3.7	7.5
SWIR-5	2145 - 2185	3.7	7.5
SWIR-6	2185 - 2225	3.7	7.5
SWIR-7	2235 - 2285	3.7	7.5
SWIR-8	2295 - 2365	3.7	7.5

2.2.Pan-sharpening algorithms

The general principles of the nine pan-sharpening algorithms most widely-used by industry are discussed below.

2.2.1 High Pass Filter (HPF)

In HPF pan-sharpening (Gangkofner, 2008), the high frequency information is extracted from the high-resolution pan image using a high pass filter. The high frequency information is then added into each band of the up-sampled low-resolution MS image with a specified weight.

2.2.2 Intensity-Hue-Saturation (IHS)

IHS pan-sharpening (Siddiqui 2003) utilizes the IHS (intensity, hue, saturation) transformation to convert three MS bands from RGB (red, green, blue) into IHS space and then replaces the intensity band with the Pan band, followed by an inverse IHS transformation.

2.2.3 Principle Component Analysis (PCA)

PCA pan-sharpening (Chavez et al. 1991) method uses the principal component (PC) transformation to convert MS bands into PCs according to the eigenvectors of their corresponding covariance matrices. The first principal component (PC-1) is then replaced by the high-resolution Pan image. The pan-sharped MS image is obtained by applying an inverse PC transformation on the new set of components.

2.2.4 Brovey

In Brovey pan-sharpening (Klonus and Ehlers 2009), each pan-sharpened band is generated by multiplying the corresponding MS band with the Pan band and then dividing by the sum of all MS bands to be fused.

2.2.5 Wavelet

Wavelet pan-sharpening utilizes a wavelet transformation to decompose the high-resolution Pan image into one low frequency approximation image and three high frequency feature images. The low frequency approximation image is then replaced by the low-resolution MS bands, and then followed by individual inverse wavelet transformations for each MS band.

2.2.6 Gram Schmidt

Gram Schmidt pan-sharpening (Laben, 1998) generates a simulated lower resolution Pan image through weighted sum of MS bands. A Gram Schmidt transformation is then applied to the simulated low-resolution Pan and the low-resolution MS bands, with the simulated Pan as the first band. The high-resolution Pan image is adjusted to match the first band of Gram Schmidt transformed bands. Then the adjusted high-resolution Pan is used to replace the first band of the Gram Schmidt transformed bands, followed by an inverse Gram Schmidt transformation to produce pan-sharpened bands.

2.2.7 Hyperspherical Color Space (HCS)

In HCS pan-sharpening (Padwick et al., 2010), image data is transformed from native colour space to a hyperspherical colour space. The pan-sharpened image is obtained by reverse transformation from HCS colour space to the original colour space.

2.2.8 NNDiffuse

This algorithm (Sun et al., 2014) assumes that each new spectrum in the high-resolution fused image is a weighted combination of the immediate neighboring super-pixel spectra in the low-resolution MS image. The weights are controlled by a diffusion model inferred from the pan image that relates the similarity of the pixel of interest to the neighbouring super-pixels.

2.2.9 Fuze Go SWIR Sharp (FGSS)

FGSS (Zhang and Mishra 2012, Zhang 2004) is an extension of the Fuze Go algorithm (formerly known as UNB pan-sharp (Zhang 2004)). The FGSS algorithm utilizes the least squares technique to find the best fit between the grey values of the Pan band and the VNIR+SWIR bands to adjust the contribution of individual bands to the fusion. It employs a set of statistical approaches to estimate the grey value relationship between all the input bands to eliminate the problem of dataset dependency (i.e. reduce the influence of dataset variation in the fusion. In the fusion process, original 1.2m VNIR bands, 7.5m SWIR bands, and 0.3m Pan band of WorldView-3 are utilized to generate 1.2m SWIR bands.

2.3 SWIR fusion results

The WV-3 imagery covering 88 km^2 of Sebastopol, Ukraine, Europe, provided by Exelis for DigitalGlobe was used in the SWIR pan-sharpening. The imagery was the first data set made available to the user community for testing. It includes different types of land covers such as urban, forest, agriculture, and water body.

The WV-3 Pan image was down-sampled from 0.4m to 1.6m using bilinear interpolation for the SWIR pan-sharpening, to produce pan-sharpened 1.6m SWIR bands that have the same resolution as the VNIR bands.

The nine algorithms discussed in section 2.2 were used to pan-sharpen the SWIR bands. The best processing procedure suggested by the respective user manual of each individual pan-sharpening technique and the default pan-sharpening parameters were used. The interpolation methods used in each pan-sharpening algorithm are summarized in **Table 2-2**. Due to space limit and for clear visualization, only small subsets are displayed in this paper.

Table 2-2 Interpolation methods used in different pan-sharpening methods

	HPF	PCA	Brov	Wave	GS	HCS	NND	FGSS
Interpolation method	BLI	BLI	BLI	BLI	CCI	BL	CCI	BLI
BLI: Bilinear interpolation; CCI: Cubic Convolution interpolation								

Figure 2.1 shows an enlarged subset of the original 1.6m RGB bands from the VNIR image, a down-sampled 1.6m Pan image, a color composite of three original 7.5m SWIR

bands, and the pan-sharpened 1.6m SWIR bands produced by the nine different pan-sharpening algorithms. presents the color composites of different three-band combinations of the pan-sharpened SWIR bands of the FGSS algorithm.

2.4 Quality evaluation and result analysis

2.4.1 Visual comparison

To avoid bias in the evaluation of SWIR pan-sharpening qualities, all the images before and after fusion were displayed under the same visualization conditions in **Figure 2.1** and **Figure 2.2**.

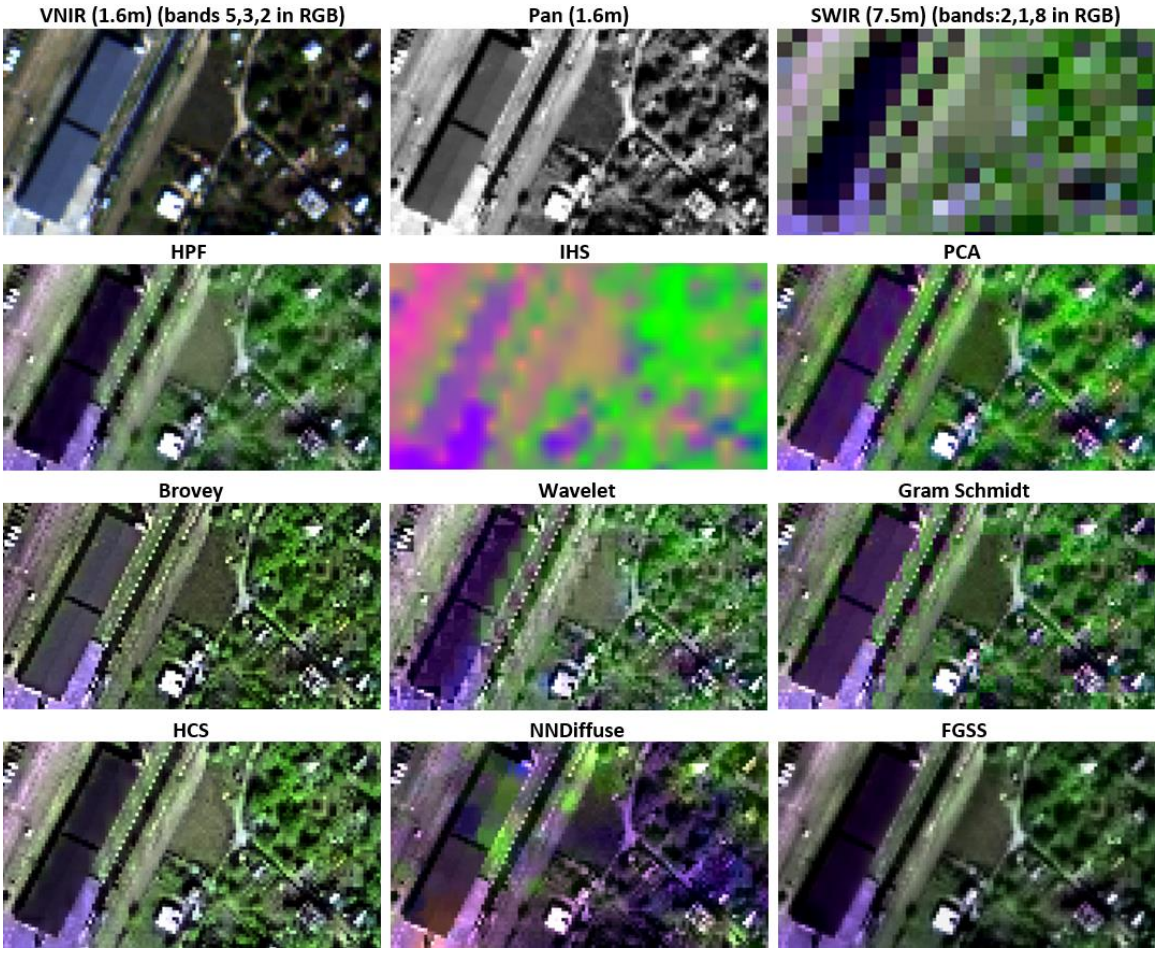

Figure 2.1 Comparison between the original VNIR (1.6m), Pan (down-sampled to 1.6m), SWIR (7.5m) WV-3 images and the pan-sharped (1.6m) WV-3 images from different pan-sharpening algorithms (2 times enlarged subset).

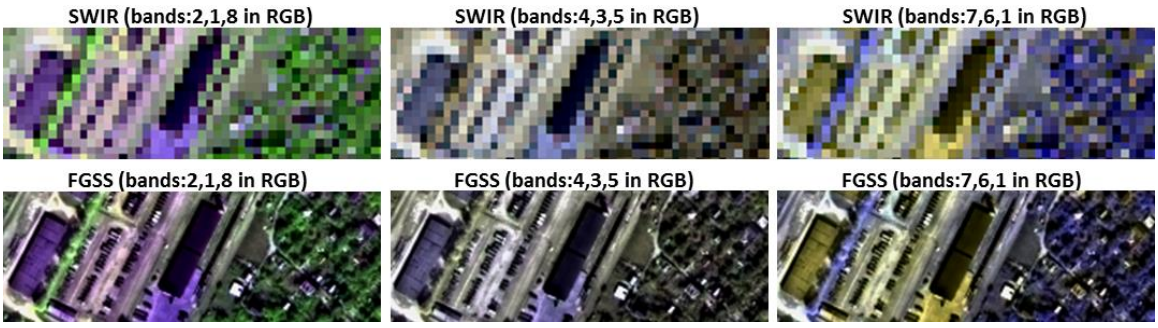

Figure 2.2 Comparison of different band combinations of the original (7.5m) and FGSS pan-sharpened (1.6m) WV-3 SWIR images.

2.4.1.1 Spatial quality evaluation

The spatial detail evaluations of SWIR bands were done by comparing the original 1.6m RGB bands from VNIR sensor and the down-sampled 1.6m Pan band with the pan-sharpened SWIR bands shown in **Figure 2.1**. It can be clearly seen that the spatial details of the FGSS pan-sharpened SWIR bands are almost identical to the down-sampled Pan image; whereas the Brovey result is sharper than the down-sampled Pan image and HPF is close to the down-sampled Pan image. The spatial detail distortion further enlarges from PCA, HCS to Gram Schmidt, until the total loss of the spatial details in the IHS result.

2.4.1.2 Spectral quality evaluation

For spectral quality evaluation, the colour of the original SWIR image was compared to those of the pan-sharpened SWIR images. The focus of comparison was to examine the presence or absence of colour distortions in the pan-sharped images. In **Figure 2.1**, it can be seen that the colour of the FGSS result is closest to that of the original SWIR image, followed by that of HPF and Gram Schmidt methods. NNDiffuse produces severe colour distortion and IHS completely distorts the colour.

2.4.1.3 Spatial and spectral integration quality evaluation

For the spatial and spectral integration quality evaluation, the quality of spatial and spectral integration in the pan-sharped images was examined. When comparing the input 1.6m Pan and 7.5m SWIR images with fused images in **Figure 2.1**, it can be seen that FGSS produced the best spatial and spectral integration followed by Brovey, whereas most other algorithms produced obvious colour artifacts due to poor spatial and spectral integration. The colour artifacts increase from HPF, PCA, Gram Schmidt, HCS to Wavelet.

The visual comparison can be summarized in **Table 2-3**.

Table 2-3 Quality ranking of visual comparison

	HPF	PCA	Brov	Wave	GS	HCS	NND	FGSS
Spa.Q	2	4	3	8	6	5	7	1
Spe.Q	2	4	5	7	3	6	8	1
Int.Q	3	4	2	7	5	6	8	1
1 = best; 8 = last; (IHS is not displayed because of its complete distortion.) Spa.Q = Spatial Quality; Spe.Q = Spectral Quality; Int.Q = Integration Quality								

2.4.2 Statistical comparison

In this paper, the following quality assessment indicators are used to assess the quality of pan-sharpened SWIR bands.

2.4.2.1 ERGAS

The ERGAS value is defined as (Wald 2000):

$$ERGAS = 100\frac{h}{l}\sqrt{\frac{1}{N}\sum_{i=1}^{N}\left(\frac{RMSE(i)}{Mean(i)}\right)^2} \qquad (2\text{-}1)$$

where, h/l is the ratio between pixel sizes of Pan and MS images, *RMSE(i)* and *Mean(i)* are the RMSE and mean of the i^{th} pan-sharpened band. A low ERGAS value indicates better image quality.

2.4.2.2 SAM

SAM (Yuhas et al. 1991) is the absolute angle between the two vectors constructed from each pixels of the original image X and the pan-sharpened image Y. For an ideal fused image, the SAM value should be zero. The SAM value is defined as

$$SAM = cos^{-1} \frac{\sum_{i,j} X_{i,j} Y_{i,j}}{\sqrt{\sum_{i,j} X_{i,j}^2} \sqrt{\sum_{i,j} Y_{i,j}^2}} \qquad (2\text{-}2)$$

where *X* and *Y* are the two spectral vectors with the same wavelength from the original MS image and pan-sharpened image respectively.

2.4.2.3 Universal Image Quality Index (Q)

Q (Wang and Bovik 2002) for two images X and Y is defined as:

$$Q = \frac{\sigma_{XY}}{\sigma_X \, \sigma_Y} \cdot \frac{2\mu_X \, \mu_Y}{\mu_X + \mu_Y} \cdot \frac{2\sigma_X \sigma_Y}{(\mu_X^2 + \mu_Y^2)(\sigma_X + \sigma_Y)} \qquad (2\text{-}3)$$

where σ_X and σ_Y are the variances of two images *X* and *Y* respectively where as μ_X and μ_Y are the means of the two images *X* and *Y* respectively. In (3), the first component is the correlation coefficient between *X* and *Y* images, the second term is a comparison of means between *X* and *Y* images, and the third term is a comparison of the image contrast. An index value that is close to 1 means good quality.

2.4.2.4 Q2n Quality Index(Q-8)

Q2n (Garzelli and Nencini 2009) for two images X and Y is defined as:

$$Q_{N \times N} = \frac{\sigma_{XY}}{\sigma_X \, \sigma_Y} \cdot \frac{2\bar{X} \, \bar{Y}}{(\bar{X})^2 + (\bar{Y})^2} \cdot \frac{2\sigma_X \sigma_Y}{\sigma_X^2 + \sigma_Y^2} \qquad (2\text{-}4)$$

where σ_X and σ_Y are the variances of two images *X* and *Y* respectively where as σ_{XY} the cross-covariance of images *X* and *Y* respectively. *Q2n* is an extension of the universal image quality index. An index value that is close to1 means good quality.

2.4.2.5 Structural Similarity Index (SSIM)

SSIM (Wang et al. 2004) is defined as follows:

$$SSIM = \frac{(2\mu_x \mu_{y+} C_1)(2\sigma_{xy}+C_2)}{(\mu_x^2+\mu_y^2+C_1)(\sigma_x^2+\sigma_y^2+C_2)} \qquad (2\text{-}5)$$

where μ is the mean of the image, σ is the standard deviation, C_1 and C_2 are constants taken from the literature. The closer the SSIM value is to 1, the better the quality.

The results obtained from the quality indicators are shown in **Table 2-4**. ERGAS, SAM, Q, and Q-8 methods are used to measure the spectral quality of the pan-sharpened image. For spectral quality assessment, the original SWIR image (7.5m) was used as a reference image, and the Pan and SWIR were down-sampled to 7.5m and 30m respectively to generate a 7.5m pan-sharpened result for comparison. The SSIM method is used to measure the spatial quality of the pan-sharpened SWIR image, for which the down-sampled 1.6m Pan image was used as a reference.

Table 2-4 Statistical comparison results

	HPF	PCA	Brov	Wave	GS	HCS	NND	FGSS
ERGAS	5.09	16.15	21.54	5.01	6.3	5.43	21.6	2.05
SAM	2.20	19.54	13.99	3.1	2.8	0.61	5.02	1.98
Q	0.73	0.45	0.005	0.70	0.72	0.89	0.08	0.94
Q-8	0.70	0.43	0.040	0.65	0.61	0.67	0.01	0.90
SSIM	0.97	0.67	0.93	0.71	0.95	0.76	0.12	0.99
Ideal values: ERGAS = 0; SAM = 0; Q = 1; Q-8=1; SSIM = 1 (IHS is not included because of its complete spatial and spectral distortion)								

Similar to the visual comparison, the statistical indexes also confirm that the FGSS algorithm produces the best results in terms of spectral and spatial fidelities. Based on the indexes, although HPF, Brovey, and Gram Schmidt reached acceptable spatial quality, their spectral qualities are poor. The other remaining pan-sharpening algorithms introduced both serious spatial and spectral distortions, which are reflected by their poor spatial and spectral indexes.

2.4.3 Result analysis

From the general principal of the nine algorithms discussed in section 2.2, one can see that most early fusion algorithms (such as HPF, IHS, Brovey, PCA and Wavelet) assume that the grey value of the Pan band is similar to that of the multispectral (MS) bands to be fused. Therefore, the high-resolution spatial information from the Pan image can be directly inputted into the MS bands, through addition, substitution, or division operations. These

methods may work well with the Pan and 4-band MS images from early satellites such as IKONOS and QuickBird, but, they do not work well with the 8-band MS image of WorldView-2 (Zhang and Mishra, 2012). They produce even poorer results for WV-3 SWIR fusion (**Figure 2.1**), because the grey value difference between the Pan and the 8 SWIR bands of WV-3 is even greater.

Gram Schmidt is known as a high quality algorithm for pan-sharpening four VNIR (R, G, B and NIR) bands. It assumes there is a fixed correlation between the Pan band and the four VNIR bands. However, this fixed correlation does not fit the correlation between the Pan and SWIR bands of WV-3. Therefore, obvious colour distortion and colour artifacts are introduced in the fusion. Colour distortions and artifacts of Gram Schmidt were also reported in early studies (Zhang and Mishra, 2012; Sun et al., 2014) where the eight VNIR bands of WorldView-2 were pan-sharpened, because the fixed correlation does not work with the eight VNIR bands either.

The HCS algorithm was developed to fuse all eight VNIR bands of the WorldView-2 satellite. It assumes that the intensity component of the VNIR bands can be well represented by the Pan band. Therefore, when the spectral bands of the VNIR image do not overlap with that of the Pan band, poor fusion results will be produced (Mercovich, 2015). Mercovich (2015) evaluated the HCS algorithm and found that although HCS improves the spatial details in all bands, it introduces noticeable spectral distortion and softens the sharpness. Obviously, the spectral coverage of the SWIR bands of WV-3 is farther away from that of the Pan band. Therefore, colour distortion is inevitable when HCS is used to fuse the Pan and SWIR bands.

The NNdiffuse algorithm was developed to solve the n-bands fusion problem. It assumes that each new spectrum in the pan-sharpened image is a weighted combination of the immediate neighboring super-pixel spectrum in the low-resolution MS image. The pan-sharpening result relies on certain external parameters which are determined based on the application of the pan-sharpened product. Due to the dependency on external parameters, serious colour distortions and artifacts are introduced into the pan-sharpened SWIR bands.

The FGSS algorithm is an image-oriented fusion approach. It does not rely on any assumption or any external parameter. It treats each set of Pan and VNIR/SWIR bands individually to find the best fit between the Pan and VNIR/SWIR bands and then fuse them together. Therefore, FGSS is able to produce high quality pan-sharpened SWIR bands (**Figure 2-1** and **Figure 2-2**).

2.5 Conclusions

This paper investigated the capacities of nine industry-adopted pan-sharpening algorithms for increasing the resolution of WV-3 SWIR bands from 7.5m to 1.6m. The experiments prove that the FGSS technique is capable of producing high quality pan-sharpened SWIR bands (**Figure 2-1** and **Figure 2-2**); whereas other fusion techniques produced poor results, with obvious spectral distortion, poor spatial quality, and/or colour artifacts (**Figure 2-1**). The reason FGSS produces good results is that FGSS treats each Pan and MS set to be fused individually and aims to find the best fit between the bands in the fusion. However, the other methods use fixed parameters in the fusion. When the MS bands are changed from VNIR to SWIR, the fixed parameters do not work anymore, so that colour distortions and artifacts are inevitably introduced.

Any resolution increase of WV-3 SWIR imagery will increase its application potential. It will further broaden its application potential if the SWIR resolution is increased from 7.5m to that of the VNIR bands (1.6m). FGSS demonstrated the capacity to produce high quality 1.6m pan-sharpened SWIR imagery, which is proved by visually examining two-times enlarged results and quantitative measurements. This capacity will provide remote sensing researchers and practitioners with an effective tool to utilize and extend WV-3 SWIR imagery for advanced applications.

2.6 Acknowledgement

The Canada Research Chairs Program funded this research. The original WorldView-3 Pan, VNIR and SWIR images were provided by Exelis for DigitalGlobe Inc.

2.7 References

Chavez, S., Sides, C., and Anderson, A. (1991). Comparison of three different methods to merge multiresolution and multispectral data: Landsat TM and SPOT panchromatic. *Journal of Photogrammetric Engineering and Remote Sensing*, 57(3): 295–303.

DigitalGlobe, Inc. Exploring the benefits of SWIR satellite imagery, white paper. Accessed 22 February17: http://global.digitalglobe.com/sites/default/files/DG_SWIR_WP.pdf

DigitalGlobe, Inc. Moving from Pixels to Products… and data to insight, white paper. Accessed 22 February 2017: http://global.digitalglobe.com/sites/default/files/DG_Pixels_to_Products_forWeb.pdf

Gangkofner, U. G., Pradhan, P. S., & Holcomb, D. W. (2008). Optimizing the high-pass filter addition technique for image fusion. *Journal of Photogrammetric Engineering and Remote Sensing*, 74(9): 1107–1118.

Garzelli, A., & Nencini, F. (2009). Hypercomplex Quality Assessment of Multi/Hyperspectral Images. *IEEE Geoscience and Remote Sensing Letters*, 6(4): 662-665.

King, R. L. & Wang, J. (2001). A wavelet based algorithm for pan sharpening Landsat 7 imagery. *Proceedings of International Geoscience and Remote Sensing Symposium (IGARSS 2001)*, July 9-13, Sydney, Australia.

Klonus, S., & Ehlers, M. (2009). Performance of evaluation methods in image fusion. *Proceedings of the 12th International Conference on Information Fusion*, July 6–9, Seattle, WA.

Laben, C. A., & Brower, B. V. (1998). Process for enhancing the spatial resolution of multispectral imagery using pan-sharpening. *US Patent US* 6,011,875, filed April 29.

Marchisio, Giovanni. (2014). An Overview of the WorldView-3 Sensor. *Centre International Conference, Geneve, Switzerland,* May 05-09.

Mercovich, R. A. (2015). Evaluation techniques and metrics for assessment of pan+MSI fusion (pansharpening). *Proceeding of the SPIE 9472, Algorithms and Technologies for Multispectral, Hyperspectral, and Ultraspectral Imagery*, April 20-24, Baltimore, MD.

Nikolakopoulos, K. G. (2008). Comparison of nine fusion techniques for very high resolution data. *Journal of Photogrammetric Engineering & Remote Sensing* 74 (5): 647–659.

Padwick, C., Deskevich, M., Pacifici, F. & Smallwood, S. (2010). Worldview-2 Pansharpening. *Proceedings of the American Society for Photogrammetry and Remote Sensing Annual Conference*, April 26–30, San Diego, CA.

Siddiqui, Y. (2003). The modified IHS method for fusing satellite imagery. *Proceedings of ASPRS annual conference,* May, 2003, Anchorage, Alaska.

Sun, W., Chen, B., & Messinger, D. W. (2014). Nearest-neighbor diffusion-based pan-sharpening algorithm for spectral images. *Optical Engineering*. 53(1): 013107-013107.

Wald, L. (2000). Quality of high resolution synthesized: is there a simple criterion?. *Proceedings of the International Conference on Fusion of Earth Data,* January 26-28, Sophia Antipolis, France.

Wang, Z., & Bovik, A. C. (2002). A universal image quality index. *EEE Signal Processing Letters, 9(3):* 81-84.

Wang, Z., Bovik, A. C., Sheikh, H. R., & Simoncelli, E. P. (2004). Image quality assessment: from error visibility to structural similarity. *IEEE Transactions on Image Processing*, 13 (4): 600-612.

Yuhas, R. H., Goetz, A. F. H., & Boardman, J.W. (1991). Discrimination among semi-arid landscape endmembers using the spectral angle mapper." *Proceeding of the third annual JPL Airborne Geoscience Workshop*, June 1, Pasadena, California.

Zhang, Y. (2004). Highlight Article: Understanding Image Fusion. *Journal of Photogrammetric Engineering & Remote Sensing*, 70(6): 657-661.

Zhang, Y., and Mishra, R. K. (2012). A review and comparison of commercially available pan-sharpening techniques for high resolution satellite image fusion." *Proceedings of the* IEEE International Geoscience and Remote Sensing Symposium, Munich, July 22-27.

Chapter 3 : Solar Photovoltaic Panel Detection using WorldView-3 satellite imagery

Abstract

Solar photovoltaic (PV) panel installations are exponentially growing worldwide. Quickly and effectively detecting solar PV panels is important for energy and environment policy making. However, traditional methods such as manual surveys and information collection from Solar PV vendors are laborious and often yield insufficient information. WorldView-3 images with its 16 spectral bands may provide a potential for cost-effectively extracting solar PV panel information. However, the resolution of commercially available 8 SWIR bands is only 7.5m, which is not sufficient for detecting small solar PV panel installations. It is also difficult to differentiate large solar PV panel installations from some large building roofs. In addition, the resolution of the 8 VNIR bands of WorldView-3 is 1.2m, which is difficult to integrate with the 8 SWIR bands for solar panel detection. This paper introduces a high-resolution, super spectral formation, and spectral angle mapping (HR-SSF-SAM) integrated method for solar PV panel detection. First, the resolution of the 8 SWIR bands is increased from 7.5m to 1.2m using the Fuze Go SWIR Sharp algorithm. Then, the 8 1.2m SWIR bands are integrated with the 8 1.2m VNIR bands to form a 16-band 1.2m super spectral image. At the end, the Spectral Angle Mapper (SAM) algorithm is adapted to identify solar PV panels in the 16-band super spectral image. The proposed HR-SSF-SAM method is tested on the WorldView-3 image of Brea, California, USA. The results demonstrate that a true detection rate of 93.3% is achieved with a 0% false detection rate. Even solar PV panels and glass roofs can be differentiated from each other.

3.1 Introduction

In recent years, there is a rapid growth of solar photovoltaic (PV) panel installations in the USA and around the world because of the technical advancement in PV and battery technologies, fast reduction in prices of solar PV panels, and government subsidies and encouragements for green energy. Hence, small scale solar power generation is quickly becoming a viable alternative to conventional sources of electricity. A report from the California Solar Initiative (CSI) shows that in California alone the solar PV capacity has increased 12 times in the years from 2006 to 2014 (Hallock and Kinman, 2015).

Therefore, it is important to acquire information about solar PV panel installations, such as the number of solar PV panels installed in an area of interest. This information is crucial in quantifying the energy production of existing solar PV panels in order to make informed decisions, such as energy policies and regulations, system planning for capacity expansion, transmission and distribution upgrades, and operation adjustments to ensure grid reliability and resilience (Malof et al., 2015). However, the traditional methods, such as on-site surveys and information collection from solar PV vendors, are laborious, time consuming, and often yield insufficient data for government and utility decision makers. In addition, the data collected by traditional methods may quickly become outdated due to the rapid growth of solar PV installations. To overcome these challenges, there is a need for new technologies that can obtain accurate information on solar PV panel installation and distribution in a cost-effective fashion.

With the recent advancement of earth imagining satellite sensors, researchers have attempted to identify solar PV panels using very high-resolution color aerial images. However, manual interpretation is not only time consuming, but it is also difficult to

differentiate solar PV panels from roofs with similar color. Bradbury et al. (2016) developed a database of solar PV panel installations for four US cities using very high-resolution (less than 30cm) aerial imagery by manually delineating individual solar PV panel installations. Malof et al. (2015) did a feasibility study, in which a computer vision algorithm was tested to detect solar PV panels in very high-resolution, visible (RGB) imagery. Only limited success was achieved because the spectral information of solar PV panels is similar to that of dark roofs, parking lots, and roads.

The launch of WorldView-3 satellite on August 13, 2014, brings a new opportunity for solar PV panel detection. It is the first commercial satellite to include 8 short wave infrared (SWIR) bands in the data collection (DigitalGlobe, 2016). Together with the existing Pan and VNIR bands, WorldView-3 simultaneously collects 1 Pan band and 16 spectral bands. The inclusion of the 8 SWIR bands has increased the potential to detect solar PV panels. However, the commercially available SWIR bands only have a resolution of 7.5m, which is not sufficient for detecting small solar PV panel installations. In addition, the experiments reveal that the spectral information in the SWIR bands is not sufficient to separate solar PV panels from some building roofs that have certain special materials. On the other hand, the VNIR bands of WorldView-3 have a resolution of 1.2m, which is more than 6 times higher than that of the available SWIR bands. Therefore, it is not only difficult to detect solar PV panels using either the original VNIR bands or the available SWIR bands, but also difficult to combine the VNIR bands and the SWIR bands to collectively detect solar PV panels. In the extensive literature review, no successful technique that can effectively detect solar PV panels in satellite imagery has been found.

This paper introduces a new method — a high-resolution, super spectral formation and spectral angle mapping (HR-SSF-SAM) method — to detect solar PV panels using WorldView-3 imagery. To solve the low-resolution problem of the available SWIR bands, the Fuze Go SWIR Sharp algorithm (Fuze Go, 2016) is utilized to increase the resolution of the SWIR bands from 7.5m to 1.2m, to produce a set of high-resolution SWIR bands (HR SWIR, with an equal resolution to that the original VNIR bands). To overcome the spectral limitations of either the VNIR bands or the SWIR bands for solar PV panel detection, the 8 original VNIR bands are stacked together with the 8 new HR SWIR bands to form a high-resolution, super spectral image with 16 bands at 1.2m resolution. To effectively detect solar PV panels in the high-resolution, super spectral image, the Spectral Angle Mapper (SAM) algorithm (ENVI, 2016; Kruse et al., 1993) is adapted to determine the spectral similarity between the image spectrum and the reference spectrum of solar PV panels. The image pixels with similar spectral angles are detected as solar PV panel pixels.

The proposed HR-SSF-SAM method was tested using WorldView-3 imagery collected over Brea, California, USA. A true detection rate of 93% was achieved with a 0% false detection rate. Even glass roofs and solar PV panels, that are difficult for human eye to separate, can be differentiated by the proposed HR-SSF-SAM method.

The remainder of this paper is organized as follows. Section 3.2 describes the study area and data set; section 3.3 discusses the spatial and spectral information of the SWIR bands; section 3.4 introduces and explains the proposed method; the results and accuracy analysis are presented in section 3.5; and the conclusions are given in section 3.6.

3.2 Study area and data set

The study area covers an area of 20 km^2 of Brea, California, USA. The WorldView-3 imagery of the study area was collected in November 2014 and provided by DigitalGlobe. As indicated in **Figure 3.1**, solar PV panels with various sizes are distributed in the area among buildings and other ground objects. Quick Atmospheric Correction (QUAC) method (ENVI, 2016) was applied to the data. QUAC is a VNIR-SWIR atmospheric correction method and works best with scenes that contain man-made structures. The spectral and spatial information of the WorldView-3 image bands is provided in **Table 3-1**.

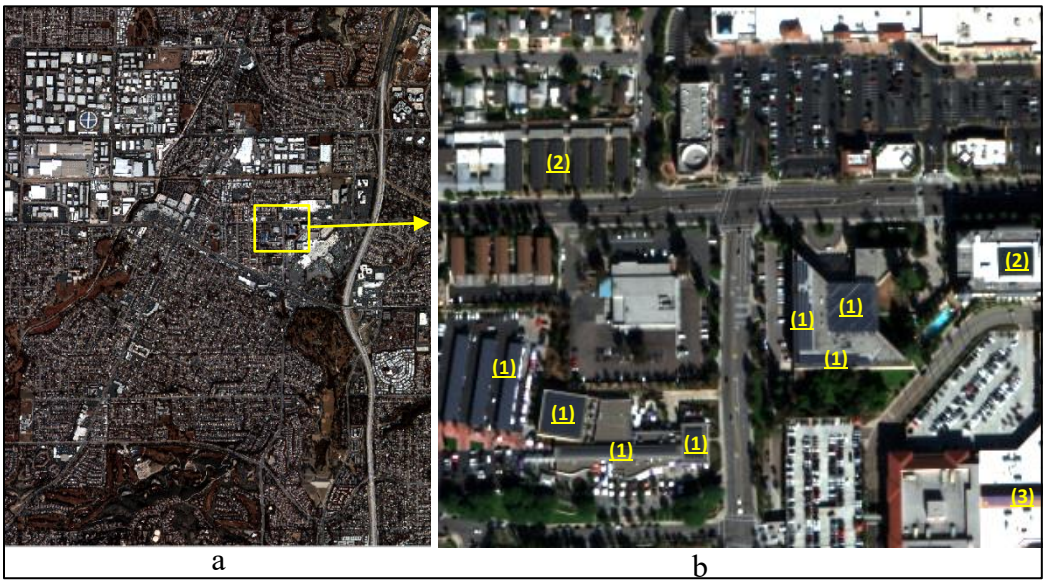

Figure 3.1 Study area and a subsection with solar PV panels. (a) Overview of the study area in the 1.2m natural colour image of WorldView-3, and (b) solar PV panels (1), dark roofs (2), and a glass roof (3).

Table 3-1 Characteristics of the WorldView-3 imagery used in this study.

Band		Spectral range (nm)	Spatial resolution (m)
	Pan	450 - 800	0.5
VNIR	Coastal	400 - 450	1.2
	Blue	450 - 510	1.2
	Green	510 - 580	1.2
	Yellow	585 - 625	1.2
	Red	630 - 690	1.2
	Red Edge	705 - 745	1.2
	NIR-1	770 - 895	1.2
	NIR-2	860 - 1040	1.2
SWIR	SWIR-1	1195 - 1225	7.5
	SWIR-2	1550 - 1590	7.5
	SWIR-3	1640 - 1680	7.5
	SWIR-4	1710 - 1750	7.5
	SWIR-5	2145 - 2185	7.5
	SWIR-6	2185 - 2225	7.5
	SWIR-7	2235 - 2285	7.5
	SWIR-8	2295 - 2365	7.5

The Pan and VNIR bands of WorldView-3 are almost the same as those of WorldView-2. The SWIR bands of WorldView-3 are beyond the near-infrared region falling roughly between 1100 and 3000 nm. The SWIR sensor is strategically designed to capture the unique spectral signatures of certain ground materials (DigitalGlobe, 2016). This opens up new opportunities to extract more high-resolution information which were not possible before. Particularly, the SWIR spectral bands can significantly improve applications in identification of man-made materials beyond the capacity of VNIR spectral bands. Young (2015) shows the usefulness of WorldView-3 SWIR spectral bands in the identification of man-made materials and minerals.

3.3 Spatial and spectral information of the SWIR bands

3.3.1 Spatial resolution of the SWIR bands

Solar PV panels have some unique absorption features in the WorldView-3 SWIR bands, which increases the possibility to detect solar PV panels. However, the 7.5m resolution makes it difficult to detect small solar PV panel installations. As shown in **Figure 3.2** (a) and **Figure 3.2** (a) the large size solar PV panel installations can be identified in the 7.5m resolution SWIR bands, but small solar PV panel installations cannot be identified. On the other hand, as shown in **Figure 3.2** (c), both large and small solar PV panel installations are clearly visible in 1.2m resolution VNIR bands.

Therefore, in order to detect both small and large solar PV panel installations, higher resolution SWIR bands are required. In addition, to maximize the application potential of the available VNIR bands and SWIR bands of WorldView-3 satellite, it is desirable to

obtain a set of high-resolution SWIR bands that have the same resolution as that of the VNIR bands.

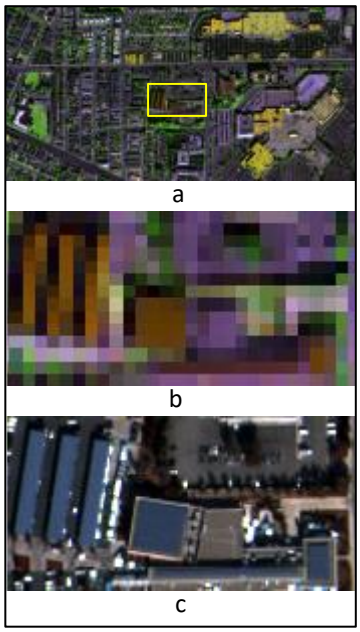

Figure 3.2 Solar PV panels in different spectral images of WorldView-3. (a) Available 7.5m SWIR bands 2, 1, 8 displayed in RGB at 1:1 ratio, (b) enlarged 7.5m SWIR bands, and (c) original 1.2m VNIR bands 5, 3, 2 displayed in RGB. (In the available SWIR bands small solar PV panel installations are not visible; however, they are clearly visible in the original VNIR bands.)

3.3.2 Spectral analysis of solar PV panels

3.3.2.1 Spectral analysis of solar PV panels

With 1.2m resolution WorldView-3 VNIR bands, the human eye can sometimes identify the solar PV panels in a complex urban scene; however, it is difficult for a computer to separate them from other ground objects which have similar spectrums. For example, as shown in **Figure 3.3** (a, b, c and d), in VNIR bands, the spectrums of a solar PV panel, two dark roofs, and a glass roof contain similar or almost the same absorption features (**Figure 3.3** (e)). The only difference is that they have a slightly different brightness. Therefore,

using VNIR bands makes it difficult or impossible for a classifier to differentiate between solar PV panels and other objects with similar spectrums. However, these ground materials have unique absorption features in different SWIR bands of WorldView-3. For example, in **Figure 3.3** (f, g, h, i and j), the spectrums of the solar PV panel, two dark roofs, and glass roof are different in SWIR bands. Therefore, the SWIR bands of WorldView-3 can help differentiate solar PV panels from those objects which cannot be done using VNIR bands.

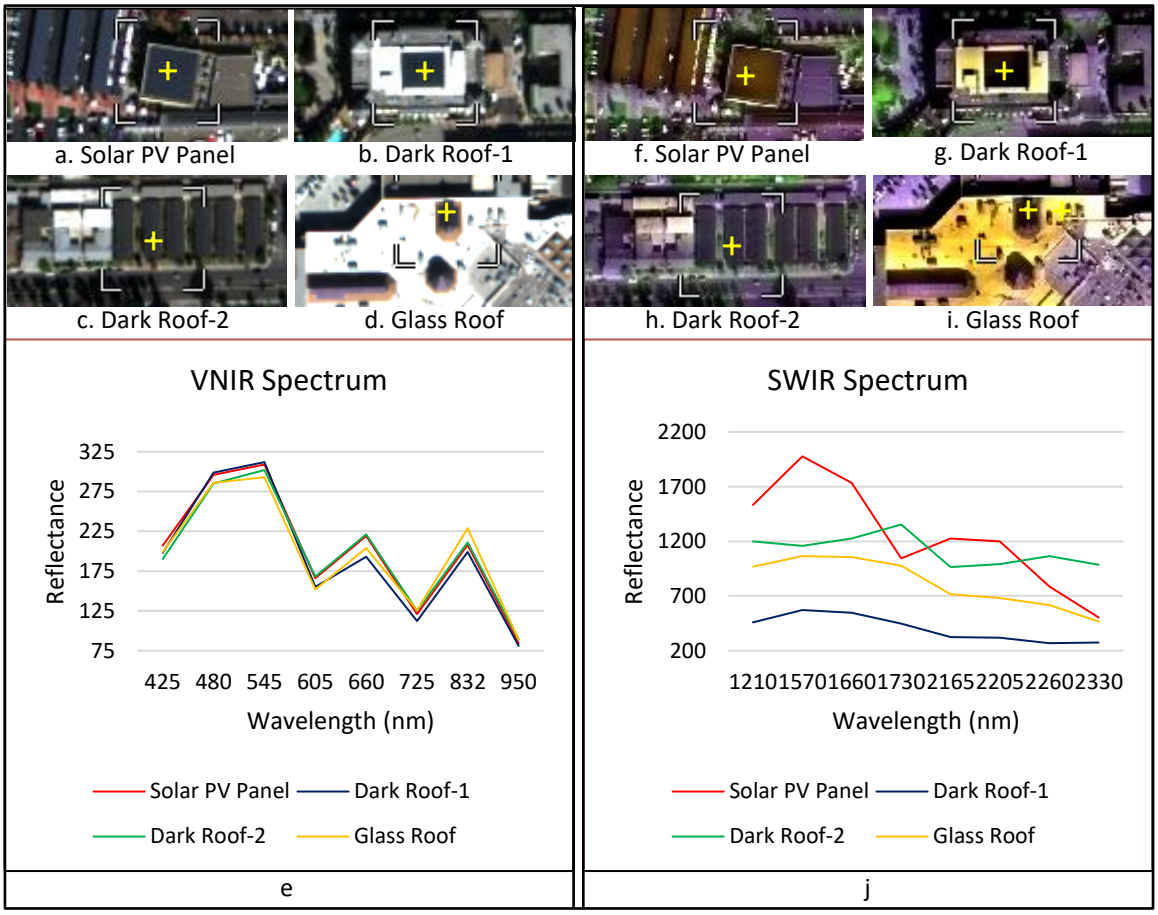

Figure 3.3 Comparison of the spectrums of a solar PV panel, dark roofs and a glass roof in VNIR and SWIR bands. (a) (b) (c) (d) solar PV panel, dark roof 1, dark roof 2, and glass roof in VNIR bands respectively, (e) the spectral curves of the pixels a, b, c, and d (centtres of the crosses) in VNIR bands, (f) (g) (h) (i) solar PV panel, dark roof 1, dark roof 2, and glass roof in SWIR bands respectively, and

(j) the spectral curves of the pixels f, g, h and i in SWIR bands. (The SWIR bands shown here are 1.2m high-resolution SWIR bands produced using Fuze Go SWIR Sharp to be discussed in the methodology section. The spectrums of solar PV panel, dark roof, and glass roof are similar in VNIR bands, but different in SWIR bands.)

3.3.2.2 Limitation of SWIR for solar PV panel detection

As shown in **Figure 3.4** (e, f, g and h), solar PV panels and white roofs have similar spectrums in SWIR bands, whereas their spectrums in VNIR bands are different as shown in **Figure 3.4** (a, b, c and d). Therefore, using the 8 SWIR bands alone make it difficult to differentiate solar PV panels from a few other objects such as white roofs.

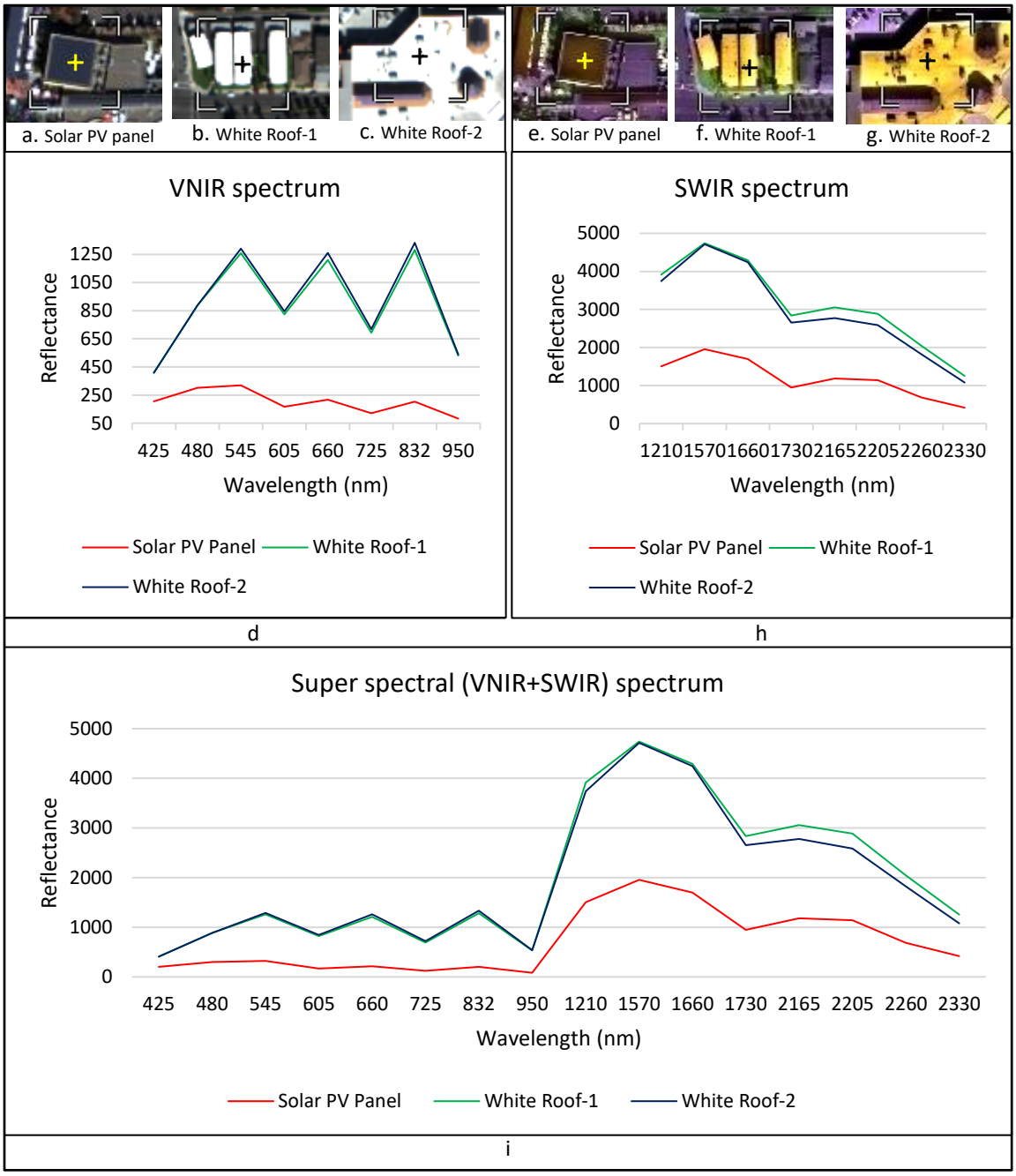

Figure 3.4 Comparison of the spectrums of a solar PV panel and white roofs in VNIR and SWIR bands. (a) (b) (c) solar PV panel, white roof-1, white roof-2 in VNIR bands respectively, (d) the spectral curves of the solar PV panel pixel (centre of the cross) and the two white roof pixels in VNIR bands, (e) (f) (g) solar PV panel, white roof-1, white roof-2 in SWIR bands respectively, (h) the spectral curves of the solar PV panel pixel and the two white roof pixels in SWIR bands, and (i) the spectral curves of the

solar PV panel pixel and the two white roof pixels in the 16 spectral bands (8 VNIR + 8 SWIR). (The solar PV panel and white roofs have similar spectral curves in SWIR bands, whereas they have different spectral curves in VNIR bands.)

3.3.2.3 Necessity of combining VNIR and SWIR bands

Some ground objects, such as dark roofs and glass roofs, have similar spectrums as that of solar PV panels in VNIR bands, but have different spectrums in SWIR bands; therefore, SWIR bands can be utilized to separate solar PV panels from dark roofs and glass roofs. However, other ground objects, such as white roofs, have similar spectrums as that of solar PV panels in SWIR bands, but different spectrums in VNIR bands. Therefore, it is not possible to achieve a high accuracy solar PV panel detection using either VNIR bands or SWIR bands, respectively.

However, as shown in **Figure 3.3**(e), **Figure 3.3**(j), and in **Figure 3.4**(i), the combination of the VNIR and the SWIR bands can ensure that sufficient spectrum difference can be found in the combined 16 super spectral bands. Therefore, it is necessary to combine the 8 VNIR bands and the 8 SWIR bands to form a 16 band super spectral image for solar PV panel detection.

3.4 Methodology of solar PV panel detection

The proposed high-resolution, super spectral formation and spectral angle mapping (HR-SSF-SAM) method consists of three major components: (1) increasing the spatial resolution of the 8 SWIR bands from 7.5m to 1.2m (equal to that of the VNIR bands) using FGSS algorithm (Fuze Go, 2016; Zhang and Mishra, 2014; Zhang, 2004) (2); combining the 8 original 1.2m VNIR bands with the 8 HR 1.2m SWIR bands to form a 16 bands super

spectral imagery; and (3) adapting the Spectral Angle Mapper (SAM) method from hyperspectral image processing to detect solar PV panels in super spectral images. The flowchart of the proposed method is shown in **Figure 3.5.**

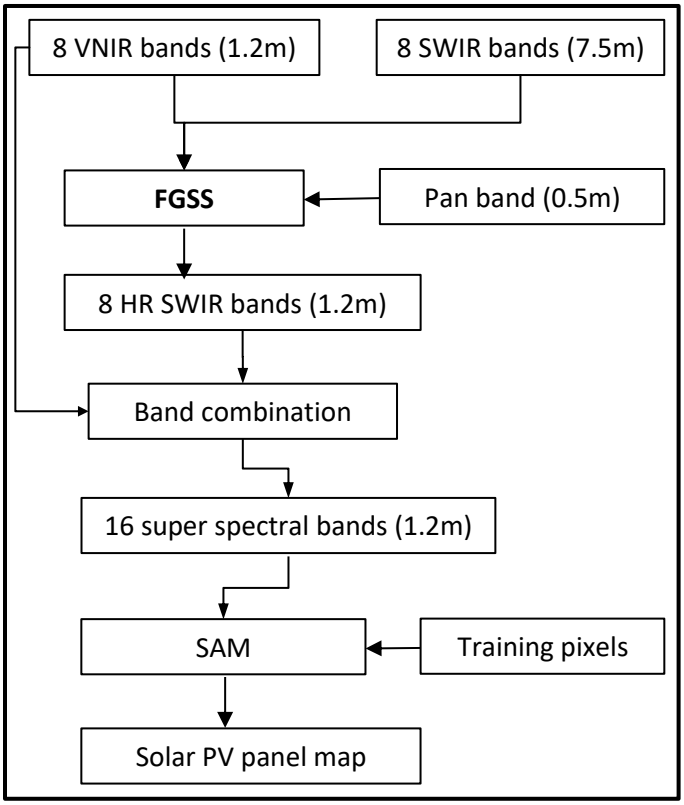

Figure 3.5 Flowchart of the proposed HR-SSF-SAM method for solar PV panel detection.

3.4.1 High-Resolution SWIR bands creation

As discussed in section 3.2, it is difficult to detect small solar PV panel installations using the available SWIR bands (7.5m resolution). It is also desirable to obtain a set of SWIR bands that have the same resolution as that of the VNIR bands, to maximize the application potential of the available 16 spectral bands of WorldView-3 satellite. Therefore, the Fuze

Go SWIR Sharp (FGSS) algorithm (Fuze Go, 2016) was used to increase the resolution of SWIR bands from 7.5m to 1.2m to produce high-resolution (HR) SWIR bands.

The FGSS algorithm is an extension of the Fuze Go algorithm (formerly known as UNB pan-sharp) (Fuze Go, 2016; Zhang and Mishra, 2014; Zhang, 2004). FGSS algorithm utilizes the least squares technique to find the best fit between the grey values of the Pan band and the VNIR/SWIR bands in order to adjust the contribution of individual bands to the fusion. It employs a set of statistical approaches to estimate the grey value relationship between all the input bands in order to eliminate the problem of dataset dependency (i.e. reduce the influence of dataset variation in the fusion). In the fusion process original 1.2m VNIR bands, 7.5m SWIR bands, and 0.3m Pan band of WorldView-3 are utilized to generate 1.2m SWIR bands.

Figure 3.6(a) and 6(b) show the available 7.5m SWIR image and the 1.2m HR SWIR image generated using FGSS algorithm. It can be seen that the generated 1.2m HR SWIR image not only has the same spectral information as the 7.5m SWIR image, but also has the same spatial resolution as that of the original 1.2m VNIR image (**Figure 3.6**(c)).

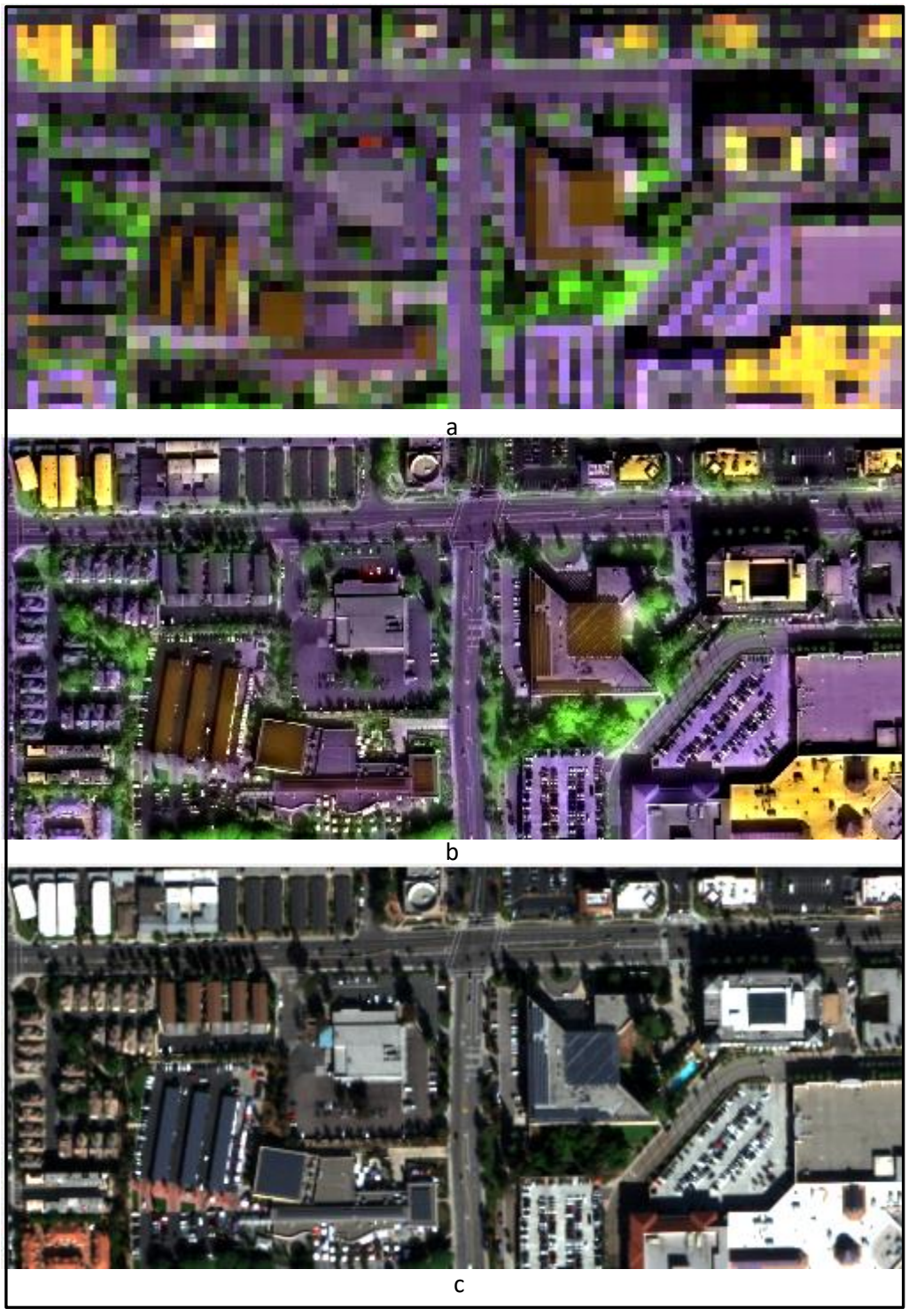

Figure 3.6 Comparison between the available 7.5m SWIR image (a), the 1.2m HR SWIR image generated using FGSS (b), and the original 1.2m VNIR image (c).

3.4.2 Super spectral image formation

As discussed in section 3.3, in VNIR bands, the spectrum of solar PV panels may be similar to that of some ground objects; however, in SWIR bands, spectrums of solar PV panel may be similar to the spectrum of other ground objects. However, the spectral analysis of VNIR and SWIR bands shows that the solar PV panel has unique spectrum features in the combination of VNIR and SWIR bands, that are different from those of none-solar-PV-panel objects. Therefore, a high-resolution, 16 band super spectral (VNIR+SWIR) image was generated by combining the eight 1.2m VNIR bands and the eight 1.2m HR SWIR bands.

3.4.3 Solar PV panel detection

The spectral angle mapper (SAM) algorithm (Kruse et al., 1993), which determines the spectral similarity between two spectrums, was adapted to identify solar PV panel installations in the high-resolution, super spectral images.

The SAM algorithm performs mapping of the spectral similarity of image spectrum to the reference spectrum which uses a n-dimensional angle to match pixels to reference spectrum (ENVI 2016; Kruse et al., 1993). The algorithm determines the similarity between two spectrums by calculating the angle between the spectrums and treating them as vectors in a space with dimensionality equal to the number of bands. The smaller angles between the two spectrums indicate high similarity and vice-versa. The reference spectrum can either be attained from the field measurements or taken directly from the image. SAM algorithm is mostly used to identify objects from hyperspectral images as the SAM algorithm can identify the ground materials based on their unique spectrum in the

hyperspectral bands. Solar illumination and albedo effects do not affect it as it uses only the vector direction and not the vector length. Moreover, the SAM algorithm works well in areas of homogeneous regions. The angle between reference and test spectrums is calculated using equation 3-1.

$$\alpha = \cos^{-1}\left\{\frac{\sum_{i=1}^{n} X_i Y_i}{\sqrt{\sum_{i=1}^{n} X_i^2}\sqrt{\sum_{i=1}^{n} Y_i^2}}\right\} \qquad (3\text{-}1)$$

where n is the number of spectral bands, X is the reference spectrum, and Y is the test spectrum.

There are two main reasons to utilize the SAM algorithm method: (1) the solar PV panel pixels have an unique spectrum in super spectral bands and SAM algorithm can accurately identify those pixel; and (2) the surfaces of solar PV panels are mostly homogenous and SAM algorithm works well in the homogenous area.

In the solar PV panel detection, SAM algorithm was applied on the 1.2m super spectral bands to detect solar PV panels. A threshold value 0.07 radian (4.01 degree) was used as maximum acceptable angle between the reference spectrum vector and the test spectrum vector. The average value of the training pixel spectrums was taken as a reference spectrum to find the optimum reference spectrum.

For result comparison purposes, the 1.2m VNIR bands, original 7.5m SWIR bands, and the 1.2m HR SWIR bands were also used for the solar PV panel detection, respectively, using exactly the same training pixels and processing parameters. **Table 3-2** shows the number of training pixels used to detect solar PV panels in VNIR bands, original SWIR

bands, HR SWIR bands, and super spectral bands. (Because the 7.5m SWIR image has a significantly lower resolution, the total number of pixels and the training pixels are also significantly less).

Table 3-2 The total number of pixels of the study area and the number of training pixels used in the solar PV panel detection from the original 1.2m VNIR, original 7.5m SWIR, produced 1.2m HR SWIR and combined 1.2m super spectral bands

	Total no. of pixels	**No. of training pixels**
1.2m VNIR (8 bands)	16777216	12
7.5m SWIR (8 bands)	438876	6
1.2m HR SWIR (8 bands)	16777216	12
1.2m Super Spectral (16 bands)	16777216	12

3.5 Results and discussions

3.5.1 Ground truth collection

The WorldView-3 imagery used in this study for solar PV Panel detection was collected in November 2014. Therefore, the very high-resolution and high quality aerial photos of Brea, California, USA that are available on Google Earth were chosen for ground truth extraction. In the aerial photos, individual solar PV panels can be clearly seen based on their color, texture and structure. In addition, a pan-sharpened 0.5m multispectral image generated using Fuze Go algorithm (Zhang and Mishra, 2014; Zhang, 2004) from the same WorldView-3 image dataset was used to assist the manual solar PV panel extraction.

The solar PV panel installations in Brea were identified and delineated by an image analyst through block-by-block scanning of the whole area. The color, texture and structure information in the aerial photos and the spatial and multispectral information in the pan-sharpened image were utilized for the solar PV panel interpretation. A total of 15 solar PV panel installations, including large area installations and small area installations, were found in the study area.

3.5.2 Solar PV panel detection results

Figure 3.7(a) shows the area where solar PV panels were detected using the proposed HR-SSF-SAM method applied on super spectral bands. The detected solar PV panels are indicated in red and WorldView-3 natural color imagery is shown as the background. For comparison purposes, **Figure 3.7** (b), 7(c), 7(d), and 7(e) show an enlarged area with the detected solar PV panels from the four different image datasets.

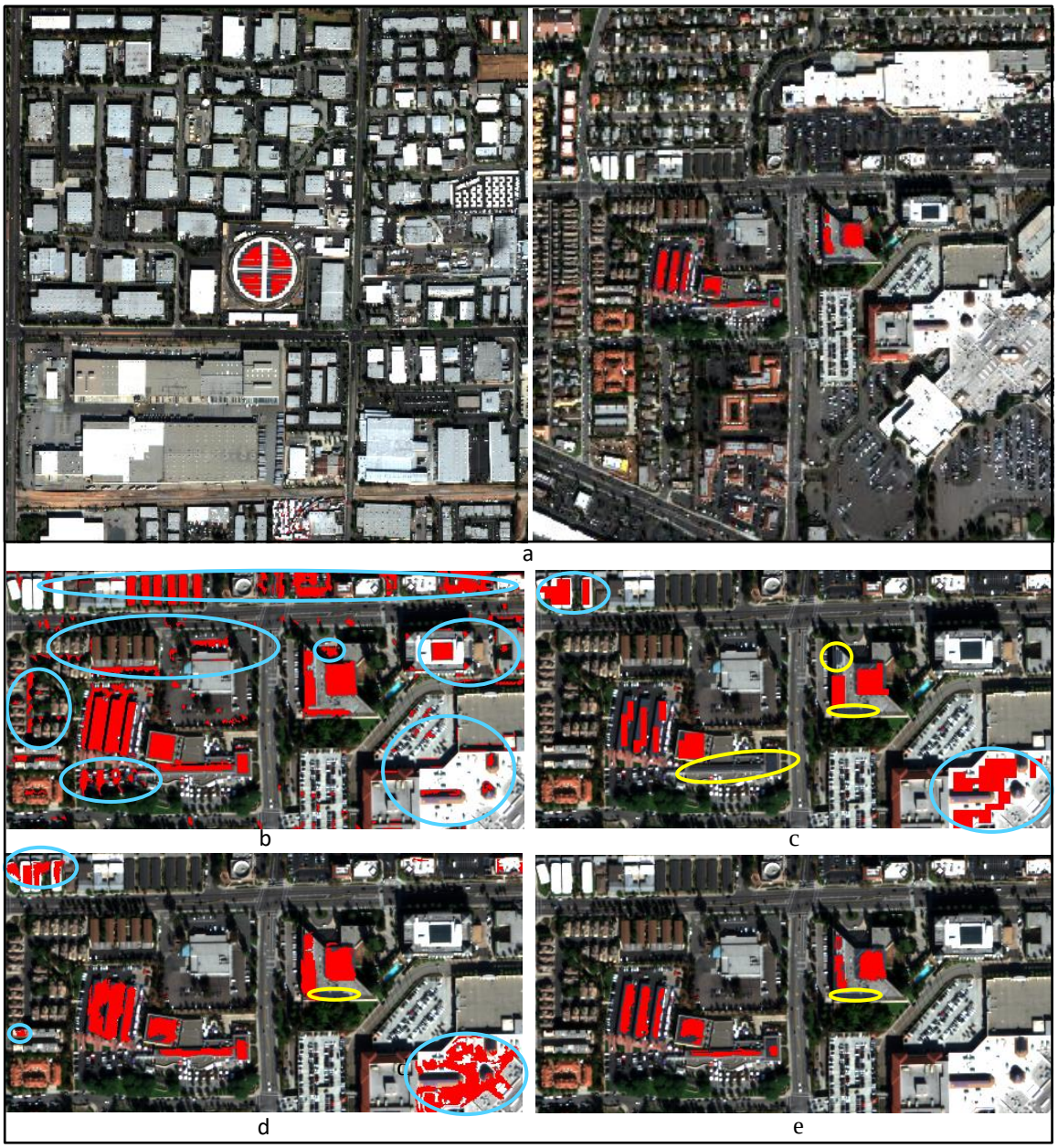

Figure 3.7 Solar PV panel detection results and the comparison (red: detected solar PV panels; yellow circle: missed detection; blue circle: false detection). (a) Solar PV panel detected using the proposed HR-SSF-SAM method, (b) subsection of Solar PV panel detected using VNIR bands, (c) subsection of solar PV panel detected using original (7.5m) SWIR bands, (d) subsection of solar PV panel detected using HR (1.2m) SWIR bands, and (e) subsection of solar PV panel detected using the proposed HR-SSF-SAM method in 16 super spectral (1.2m) bands. (SAM algorithm was used in all of the detections)

3.5.3 Methods for accuracy calculation

3.5.3.1 True detection rate

True detection is the number of solar PV panels correctly detected and the true detection rate is the percentage of correctly detected solar PV panels. The true detection rate (TDR) is computed using equation 3-2.

$$TDR = \frac{NTD}{N} \times 100 \qquad (3\text{-}2)$$

where TDR is true detection rate, NTD is number of true detections, N is total number of solar PV panels in the study area.

3.5.3.2 Missed detection rate

Missed detection is the number of solar PV panels that were not detected and the missed detection rate is the percentage of missed solar PV panel detection. The missed detection rate (MDR) is computed using equation 3-3.

$$MDR = \frac{NMD}{N} \times 100 \qquad (3\text{-}3)$$

where MDR is missed detection rate, NMD is number of missed detections, N is total number of solar PV panels in the study area.

3.5.3.3 False detection rate

False detection is the number of other objects which were falsely detected as solar PV panels and the false detection rate is the percentage of false solar PV panel detection. The false detection rate (FDR) is computed using equation 3-4.

$$FDR = \frac{NFD}{TD} \times 100 \qquad (3\text{-}4)$$

where FDR is false detection rate, NFD is number of false detections, TD is total number of detections.

3.5.4 Accuracy comparison and analysis

Table 3-3 shows the true detections (correctly detected), missed detections (solar PV panel was not detected), and false detections (other object was falsely detected as solar PV panel) using original VNIR bands, original SWIR bands, HR SWIR bands, and super spectral bands, respectively.

Table 3-3 Solar PV panel detection results using original SWIR bands, HR SWIR bands, and super spectral bands.

	True detection	True detection rate	Missed detection	Missed detection rate	False detection	False detection rate
1.2m Original VNIR	15	100%	0	0%	11012	99.9%
7.5m Original SWIR	11	73%	4	27%	11	50%
1.2m HR SWIR	14	93.3%	1	6.7%	16	53.3%
1.2m Super spectral	14	93.3%	1	6.7%	0	0%

3.5.4.1 Solar PV panel detection using VNIR bands

Figure 3.7(b) shows a subset of solar PV detection result using VNIR bands. As shown in **Table 3-3**, true detection, missed detection, and false detection rates were 100%, 0%, and 99.9%, respectively. Although all solar PV panels were accurately detected, there was an extremely high false detection rate. Several other objects such as dark roofs, parking lots,

and roads, which have similar spectrums to that of solar PV panels, were falsely detected as solar PV panels.

3.5.4.2 Solar PV panel detection using original SWIR bands

Figure 3.7(c) shows a subset of solar PV detection result using original SWIR bands. As shown in **Table 3-3**, true detection, missed detection, and false detection rates were 73%, 27%, and 50%, respectively. Because of the large pixel size (7.5m), a high level of spectral mixing was encountered. This led to a number of missed and false detections. Moreover, small solar PV panel installations were not detected because of the 7.5m pixel size.

3.5.4.3 Solar PV panel detection using HR SWIR bands

Figure 3.7(d) shows a subset of solar PV detection result using HR SWIR bands. As shown in **Table 3-3**, true detection, missed detection, and false detection rates were 93.3%, 6.7%, and 55%, respectively. With smaller pixel size (1.2m) the problem of small size solar PV panel detection was solved, i.e. HR SWIR bands with 1.2m pixel size reduced spectral mixing significantly, therefore, small solar PV panel installations can also be detected. However, some other ground objects, such as white roofs, which have similar spectrum to that of solar PV panels, were falsely detected as solar PV panels. Because of the high-resolution, more such objects became apparent which led to more false detections. In summary, true detections increased with HR SWIR bands; however, false detections increased as well.

3.5.4.4 Solar PV panel detection using super spectral bands

Figure 3.7(e) shows a subset of solar PV detection result using super spectral bands. As shown in **Table 3-3**, true detection, missed detection, and false detection rates were 93.3%,

6.7%, and 0%, respectively. The results demonstrated that the use of super spectral bands not only reduced spectral mixing, avoiding missed detections, but also eliminated false detections. False detections were eliminated because some other objects such as white roofs which have similar spectrums to that of solar PV panels in SWIR spectral bands, have different spectrums in super spectral bands.

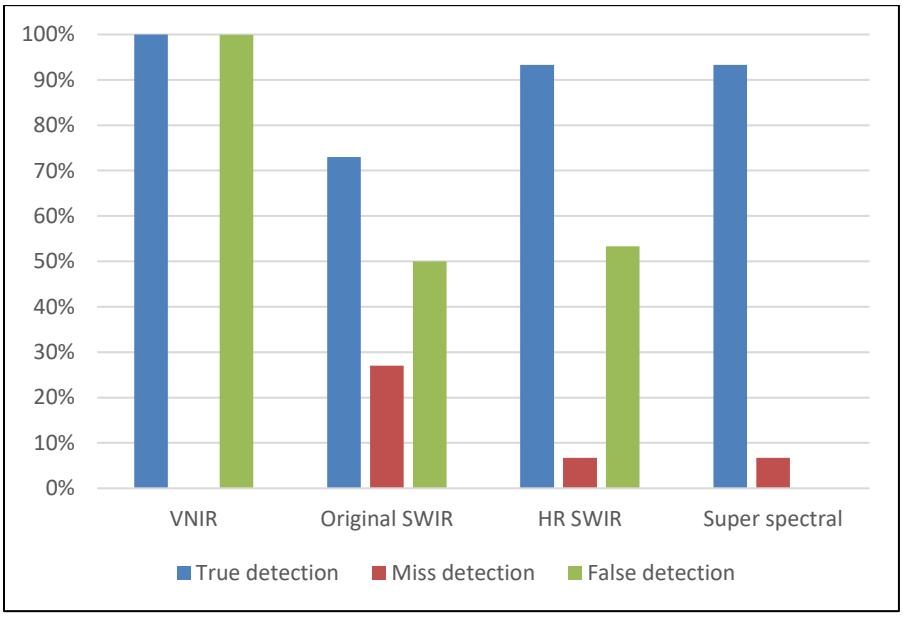

Figure 3.8 Comparison of solar PV panel true detection, miss detection, and false detection rates using VNIR 1.2m, original 7.5m SWIR, HR 1.2m SWIR and 16 super spectral 1.2m bands (HR-SSF-SAM method) respectively.

Based on the detection results shown in **Table 3-3** and detections rate comparison shown in **Figure 3.8**, it can be concluded that the proposed HR-SSF-SAM method can produce high quality solar PV panel detection result. Furthermore, as shown in **Figure 3.9**(a), in a subset of the pan-sharpened image (50cm resolution), there are three solar PV panels installed; however, these were not detected as solar PV panels using the proposed method. When matched with the ground truth, it was found that the three objects that look similar

to solar PV panels in the pan-sharpened image are actually glass roofs installed on a mall (**Figure 3.9**(b)). This shows that using the proposed method, solar PV panels can be differentiated from glass roofs; glass roofs are difficult to differentiate by humans even in very high-resolution images.

Figure 3.9 Glass roofs of Brea mall, Brea California. (a) 0.5m pan-sharpened natural color WorldView-3 image, (b) 3D view of the roof top in Google Earth image.

3.6 Conclusions

The latest high-resolution satellite, WorldView-3, with 1 Pan band, 8 VNIR bands and 8 SWIR bands, significantly increases the potential for detecting solar PV panels in urban environments. However, the experiments conducted for this research found that only using VNIR bands are not sufficient for solar PV panel detection. Although the available SWIR bands of WorldView-3 can provide additional information for solar PV panel detection, it is difficult to detect small solar PV panel installations due to low-resolution (7.5m). It is also difficult to differentiate large solar PV panels from some large roofs made of certain special materials because the spectral information in the original SWIR bands is not sufficient for separating them from each other. In addition, although the detection of small solar PV panel installations can be made possible by utilizing the FGSS algorithm to increase the resolution of available SWIR bands from 7.5m to 1.2m, the resolution increase

also increases the false detection rate due to its inability to separate solar PV panels from roofs with special materials.

Therefore, this research introduced a novel HR-SSF-SAM method to detect solar PV panels using WorldView-3 satellite imagery. The method combines the original 1.2m VNIR bands and the 1.2m HR SWIR bands generated by the FGSS algorithm to form a high-resolution, super spectral image, and then utilizes the spectral similarity detection capacity of the SAM algorithm to identify solar PV panels in the high-resolution, super spectral bands. The detection results show that the proposed HR-SSF-SAM method achieved a true detection rate of 93.3% with a 0% false detection rate. Only one small and very narrow solar PV panel installation was not detected, due to the lack of image spatial resolution. Even solar PV panels and glass roofs can be differentiated from each other by the proposed method, which is difficult for the human eye to achieve. Furthermore, the proposed method is applicable world-wide as spectral characteristics of solar PV panels are similar everywhere.

Similar to the solar PV panels, most of the manmade materials have unique spectrum features in the combined VNIR and SWIR bands, which can be utilized to differentiate materials. Therefore, the proposed HR-SSF-SAM method has the potential to be extended to detect rooftop materials. This extension will be conducted in future research.

3.7 Acknowledgement

The Canada Research Chairs Program funded this research. The original WorldView-3 Pan, VNIR and SWIR images were provided by DigitalGlobe Inc.

3.8 References

Bradbury, K., Saboo, R., Malof, J., Johnson, T., Devarajan. A., Zhang, W., Collins, L., Newell, R. 2016. Distributed Solar Photovoltaic Array Location and Extent Data Set for Remote Sensing Object Identification. *Scientific Data*, 3:160106.

DigitalGlobe, Inc. Exploring the benefits of SWIR satellite imagery, white paper.

Accessed 22 February17:

http://global.digitalglobe.com/sites/default/files/DG_SWIR_WP.pdf

ENVI. 2016. ENVI ver. 5.3 software help document. Boulder, CO: Exelis Visual Information Solutions. Inc., a subsidiary of Harris Corporation.

Fuze Go. 2016. FuzeGo ver. 3.0 software help document. Fredericton, NB: Scene Sharp Technologies Inc.

Hallock, L., Kinman, M. 2015. California's Solar Suc- cess Story: How the Million Solar Roofs Initiative Trans-formed the State's Solar Energy Landscape. *Environment California report.*

Kruse, F.A., Lefkoff, A.B., Boardman, J.W., Heidebrecht, K.B., Shapiro, A.T., Barloon, P.J., Goetz, A.F.H. 1993. Airbone Imaging Spectrometry The spectral image processing system (SIPS)—interactive visualization and analysis of imaging spectrometer data. *Remote Sensing of Environment*, 44 (2), 145-163.

Malof, J. M., Rui Hou., Collins, L. M., Bradbury, K., Newell, R. 2015. Automatic solar photovoltaic panel detection in satellite imagery. *International Conference on Renewable Energy Research and Applications (ICRERA)*, Palermo, pp. 1428-1431.

Young, D. 2015. Use cases for SWIR imagery – taking a closer look – part 1 and 2, DigitalGlobe Inc. Longmont, CO, white paper.

Zhang, Y., 2004. Understanding image fusion. *Photogrammetric Engineering & Remote Sensing*, 70 (6), 657–661.

Zhang, Y., Mishra, R.K. 2014. From UNB PanSharp to Fuze Go – the success behind the pan-sharpening algorithm. *International Journal of Image and Data Fusion*, 5 (1), 39–53.

Chapter 4 : Roofing Material Detection using WorldView-3 Satellite Imagery

Abstract

Detection of roofing material is an important task in urban management and planning. Conventional on-site surveys for roofing material detection are expensive, time consuming, and slower in coping with the new constructions. Therefore, remote sensing becomes an attractive option for roofing material detection. The availability of WorldView-3 imagery, with 16 spectral bands (8 VNIR bands and 8 SWIR bands) plus one panchromatic band, significantly increases the possibility of using satellite remote sensing for roofing material detection. However, successful roofing material detection using WorldView-3 imagery has not been found in a review of the relevant literature yet, because of the coarse resolution of the commercially available SWIR bands (7.5m), the difficulty of integrating SWIR bands with VNIR bands (1.2m), and other technical challenges. This paper introduces a novel method to detect roofing materials, such as fiberglass, ethylene propylene diene monomer (EPDM), metal, and concrete, using WorldView-3 imagery. The method overcomes the coarse resolution problem of the SWIR bands, effectively integrates the SWIR bands with the VNIR bands, and introduces a new approach to detect roofing materials using integrated bands (VNIR+SWIR). Experiments with the WorldView-3 imagery of Brea, California, USA, demonstrates that the proposed method achieves an overall accuracy of 97.59% and Kappa accuracy of 95.59% for roofing material detection in commercial areas, and an overall accuracy of 93.99% and Kappa accuracy of 88.98% for detecting roofing materials of residential houses.

4.1 Introduction

Urban areas have been rapidly growing in the last few decades around the world. Urban areas normally consist of a large variety of land covers with different man-made and natural materials which influence the environment, climate, and energy conditions of a region (Taherzadeh and Shafri, 2013). Roofing materials are some of the important land covers that affect the environment and even the safety of an urban area. For example, information about roofing material is important for various applications such as determining fire prone areas, water flows, disaster preparedness, and pollution sources. In the fire prone areas, insurance companies need to know the roofing materials for their flammability. Hence, detection of roofing materials is one of the important tasks for urban management and planning. However, conventional on-site surveys for roofing material detection are expensive, time consuming, and slower in coping with the new constructions. They are not practical for detecting roofing materials of a large area. Therefore, remote sensing technologies have become an attractive option for detecting roofing materials.

Because each manmade material has unique spectral signatures which can be recorded by hyperspectral bands, research has explored the potential of using hyperspectral data (including field spectroscopy data and hyperspectral imagery) for roofing material detection. For example, Cilia et al. (2015) used aerial hyperspectral images to detect asbestos cement roofs and their weathering status. Hamedianfar et al. (2014) combined data mining algorithm and object-based analysis together to classify urban surface materials in aerial hyperspectral images. Samsudin et al. (2016) applied feature selection algorithms to field spectroscopy data to detect roofing materials. These studies indicated that although aerial hyperspectral imagery and field spectroscopy data provide the best

possible spatial and spectral resolutions for detecting roofing materials, they are expensive and have a limited ground coverage, compared to very high-resolution (VHR) satellite imagery.

Some research works (Taherzadeh and Shafri, 2013; Taherzadeh and Shafri, 2014; Taherzadeh and Shafri, 2015; Taherzadeh and Shafri, 2016) utilized the state-of-the-art object-based classification methods to detect roofing materials in VHR satellite imagery. However, very limited success was achieved with high misclassification errors, due to the lack of necessary spectral information in VHR multispectral imagery.

The launch of WorldView-3 satellite on August 13, 2014, brings a new opportunity for roofing material detection, because it is the first high-resolution satellite to include 8 short wave infrared (SWIR) bands, 8 visible and near infrared (VNIR) bands and 1 panchromatic (Pan) band in the data collection (DigitalGlobe, 2016). However, numerous technical challenges also exist for detecting roofing materials from WorldView-3 imagery. (1) The resolution of the commercially available SWIR bands (7.5m) is too coarse to detect roofing materials of individual family houses. (2) The experiments conducted for this research reveal that just using the 8 SWIR bands is not sufficient to separate roofing materials from some non-roof materials (such as roads and parking lots), (3) A recent study (Samsudin et al., 2016) proved that if just using the 8 VNIR bands and field spectroscopy data, only two types of roofing materials (concrete and metal) can be detected. And, (4) the resolution difference between the VNIR bands (1.2m) and the available SWIR bands (7.5m) is more than 6 times, which creates a challenge to effectively integrate them together for roofing material detection. In the literature review conducted for this research, no publication was

found that demonstrated the ability to detect more than two types of roofing materials (concrete and metal) from the WorldView-3 imagery.

This paper introduces a new method to detect four types of common roofing materials (fiberglass, ethylene propylene diene monomer (EPDM), metal, and concrete) using WorldView-3 imagery. To suppress non-roofing objects such as roads and parking lots, a suppressed non-roofing objects (SNRO) image is created using VNIR bands and the Spectral Angle Mapper (SAM) algorithm (Kruse et al., 1993). To solve the coarse-resolution problem of the available SWIR bands and spectral limitations of either the VNIR bands or the SWIR bands for roofing material detection, the Fuze Go SWIR Sharp algorithm (Fuze Go, 2016) is utilized to increase the resolution from 7.5m to 1.2m, and then integrate 8 original 1.2m VNIR bands are integrated together with the 8 new 1.2m SWIR bands in order to form a 16-band 1.2m super spectral image set. Finally, SAM algorithm is modified to detect roofing materials by utilizing the SNRO image, super spectral imagery, reference spectrums, and non-target reference spectrums. In this paper, a few of the non-roofing objects such as parts of roads and bare earth, which were not suppressed in the SNRO image were defined as non-target objects.

The proposed method was tested using WorldView-3 imagery over the city Brea, California, USA. A commercial area and a residential area were chosen to test the effectiveness of the proposed method. For the commercial area, the overall accuracy and Kappa coefficient of 97.59% and 95.59% respectively were achieved; whereas, for the residential area, overall accuracy and Kappa coefficient of 93.99% and 88.98% respectively were achieved.

The remainder of this paper is organized as follows. Section 4.2 describes the study area and data set; section 4.3 discusses the potential and limitations of VNIR and SWIR bands; section 4.4 introduces and explains the proposed method; the results and accuracy analysis are presented in section 4.5; and the conclusions are given in section 4.6.

4.2 Study area and data set

The study area covers 20 km^2 of the city of Brea, California, USA. The WorldView-3 imagery of the study area was collected in November 2014 and provided by DigitalGlobe. As indicated in **Figure 4.1**, buildings with various sizes are distributed in the study areas among other ground objects. Quick Atmospheric Correction (QUAC) method (ENVI 2016) was applied to the data. QUAC is a VNIR-SWIR atmospheric correction method and works best with scenes that contain man-made structures. The spectral and spatial information of the WorldView-3 image bands is provided in **Table 4-1**.

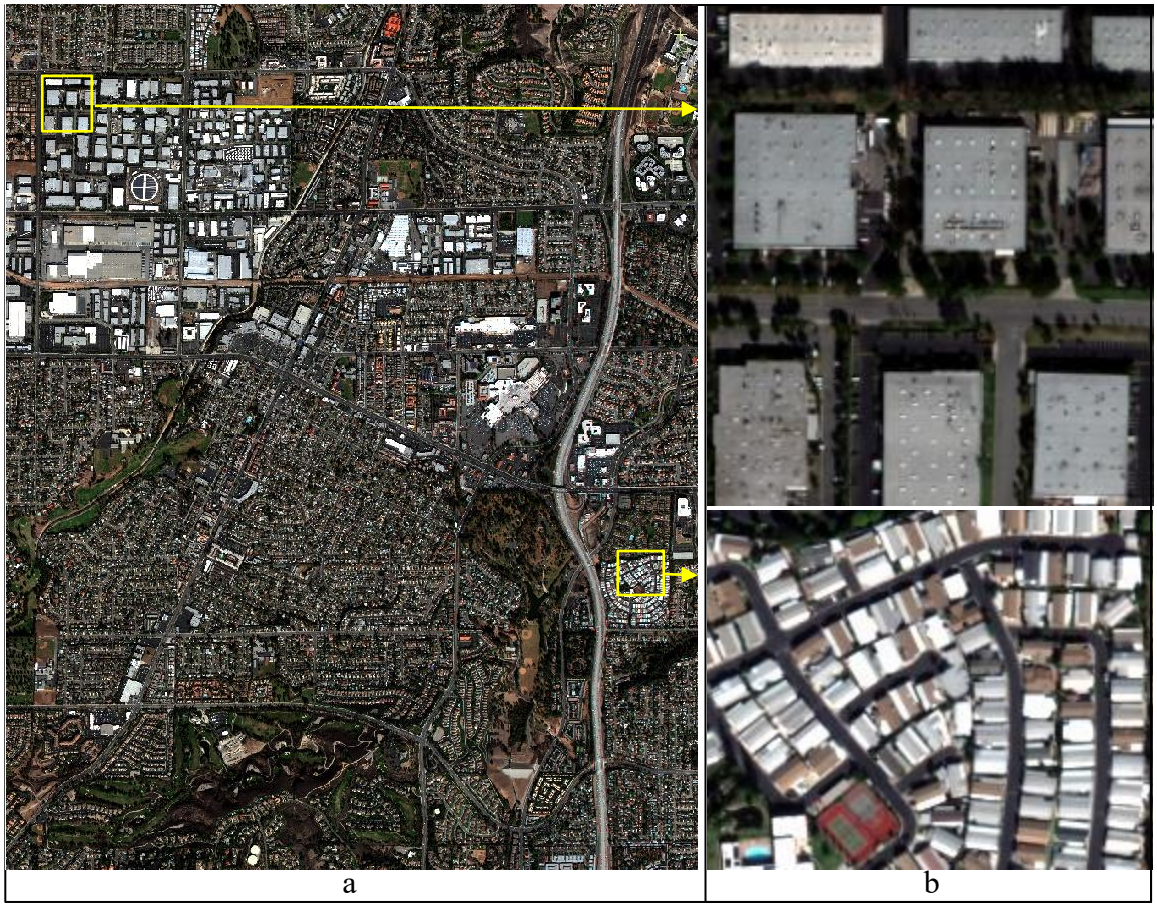

Figure 4.1 Study area and subsections with commercial and residential buildings. (a) Overview of the study area in the 1.2m natural colour image of WorldView-3, and (b) an enlargement showing the commercial and residential buildings.

Table 4-1 Characteristics of the WorldView-3 imagery used in this study.

Band		Spectral range (nm)	Spatial resolution (m)
	Pan	450 - 800	0.5
VNIR	Coastal	400 - 450	1.2
	Blue	450 - 510	1.2
	Green	510 - 580	1.2
	Yellow	585 - 625	1.2
	Red	630 - 690	1.2
	Red Edge	705 - 745	1.2
	NIR-1	770 - 895	1.2
	NIR-2	860 - 1040	1.2
SWIR	SWIR-1	1195 - 1225	7.5
	SWIR-2	1550 - 1590	7.5
	SWIR-3	1640 - 1680	7.5
	SWIR-4	1710 - 1750	7.5
	SWIR-5	2145 - 2185	7.5
	SWIR-6	2185 - 2225	7.5
	SWIR-7	2235 - 2285	7.5
	SWIR-8	2295 - 2365	7.5

The Pan and VNIR bands of WorldView-3 are almost the same as those of WorldView-2. The SWIR bands of WorldView-3 are beyond the near-infrared region falling roughly between 1100 and 3000 nm. The SWIR sensor is strategically designed to capture the unique spectral signatures of certain ground materials (DigitalGlobe, 2016). This opens up a new opportunity to extract more high-resolution information which was not possible before. Particularly, the SWIR spectral bands can significantly improve applications in identification of man-made materials beyond the capacity of VNIR spectral bands. Young (2015) and Kruse et al., (2015) demonstrate the usefulness of WorldView-3 SWIR spectral bands in the identification of man-made materials and minerals.

4.3 Potential and limitation of VNIR and SWIR bands for roofing material detection

4.3.1 Spatial resolution of the SWIR bands

Different roofing materials such as fiberglass, ethylene propylene diene monomer (EPDM), metal, and concreate have unique absorption features in the WorldView-3 SWIR bands; therefore, it increases the possibility of detecting these roofing materials. However, with 7.5m resolution, it is difficult to detect the material of small size residential roofs. As shown in **Figure 4.2**(a) and **Figure 4.2** (b), materials of large roofs can be identified in the 7.5m resolution SWIR bands; but materials of small roofs cannot be identified. On the other hand, as shown in **Figure 4.2** (c), materials of both large and small roofs are clearly visible in 1.2m resolution VNIR bands.

Therefore, in order to detect materials of both small and large roofs, higher resolution SWIR bands are required. In addition, to maximize the application potential of the available

VNIR bands and SWIR bands of WorldView-3 satellite, it is desired to obtain a set of high-resolution SWIR bands that has the same resolution as that of the VNIR bands.

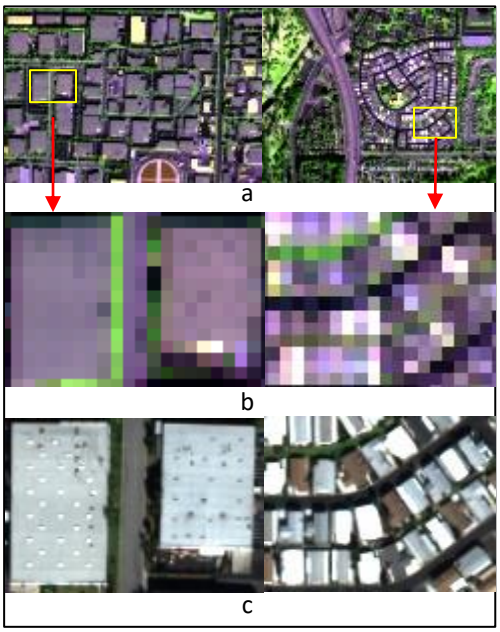

Figure 4.2 Roofs in different spectral images of WorldView-3. (a) Available 7.5m SWIR bands 2, 1, 8 displayed in RGB at 1:1 ratio, (b) enlarged 7.5m SWIR bands, and (c) original 1.2m VNIR bands 5, 3, 2 displayed in RGB. (Small roofs are not visible in the available SWIR bands; however, they are clearly visible in the original VNIR bands.)

4.3.2 Spectral analysis of roofing materials

4.3.2.1 Spectral analysis of VNIR and SWIR bands

Often absorption features of the roofing materials are only apparent in SWIR region of the EMS. Therefore, it is difficult to detect roofing materials using 1.2m resolution WorldView-3 VNIR bands. For example, as shown in **Figure 4.3**(a, b, c and d), in VNIR bands, the spectrums of a fiberglass roof, an EPDM roof, a metal roof, and a concrete roof contain similar or almost the same absorption features (**Figure 4.3**(e)). The only difference

is that they have a slightly different brightness. Therefore, using VNIR bands, it is difficult or impossible for a classifier to differentiate among different roofing materials with similar spectrums. However, these ground materials have unique absorption features in different SWIR bands of WorldView-3. For example, in **Figure 4.3** (f, g, h, i and j), the spectrums of a fiberglass roof, an EPDM roof, a metal roof, and a concrete roof are different in SWIR bands. Therefore, the SWIR bands of WorldView-3 can help differentiate among different roofing materials that cannot be done using VNIR bands.

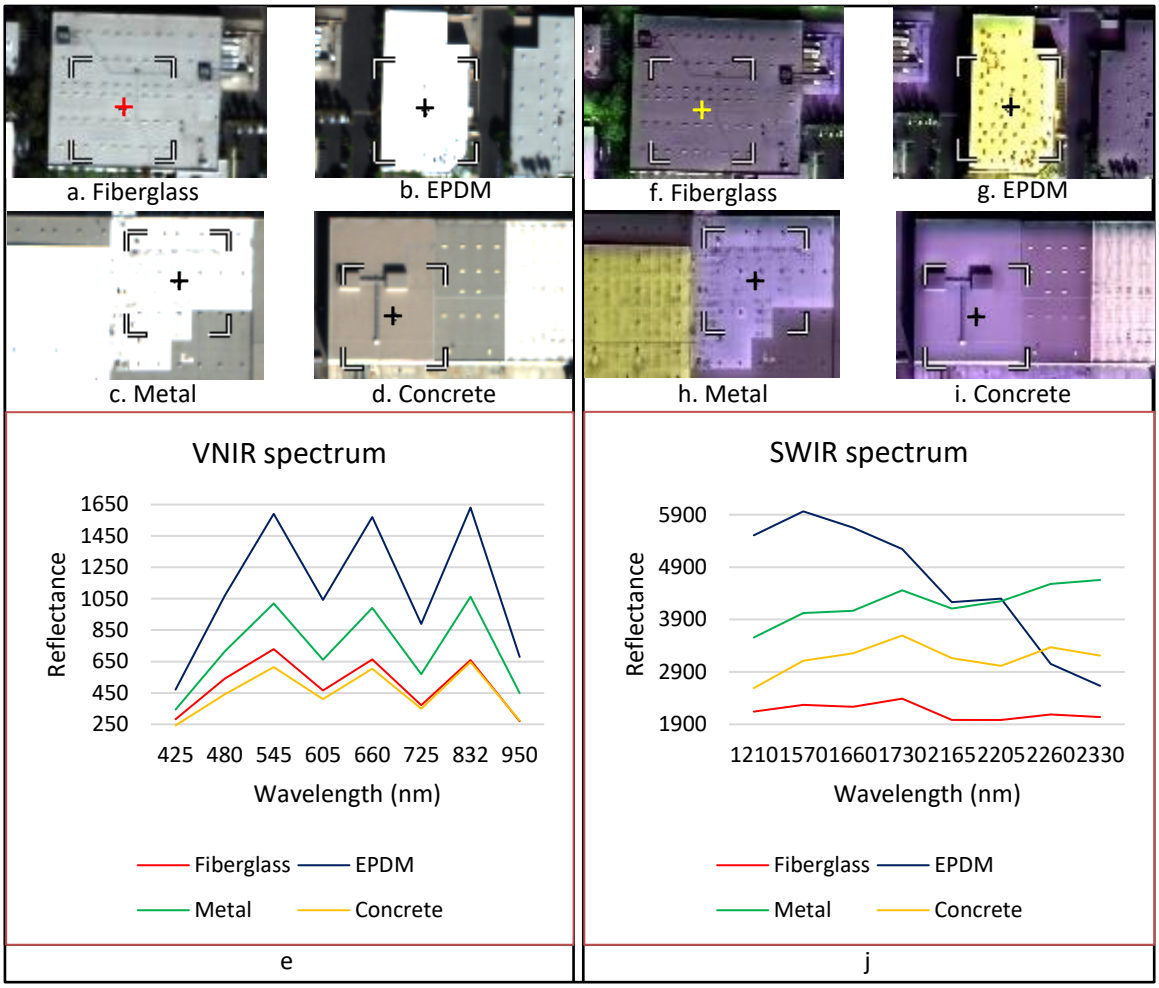

Figure 4.3 Comparisons of the spectrums of a fiberglass roof, a EPDM roof, a metal roof, and a concrete roof in VNIR and SWIR bands. (a) (b) (c) (d) fiberglass roof, EPDM roof, metal roof, and concrete roof in VNIR bands respectively, (e) the spectral curves of the pixels a, b, c, and d (centres of the crosses) in VNIR bands, (f) (g) (h) (i) fiberglass roof, EPDM roof, metal roof, and concrete roof in SWIR bands respectively, and (j) the spectral curves of the pixels f, g, h and i (centres of the crosses) in SWIR bands. (The SWIR bands are 1.2m high-resolution SWIR bands produced using Fuze Go SWIR Sharp to be discussed in the methodology section. The spectrums of fiberglass roof, EPDM roof, metal roof, and concrete roof are similar in VNIR bands; but different in SWIR bands.)

4.3.2.2 Limitations of SWIR bands for roofing material detection

On the other hand, as shown in **Figure 4.4** (d, e, and f), a road and a roof have similar spectra in SWIR bands; whereas, as shown in **Figure 4.4** (a, b, and c), their spectrums in VNIR bands are different. Therefore, using the 8 SWIR bands alone, it will be difficult to differentiate roofing materials from non-roofing materials such as roads, parking lots, and the like.

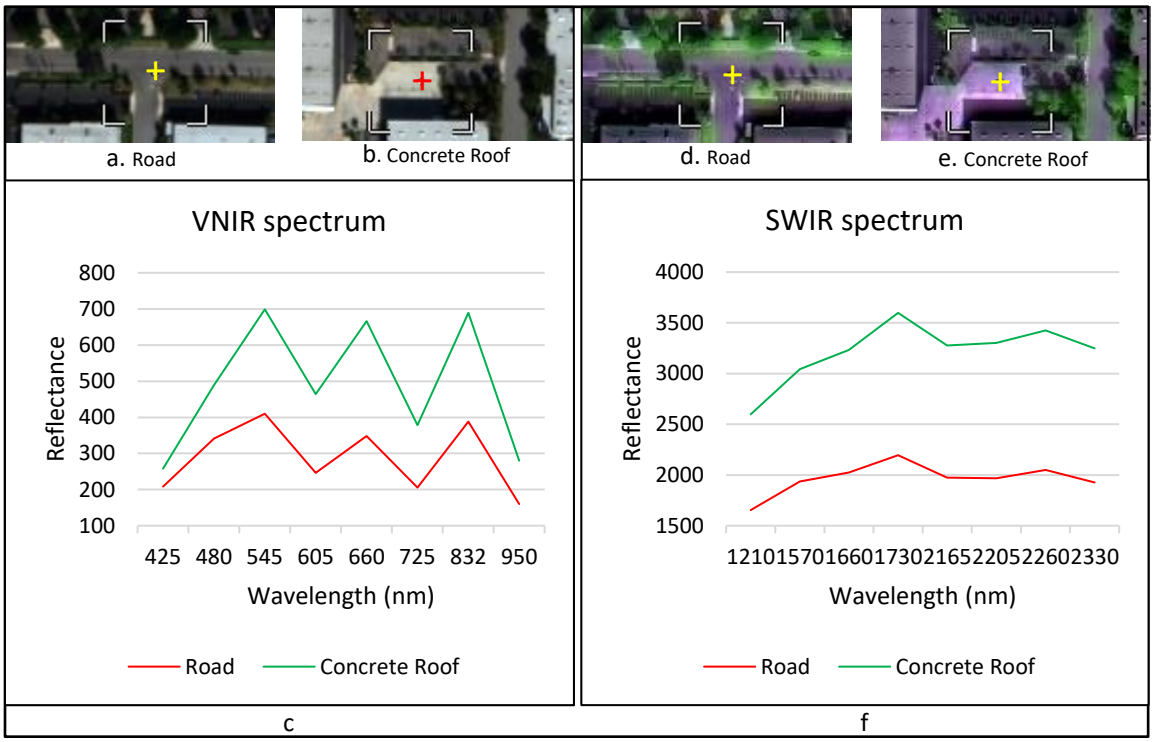

Figure 4.4 Comparison of the spectrums of a road and a concretes roof in VNIR and SWIR bands. (a) and (b) road and concrete roof in VNIR bands respectively, (c) the spectral curves of the road pixel (centre of the cross) and the concrete roof pixels in VNIR bands, (d) and (e) road and concrete roof in SWIR bands respectively, (f) the spectral curves of the road and the concrete roof pixels in SWIR bands. (The road and the concrete roof have similar spectral curves in SWIR bands, whereas they have different spectral curves in VNIR bands.)

4.3.2.3 Necessity of combining VNIR and SWIR bands

Fiberglass, EPDM, metal, and concrete roofs have similar spectrums in VNIR bands, but they have different spectrums in SWIR bands; therefore, SWIR bands can be utilized to detect roofing materials. However, some other ground objects, such as roads, and parking lots have spectrums similar to those of a few roofs in SWIR bands, but different spectrums in VNIR bands. Therefore, it is not possible to achieve a high accuracy roofing material detection using either VNIR bands or SWIR bands.

However, as shown in **Figure 4.3**(e), **Figure 4.3**(j), and in **Figure 4.4**(c), **Figure 4.4**(f), the combination of the VNIR and the SWIR bands can ensure that sufficient spectrum difference can be found in the combined 16 super spectral bands. Therefore, it is necessary to combine the 8 VNIR bands and the 8 SWIR bands together to form a 16 band super spectral image for roofing material detection.

Furthermore, previous studies (Herold et al., 2004; Fiumi et al., 2012; Cilia et al., 2015) have used both VNIR and SWIR hyperspectral bands to detect roofing materials as the combination of VNIR and SWIR bands increases separability among different roofing materials.

4.4 Methodology of roofing material detection

Based on the discussions in section 4.3, a novel method was proposed to detect roofing materials using WorldView-3 imagery. The proposed, method consists of three major components: (1) Non-roofing objects were supressed and a supressed non-roofing objects (SNRO) image was produced by utilising VNIR bands and SAM algorithm (Kruse et al., 1993); (2) a 16 bands super spectral imagery was formed by increasing the spatial

resolution of the 8 SWIR bands from 7.5m to 1.2m (equal to that of the VNIR bands) using FGSS algorithm (Fuze Go, 2016; Zhang, et al., 2016, Zhang and Mishra, 2014; Zhang and Mishra 2012, Zhang, 2004) and combining the 8 original 1.2m VNIR bands with the 8 HR 1.2m SWIR; and (3) SAM algorithm was modified to detect roofing materials by utilising SNRO image, super spectral imagery, reference spectrums, and non-target reference spectrums. The flowchart of the proposed method is shown in **Figure 4.5**.

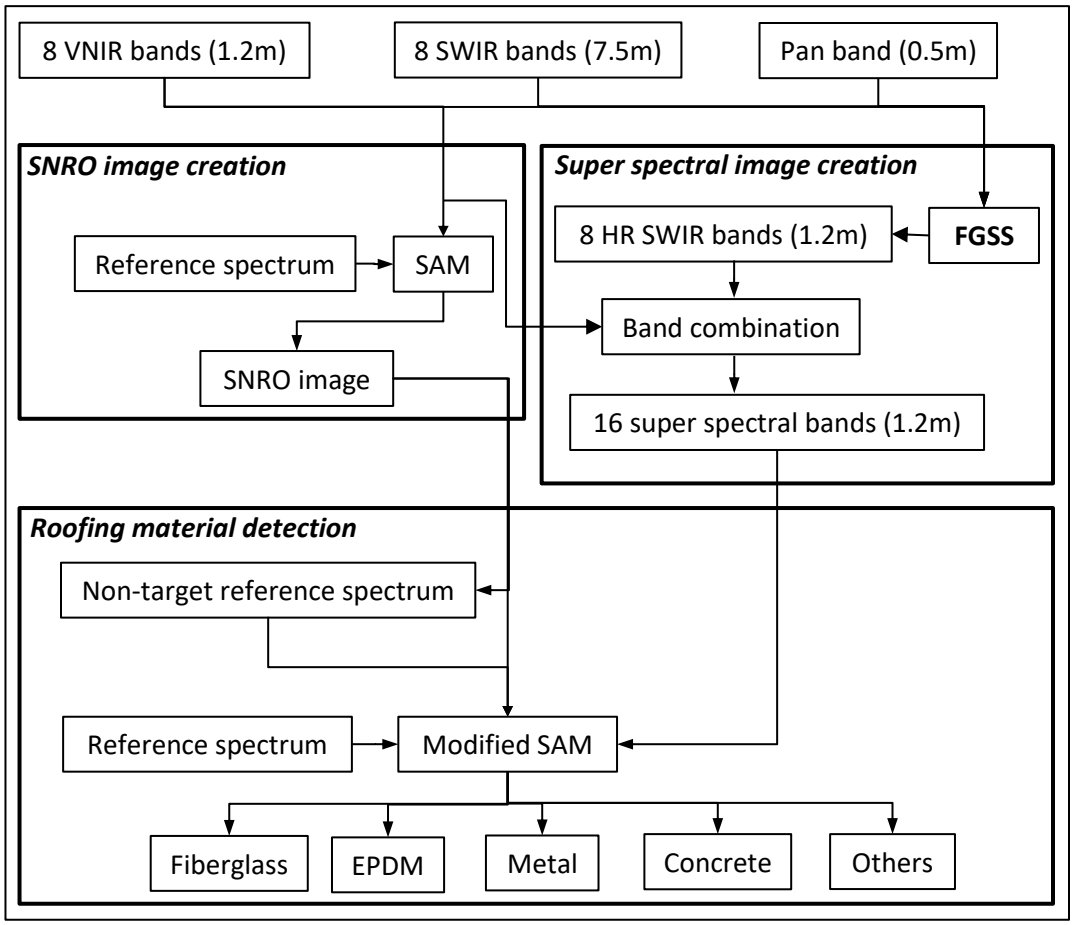

Figure 4.5 Flowchart of the proposed method for roofing material detection.

4.4.1 SNRO image creation

SNRO (suppressed non-roofing objects) image was created using VNIR bands to suppress non-roofing objects from the study area. The spectral angle mapper (SAM) algorithm (Kruse et al., 1993), which determines the spectral similarity between two spectrums, was utilized to generate an SNRO image.

The SAM algorithm performs mapping of the spectral similarity of image spectrum to the reference spectrum which uses an n-dimensional angle to match pixels to reference spectrum (ENVI 2016; Kruse et al., 1993). The algorithm determines the spectrum similarity between two spectrums by calculating the angle between the spectrums and treating them as vectors in a space with dimensionality equal to the number of bands. The smaller angles between the two spectrums indicate high similarity and vice-versa. The reference spectrum can either be attained from the field measurements or taken directly from the image. SAM algorithm is mostly used to identify objects from hyperspectral images as it can identify the ground materials based on their unique spectrum in the hyperspectral bands. Solar illumination and albedo effects do not affect it as it uses only the vector direction and not the vector length. Moreover, it works well in areas of homogeneous regions such as urban environments. Spectrum plot of a reference spectrum and test spectrum for a two-band image is shown in **Figure 4.6**. The angle between reference and test spectrums for an n-band image is calculated using equation 4-1.

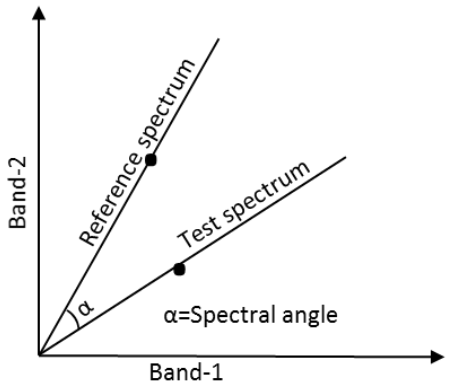

Figure 4.6 Spectral angle between reference and test spectrums for a two-band image (Kruse et al., 1993).

$$\boldsymbol{\alpha = \cos^{-1}\left\{\frac{\sum_{i=1}^{n} X_i Y_i}{\sqrt{\sum_{i=1}^{n} X_i^2}\sqrt{\sum_{i=1}^{n} Y_i^2}}\right\}} \qquad (4\text{-}1)$$

where n is the number of spectral bands, X is the reference spectrum, and Y is the test spectrum.

As discussed in section 4.3.2.3, the spectrums of non-roofing and roofing objects are different in VNIR bands. Therefore, the spectrums of roofing and non-roofing objects in VNIR bands can be utilized to suppress non-roofing objects. In order to suppress non-roofing objects, first, the reference spectrums of roofing objects (fiberglass, EPDM, metal, and concrete roofs) in VNIR bands are taken from the reference spectrum generated in section 4.4.3.1. Spectral angle between each pixel of VNIR image and the reference spectrums were then computed using equation (4-1). This process resulted in four rule images (one for each roofing material) where each pixel of the rule images contains the spectral angle between respective VNIR image pixel spectrum and respective reference spectrum. For example, each pixel of fiberglass rule image contains spectral angle between

a VNIR image pixel spectrum and the fiberglass reference spectrum. Finally, a suppressed non-roofing object (SNRO) image was generated by applying equation (4-2) to each pixel of four rule images. A subset of the resulted SNRO image is shown in **Figure 4.7**. In the equation (4-2), 0.7 radian (4 degree) was used as the threshold (t_F , t_E , t_M , and t_C) value. In the SNRO image, roof pixels were leveled transparent and non-roof pixels were labeled as black color.

$$SNRO(i,j) = \begin{cases} Roof \text{ if } (\alpha_F \le t_F) \wedge (\alpha_E, \alpha_M, \alpha_C > \alpha_F) \\ Roof \text{ if } (\alpha_E \le t_E) \wedge (\alpha_F, \alpha_M, \alpha_C > \alpha_E) \\ Roof \text{ if } (\alpha_M \le t_M) \wedge (\alpha_F, \alpha_E, \alpha_C > \alpha_M) \\ Roof \text{ if } (\alpha_C \le t_C) \wedge (\alpha_F, \alpha_E, \alpha_M > \alpha_C) \\ Non-roof \quad Otherwise \end{cases} \tag{4-2}$$

where $SNRO(i,j)$ is the SNRO image and i and j are row and columns; α_F, α_E, α_M, and α_C are spectral angles between fiberglass reference spectrum and image spectrum, EPDM reference spectrum and image spectrum, metal reference spectrum and image spectrum, and concrete reference spectrum and image spectrum respectively; t_F , t_E , t_M , and t_C are threshold values for fiberglass, EPDM, metal, and concrete respectively.

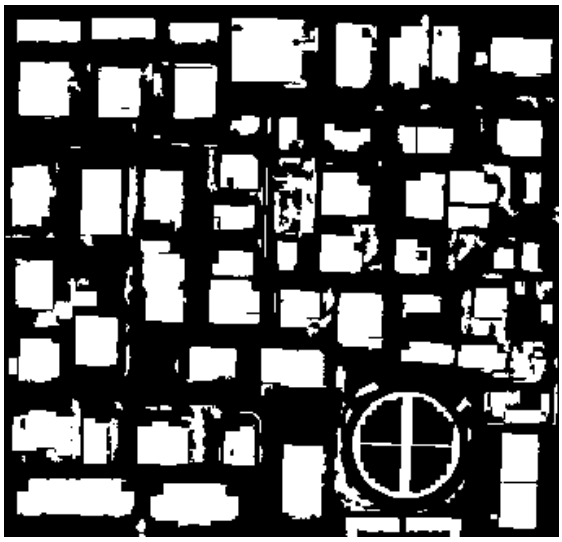

Figure 4.7 SNRO image created using VNIR bands. Most of the non-roofing objects are suppressed in the SNRO image.

4.4.2 Super spectral image formation

As discussed in section 4.3, it is difficult to detect roofing materials using the available SWIR bands (7.5m resolution). It is also desired to obtain a set of SWIR bands that have the same resolution as that of the VNIR bands, to maximize the application potential of the available 16 spectral bands of WorldView-3 satellite. Therefore, the Fuze Go SWIR Sharp (FGSS) algorithm (Fuze Go, 2016) was used to increase the resolution of SWIR bands from 7.5m to 1.2m, to produce high-resolution (HR) SWIR bands.

The FGSS algorithm is an extension of the Fuze Go algorithm (formerly known as UNB pan-sharp) (Fuze Go, 2016; Zhang et al., 2016; Zhang and Mishra, 2014; Zhang and Mishra, 2012; Zhang, 2004). It utilizes the least squares technique to find the best fit between the grey values of the Pan band and the VNIR/SWIR bands to adjust the contribution of individual bands to the fusion. It employs a set of statistical approaches to estimate the grey value relationship between all the input bands to eliminate the problem

of dataset dependency (i.e. reduce the influence of dataset variation in the fusion). In the fusion process original 1.2m VNIR bands, 7.5m SWIR bands, and 0.3m Pan band of WorldView-3 are utilized to generate 1.2m SWIR bands.

Figure 4.8 (a) and **Figure 4.8**(b) show the available 7.5m SWIR image and the 1.2m HR SWIR image generated using FGSS algorithm. It can be seen that the generated 1.2m HR SWIR image not only has the same spectral information as the 7.5m SWIR image, but also has the same spatial resolution as that of the original 1.2m VNIR image (**Figure 4.8**(c)).

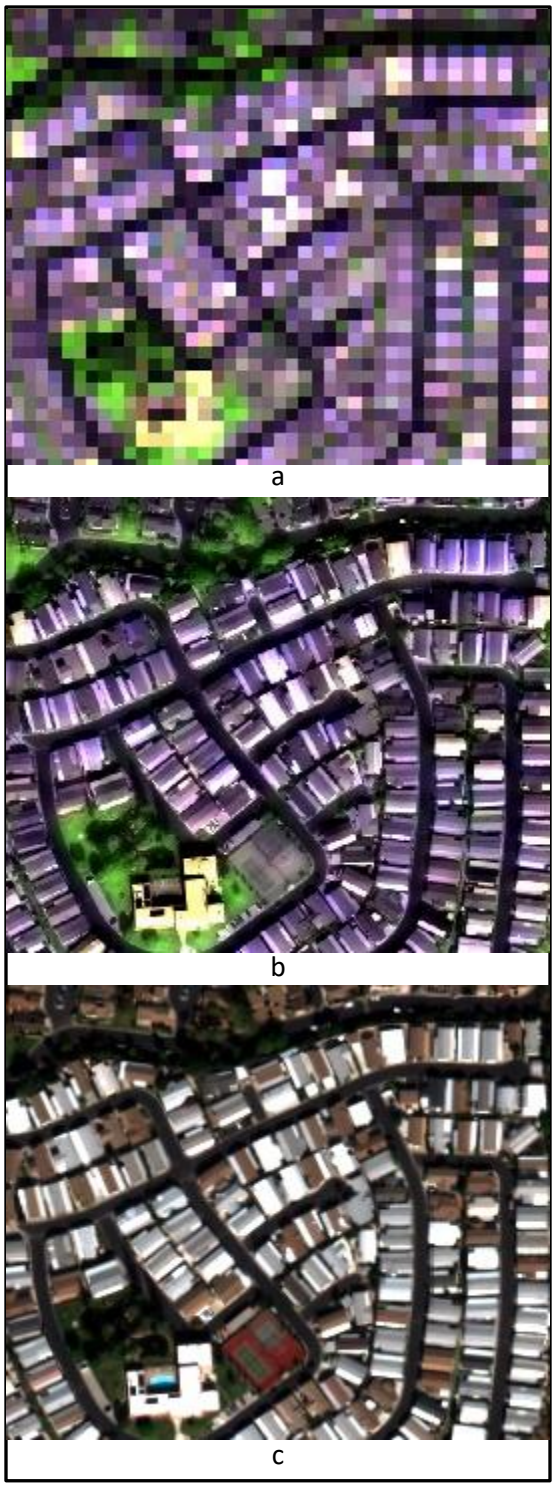

Figure 4.8 Comparison between the available 7.5m SWIR image (a), the 1.2m HR SWIR image generated using FGSS (b), and the original 1.2m VNIR image (c).

As discussed in section 4.3, spectrums of the roofing materials are similar in VNIR bands but different in SWIR bands. However, there are a few other ground objects which have similar spectrums to those of a few roofing materials in SWIR bands but different spectrum in VNIR bands. Spectral analysis of VNIR and SWIR bands shows that the false detection of some ground objects as one of the roofing materials could be avoided in combined VNIR and SWIR bands. Therefore, a high-resolution, 16 band super spectral (VNIR+SWIR) image was generated by combining the eight 1.2m VNIR bands and the eight 1.2m HR SWIR bands together.

4.4.3 Roofing material detection

SAM algorithm was modified to detect roofing materials by utilising SNRO image, super spectral image, reference spectrums, and non-target reference spectrums.

4.4.3.1 Reference spectrums

A small number of training pixels referred to as region of interest (ROI) pixels in super spectral bands were selected from the known fiberglass, EPDM, metal, and concrete roofs in the study area to generate reference spectrums. The reference spectrums were generated by averaging the ROI pixels spectrums to find the optimum reference spectrums. The generated reference spectrums for fiberglass, EPDM, metal, and concrete roofing materials are shown in **Figure 4.9**.

The quality of the roofing material detection is highly dependent on the separability among the reference spectrums; i.e. the larger separability among reference spectrums leads to better detection results. Hence, in order to ensure the separability of the reference spectrums, separability of the selected ROI pixels was computed using Jeffries-Matusita

distance (ENVI, 2016; Jeffreys, 1946) and Transformed Divergence (ENVI, 2016; Richards, 1999) methods. Formulas to compute Jeffries-Matusita distance are given in equation 4-3 and equation 4-4, and formulas to compute Transformed Divergence are given in equation 4-5 and equation 4-6. The computed separability values are shown in **Table 4-2**. Jeffries-Matusita and Transformed Divergence separability values range from 0 to 2.0 and indicate the quality of ROI data pairs. The separability values greater than 1.9 indicate that the ROI data pairs are highly statistically separate. As shown in **Table 4-2**, the separability values for the ROI pixels pairs selected for this study are very high which indicates the highest level of separability among the ROI pixels pairs.

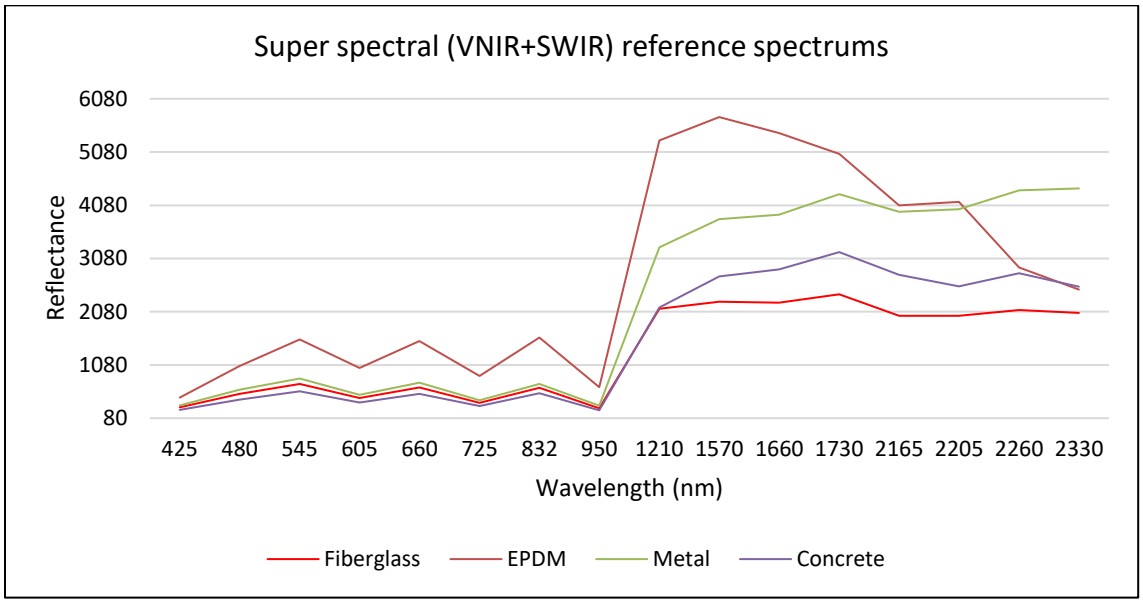

Figure 4.9 Reference spectrums produced from the ROI pixels in the super spectral bands.

$$JMD_{ij} = 2(1 - e^{-\alpha}) \qquad (4\text{-}3)$$

$$\alpha = \frac{1}{8}(\mu_i - \mu_j)^T \left(\frac{C_i + C_j}{2}\right)^{-1} (\mu_i - \mu_j) + \frac{1}{2} ln \left(\frac{\frac{1}{2}|(C_i + C_j)|}{\sqrt{|C_i| \times |C_j|}} \right) \quad (4\text{-}4)$$

where JMD_{ij} is Jeffries-Matusita distance between two reference spectrums i and j; α is the angle; μ_i and μ_j are mean vector of reference spectrums i and j respectively; C_i and C_j are covariance matrices of reference spectrums i and j respectively; T is the transposition function.

$$TD_{ij} = 2\left[1 - exp\left(\frac{-D_{ij}}{8}\right)\right] \quad (4\text{-}5)$$

$$D_{ij} = \frac{1}{2} tr\left[(C_i - C_j)(C_i^{-1} - C_j^{-1})\right] + \frac{1}{2} tr\left[(C_i^{-1} - C_j^{-1})(\mu_i - \mu_j)(\mu_i - \mu_j)^T\right] \quad (4\text{-}6)$$

where TD_{ij} is Transformed Divergence between two reference spectrums i and j; D_{ij} is distance between two reference spectrums i and j; μ_i and μ_j are mean vector of reference spectrums i and j respectively; C_i and C_j are covariance matrices of reference spectrums i and j respectively; *tr* is the trace function; T is the transposition function.

Table 4-2 Jeffries-Matusita distance and Transformed Divergence separability measurements among different roofing materials ROI pixels.

		Fiberglass	EPDM	Metal	Concrete
Fiberglass	JMD	0	2.0	2.0	2.0
	TD	0	2.0	2.0	2.0
EPDM	JMD	2.0	0	2.0	2.0
	TD	2.0	0	2.0	2.0
Metal	JMD	2.0	2.0	0	2.0
	TD	2.0	2.0	0	2.0
Concrete	JMD	2.0	2.0	2.0	0
	TD	2.0	2.0	2.0	0
JMD: Jeffries-Matusita distance; TD: Transformed Divergence					

4.4.3.2 Non-target material reference spectrum

In the SNRO image (**Figure 4.7**), most of the non-roofing materials were suppressed; however, still there are a few non-roofing objects which were not suppressed. The experiment results reveals that there are a few other ground objects such as a few roads and bare earth which have similar reflectance to that of the concrete roofs in both VNIR and SWIR bands. For example, in **Figure 4.10** (a, b, c, and d), the spectrums of the concrete roof, road, bare earth are similar in the super spectral bands. Therefore, based on their spectrums, the road and bare earth pixels will falsely be detected as concrete.

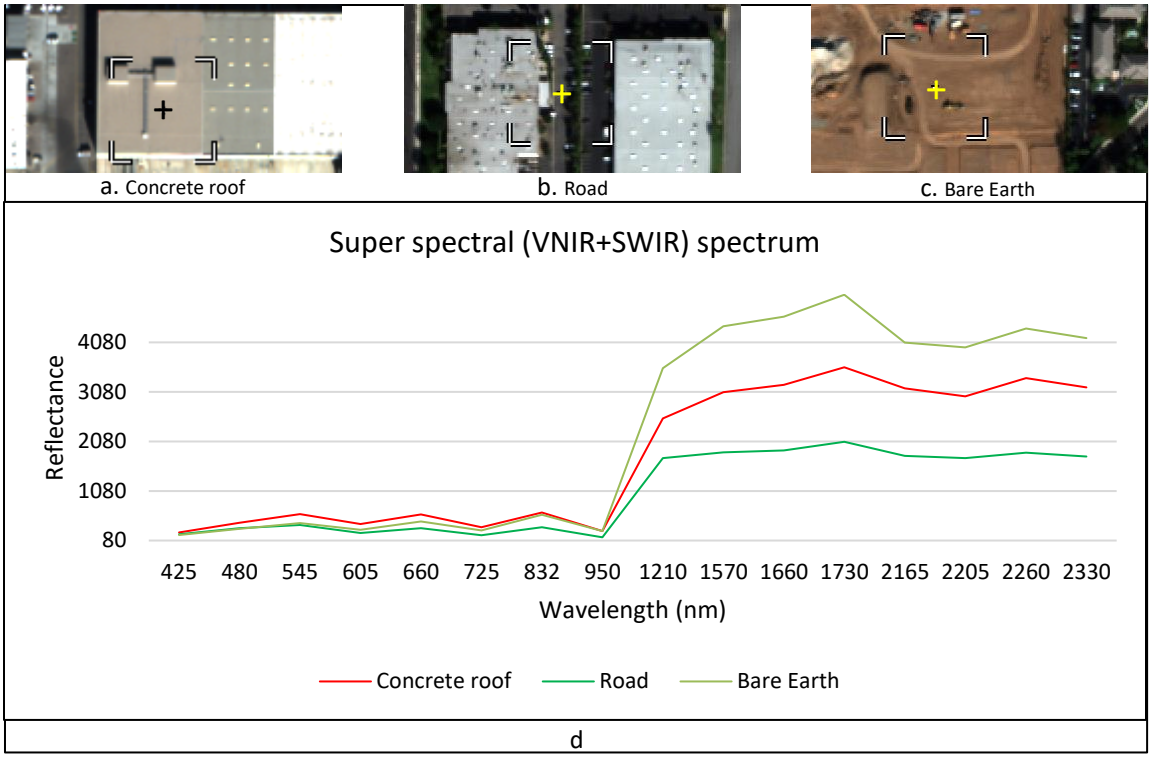

Figure 4.10 Comparison of the spectrums of a concrete roof, road and barren land in super spectral bands. (a) (b) (c) concrete roof, road, and bare earth in super spectral bands respectively, (d) the spectral curves of the pixels a, b, and c (centres of the crosses) in super spectral bands. (The spectrums of concrete roof, road, and bare earth are similar in super spectral bands.)

All pixels of a roofing material ideally should have the same spectrums; however, in reality, there are slight differences in the spectrums of those pixels. Therefore, to optimally detect the roofing materials, the SAM algorithm requires a threshold value as maximum acceptable angle between the reference spectrum vector and the test spectrum vector. Pixels further away than the specified maximum angle threshold are not detected. However, the threshold value also leads to false detections when the angle between the reference spectrum vector and the spectrum vector of other ground materials come within the range

of the specified threshold value. For example, the spectral angle between the concrete reference spectrum (**Figure 4.9**) and the road pixels spectrum (**Figure 4.10**) is 0.054 radians and the spectral angle between the concrete reference spectrum (**Figure 4.9**) and the bare earth pixels spectrum (**Figure 4.10**) is 0.06 radians. Therefore, with a threshold 0.07 radian, both road and bare earth pixels will falsely be detected as concrete.

Therefore, to eliminate the false detection problem, road and bare earth were identified as non-target materials for the study area. Mean reference spectrums of non-target materials were generated in super spectral bands using region of interest (ROI) pixels selected from the study area (shown in **Figure 4.11**).

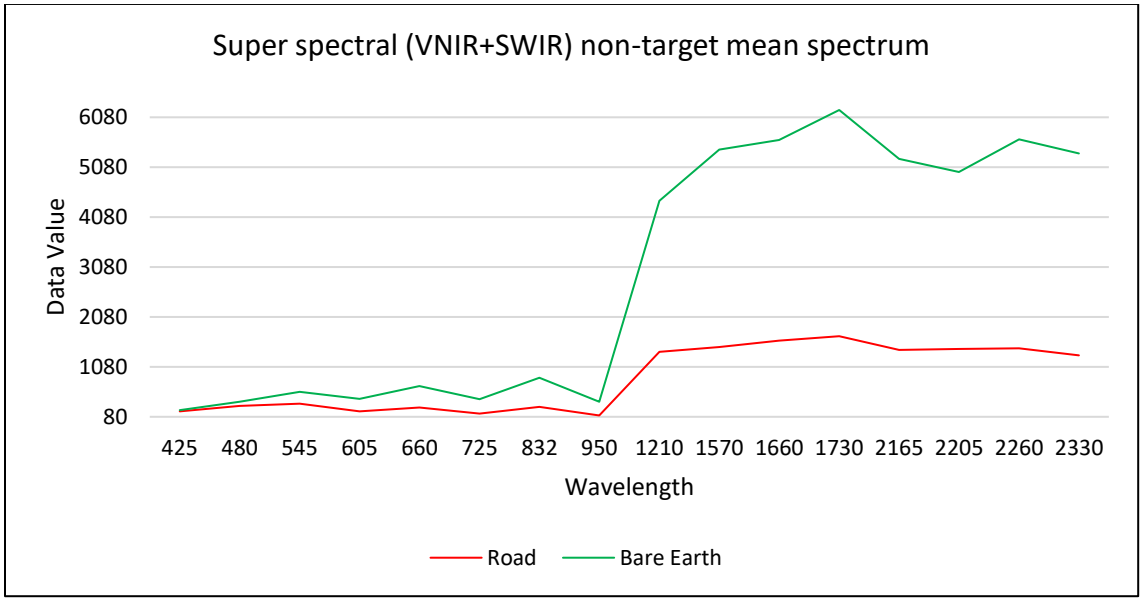

Figure 4.11 Non-target reference spectrums produced from the ROI pixels of the non-target objects (road and bare earth).

4.4.3.3 Roofing material detection

The SAM (Kruse et al., 1993) algorithm was modified to utilize the SNRO image, super spectral image, reference spectrums, and non-target reference spectrums to detect roofing materials. In the modified SAM algorithm, the SNRO image was used to suppress the non-roofing objects such as roads and parking lots in the super spectral image using equation (4-7) and a modified super spectral image was generated. A section of the modified super spectral image is shown in **Figure 4.12**.

$$SSI'(i,j) = SSI(i,j) - SNRO(i,j) \qquad (4\text{-}7)$$

where $SSI'(i,j)$ is the modified super spectral image with suppressed non-roofing objects and i and j are rows and columns; *SSI* is the super spectral image; SNRO is the suppressed non-roofing objects image (shown in **Figure 4.7**).

Figure 4.12 Modified super spectral image

The spectral angle between each pixel of the modified super spectral image and reference spectrums (reference spectrums and non-target reference spectrums) were computed using equation (4-1). Spectral angles of the modified super spectral image pixels which were suppressed using equation (4-7) were not computed. This process resulted in six rule images (four rule images for four types of roofing materials and two rule images for non-target materials) where each pixel of the rule images contains the spectral angle between the respective super spectral image pixel spectrum and the respective reference spectrum. For example, each pixel of fiberglass rule image contains the spectral angle between the super spectral image pixel spectrum and the fiberglass reference spectrum. The final output image was computed by applying equation (4-8) to each pixel of six rule images. In equation (4-8), 0.7 radians (4 degrees) was used as the threshold (t_F , t_E , t_M , t_C , t_{NT1} , and t_{NT2}) value. In the final output image, fiberglass, EPDM, Metal, and Concrete pixels were leveled as red, green, blue, and yellow colors respectively and other pixels were labeled as black color.

$$I(i,j) = \begin{cases} Fiberglass \text{ if } (\alpha_F \le t_F) \wedge (\alpha_E, \alpha_M, \alpha_C, \alpha_{NT1}, \alpha_{NT2} > \alpha_F) \\ EPDM \text{ if } (\alpha_E \le t_E) \wedge (\alpha_F, \alpha_M, \alpha_C, \alpha_{NT1}, \alpha_{NT2} > \alpha_E) \\ Metal \text{ if } (\alpha_M \le t_M) \wedge (\alpha_F, \alpha_E, \alpha_C, \alpha_{NT1}, \alpha_{NT2} > \alpha_M) \\ Concrete \text{ if } (\alpha_C \le t_C) \wedge (\alpha_F, \alpha_E, \alpha_M, \alpha_{NT1}, \alpha_{NT2} > \alpha_C) \\ Others \text{ if } (\alpha_{NT1} \le t_{NT1}) \wedge (\alpha_F, \alpha_E, \alpha_M, \alpha_C, \alpha_{NT2} > \alpha_{NT1}) \\ Others \text{ if } (\alpha_{NT2} \le t_{NT2}) \wedge (\alpha_F, \alpha_E, \alpha_M, \alpha_C, \alpha_{NT2} > \alpha_{NT2}) \\ Others \quad \text{Othervise} \end{cases} \tag{4-8}$$

where $I(i,j)$ is the output image and *i* and *j* are rows and columns; α_F, α_E, α_M, α_C, α_{NT1}, and α_{NT2} are spectral angles between the fiberglass reference spectrum and the image spectrum, the EPDM reference spectrum and the image spectrum, the metal reference spectrum and the image spectrum, the concrete reference the spectrum and the image

spectrum, the non-target-1 reference spectrum and the image spectrum, and the non-target-2 reference spectrum and the image spectrum, respectively; t_F, t_E, t_M, t_C, t_{NT1}, and t_{NT2} are threshold values for fiberglass, EPDM, metal, concrete, non-target-1, and non-target-2, respectively.

For result comparison purposes, first, the SAM algorithm was applied to the 1.2m VNIR bands, original 7.5m SWIR bands, 1.2m HR SWIR bands, and the 1.2m super spectral bands for the roofing material detection, using the same ROI pixels and processing parameters. **Table 4-3** shows the number of ROI pixels used to detect roofing materials in VNIR bands, original SWIR bands, HR SWIR bands, and super spectral bands (Because the 7.5m SWIR image has a significantly lower resolution, the total number of pixels and the training pixels are also significantly fewer). The proposed method was then used to detect roofing material using the 1.2m VNIR and the 1.2m super spectral bands. As the proposed method also used the non-target reference spectrums in addition to the reference spectrums, the number of non-target ROI pixels used to detect non-target materials is shown in **Table 4-3**.

Table 4-3 Total number of pixels of the study area and the number of ROI pixels used to generate reference spectrums of roofing materials and non-target materials from the original 1.2m VNIR, original 7.5m SWIR, and 1.2m super spectral bands.

		Fiberglass	EPDM	Metal	Concrete	Non-target-1 (Road)	Non-target-2 (Bare earth)
1.2m VNIR, 1.2m HR SWIR, and 1.2m Super spectral	No. of ROI pixels	79	78	92	82		
	% of the test areas	0.0006%	0.0006%	0.0007%	0.0006%		
7.5m SWIR	No. of ROI pixels	12	13	9	11		
	% of the test areas	0.0035%	0.0037%	0.0026%	0.0032%		
1.2m VNIR, and 1.2m super spectral (proposed frame work)	No. of ROI pixels	79	78	92	82	33	74
	% of the test areas	0.0006%	0.0006%	0.0007%	0.0006%	0.0002%	0.0005%
Total number of pixels in the study area: **13377536 (1.2m image) and 343088 (7.5m image)**							

4.5 Results and discussions

4.5.1 Ground truth collection

Very high-resolution (approximately 5cm spatial resolution) and high quality aerial photos of Brea, California, USA that are available on Google Earth and Street View were used for ground truth extraction. In the aerial photos, individual roofs can be clearly seen and therefore based on their color, texture, and structure of the building roofs, their roofing materials can be mannualy identified.

To demonstrate the effectiveness of the proposed method, two test areas (commercial and residential) were selected from the study area for accuracy assessment. Building roofs made with fiberglass, EPDM, metal, and concrete in the two test areas were identified and delineated by an image analyst using Google Earth imagery and Google street view. The color, texture and structure information in the aerial photos and Google street view were utilized for the roofing material interpretation. Ground truths delineated with different colors are shown in the **Figure 4.13**. Furthermore, the spectrum of each roof was compared with the reference spectrum (**Figure 4.10**) of fiberglass, EPDM, metal, and concrete to make sure the manually identified roofing materials are correct. **Table 4-4** shows the total number of different roofing materials identified in the two test areas.

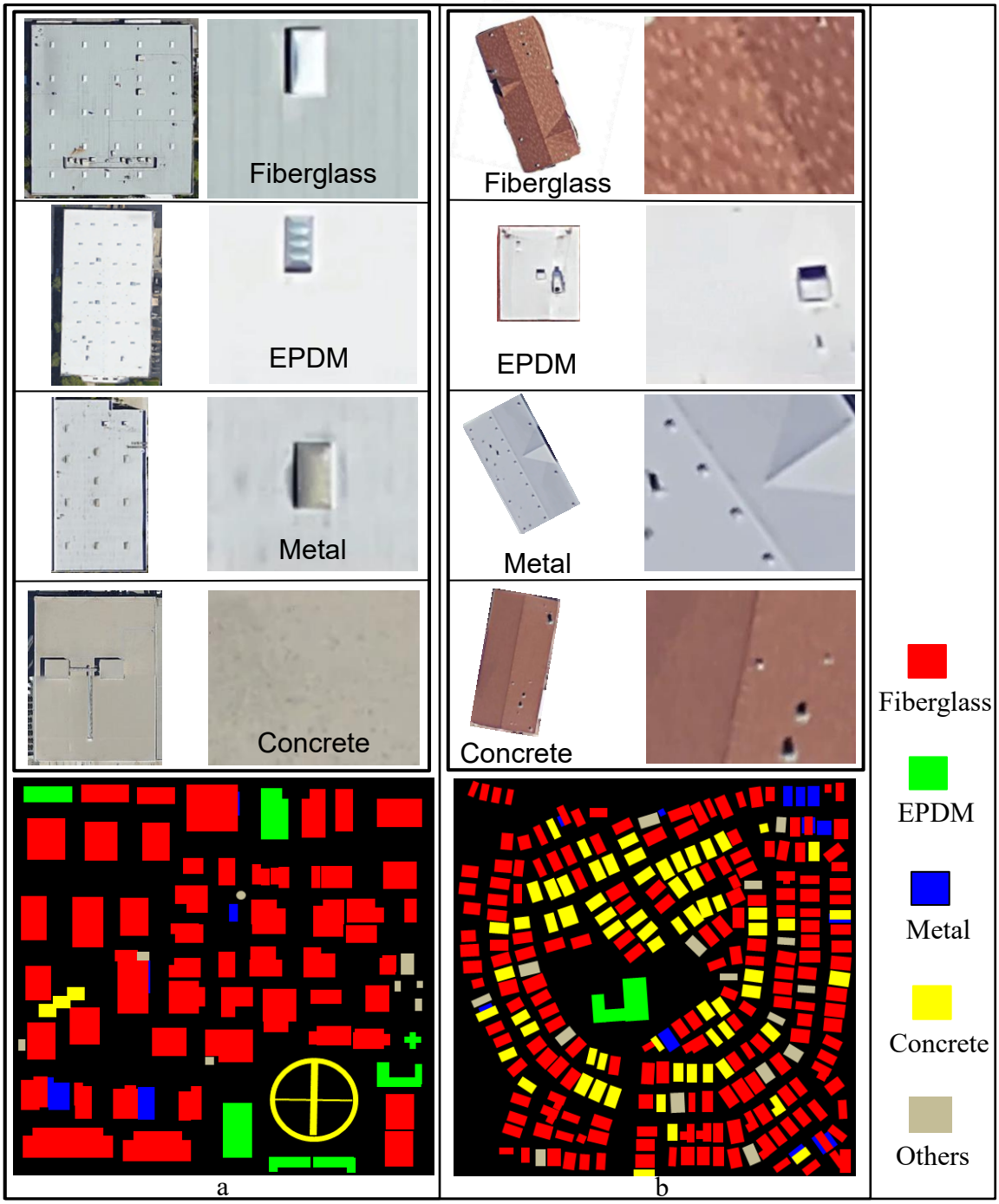

Figure 4.13 Texture and color of different roofing materials and ground truth image of two test areas. (a) textures of different types of roofing materials in the Test Area-1 (commercial) and ground truth

image; (b) textures of different types of roofing materials in the Test Area -2 (residential) area and ground truth image.

Table 4-4 The total number of different roofing materials identified in the two test areas.

	Test area-1	Test area-2
Fiberglass	52	183
EPDM	8	4
Metal	5	14
Concrete	6	66
Others	8	16

4.5.2 Roofing material detection results

Figure 4.14 (b,c,d,e) shows the roofing material detection results in the Test Area-1 using different data sets and **Figure 4.14**(f) shows the roofing material detection results using the proposed method. Whereas **Figure 4.15**(b,c,d,e) shows the roofing material detection results in the Test Area-2 using different data sets and **Figure 4.15**(f) shows the roofing material detection results using the proposed method.

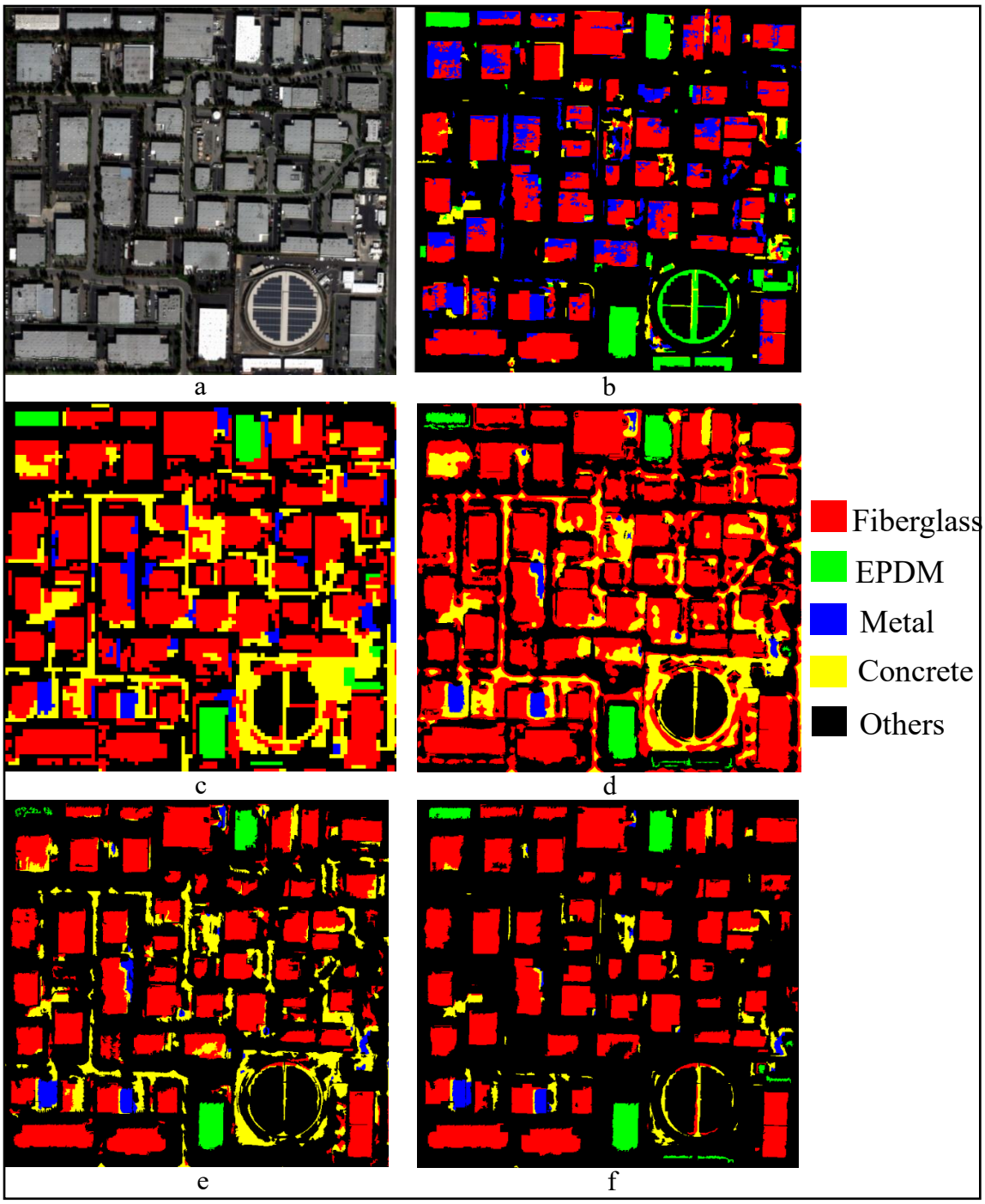

Figure 4.14 Roofing material detection results and the comparison for the study area-1 (commercial buildings). (a) RGB image of the study area-1, (b) roofing materials detected using VNIR bands, (c) roofing materials detected using original (7,5m) SWIR bands, (d) roofing materials detected using HR (1.2m) SWIR bands, (e) roofing materials detected using 16 super spectral (1.2m) bands, and (f) roofing

materials detected using the proposed framework. Results shown in (b), (c), (d), and e) were generated using the SAM algorithm; the result shown in (f) were generated using the proposed method.

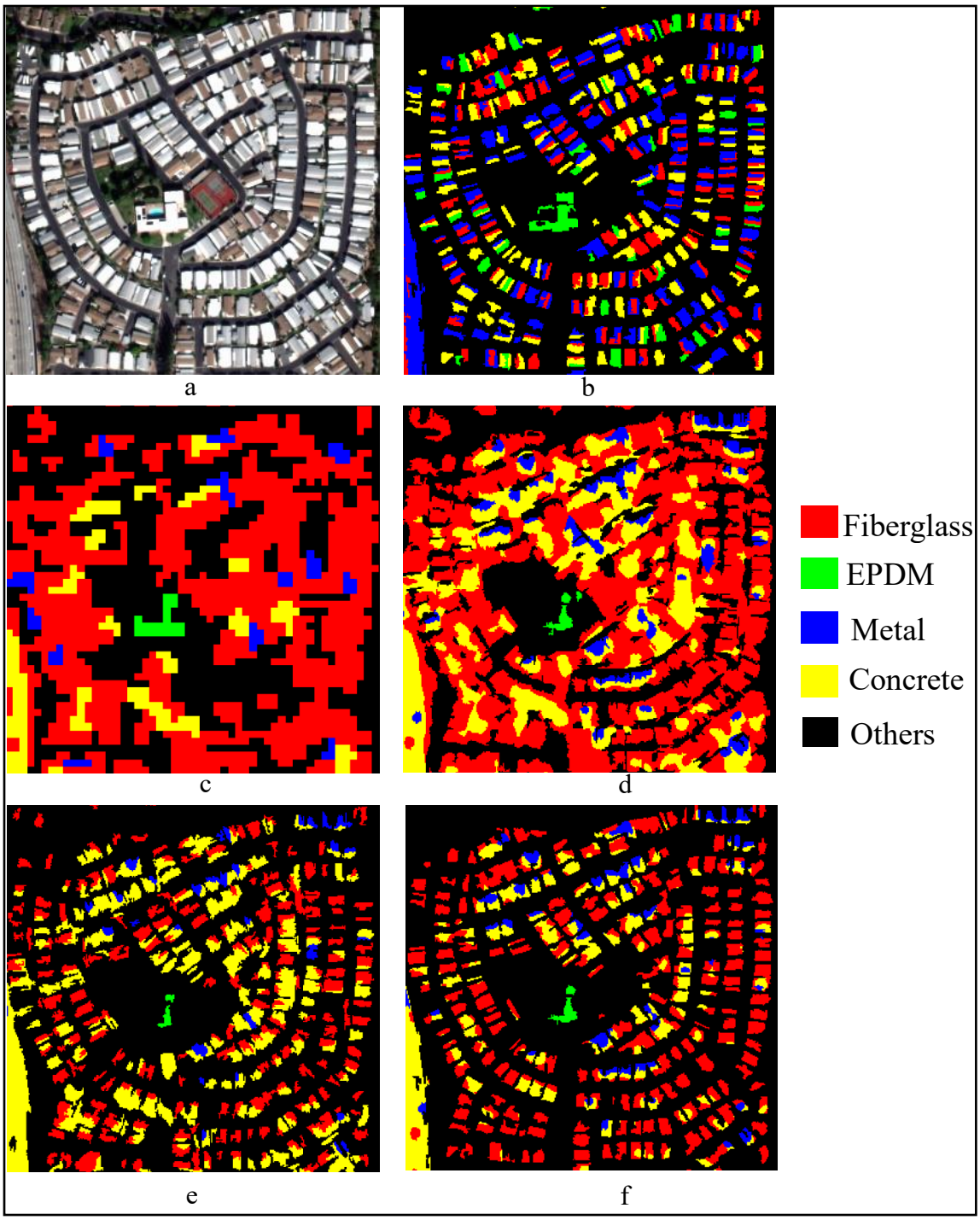

Figure 4.15 Roofing material detection results and the comparison for the study area-2 (residential buildings). (a) RGB image of the study area-1, (b) roofing materials detected using VNIR bands, (c) roofing materials detected using original (7,5m) SWIR bands, (d) roofing materials detected using HR

(1.2m) SWIR bands, (e) roofing materials detected using 16 super spectral (1.2m) bands, and (f) roofing materials detected using the proposed framework. Results shown in (b), (c), (d), and e) were generated using the SAM algorithm, and the result shown in (f) was generated using the proposed method.

4.5.3 Accuracy comparison and analysis

The accuracy assessments of roofing material detections were done using the conventional error matrix (Congalton and Green 2009) and it elements including producer accuracy (PA), user accuracy (UA), overall accuracy (OA), and kappa coefficient (KC). **Table 4-5** shown the PA, UA, OA, and KC computed for Test Area-1; whereas,**Table 4-6** shows the PA, UA, OA, and KC computed for Test Area-2. Non-roofing object detection rates (NRODR) using each data set was calculated using equation (4-9) and are shown in **Table 4-7**. **Figure 4.16**(a) and **Figure 4.16**(b) show the accuracy comparisons for the Test Area-1 and Test Area-2, respectively.

Table 4-5 PA, UA, OA, and Kappa of the Test Area-1 for VNIR bands, original SWIR bands, HR SWIR bands, super spectral bands and, the proposed method.

	1.2m VNIR	7.5m SWIR	1.2m SWIR	1.2m super spectral	Proposed Method
Roofing materials	**PA** **UA**	**PA** **UA**	**PA** **UA**	**PA** **UA**	**PA** **UA**
Fiberglass	98.11 50.00	91.37 80.30	88.33 89.83	96.36 91.37	100.0 96.36
EPDM	33.33 53.84	100.0 75.0	100.0 50.00	100 37.5	100.0 100.0
Metal	11.32 85.71	45.45 100.0	75.00 100.0	85.71 100.0	100.0 100.0
Concrete	18.75 30.0	40.00 85.71	50.00 60.00	38.46 62.5	75.00 100.0
Others	0.00 0.00	60.00 33.33	44.44 50.00	66.66 80.00	100.0 100.0
OA	**47.22**	**76.84**	**78.94**	**83.33**	**97.59**
Kappa	**24.05**	**57.73**	**63.27**	**70.78**	**95.59**

Table 4-6 PA, UA, OA, and Kappa of the Test Area-2 for VNIR bands, original SWIR bands, HR SWIR bands, super spectral bands and, the proposed method.

	1.2m VNIR	**7.5m SWIR**	**1.2m SWIR**	**1.2m super spectral**	**Proposed method**
Roofing materials	**PA** **UA**	**PA** **UA**	**PA** **UA**	**PA** **UA**	**PA** **UA**
Fiberglass	76.96 33.09	68.90 44.80	89.22 81.42	97.88 75.95	99.41 93.44
EPDM	7.84 100.0	100.0 100.0	100.0 100.0	100.0 100.0	100.0 100.0
Metal	6.34 66.66	22.72 35.71	58.33 100.0	92.30 85.71	85.71 85.71
Concrete	27.55 29.91	55.17 24.24	67.12 69.01	70.78 95.45	96.92 95.45
Others	58.33 87.50	0.0 0.0	15.00 18.75	28.57 62.50	57.14 100.0
OA	**35.50**	**37.80**	**76.04**	**80.56**	**93.99**
Kappa	**9.69**	**8.32**	**57.29**	**67.21**	**88.98**

$$NRODR = \frac{NNROD}{TD} \times 100 \qquad (4\text{-}9)$$

where NRODR is non-roofing object detection rate, NNROD is number of non-roofing object detections, TD is total number of detections (both roofing and non-roofing objects).

Table 4-7. Non-roofing object detection rates (NRODR) of the Test Area-1 and Test Area-2 for VNIR bands, original SWIR bands, HR SWIR bands, super spectral bands and, the proposed methods.

		1.2m VNIR	7.5m SWIR	1.2m SWIR	1.2m superspectral	Proposed Method
Non-roofing object detection rate (NRODR)	**Test area-1**	29.41%	56.01%	62.89%	39.18%	16.16%
	Test area-2	4.20%	23.92%	40.37%	19.83%	2.07%

4.5.3.1 Roofing material detection using VNIR bands

Figure 4.14(b) and **Figure 4.15**(b) show the results of roofing material detection using VNIR bands in Test Area-1 and Test Area-2, respectively. As shown in **Table 4-5** and **Table 4-7**, for Test Area-1, the OA, KC, and NRODR were 47.22%, 24.05%, and 29.41%, respectively; whereas, as shown in **Table 4-6** and **Table 4-7**, for Test Area-2 the OA, KC, and NRODR were 35.5%, 9.69%, and 4.20% respectively. Although most of the non-roofing objects were successfully suppressed, there were extremely high false detections. Because of the spectral similarities of different roofing materials in VNIR bands, one type

of roofs was detected as other types. For example, many of the fiberglass roofs were detected as metal.

4.5.3.2 Roofing material detection using original SWIR bands

Figure 4.14(c) and **Figure 4.15**(c) show the results of roofing material detection using original SWIR bands in the Test area-1 and Test area-2, respectively. As shown in **Table 4-5** and **Table 4-7,** for Test Area-1, the OA, KC, and NRODR were 76.84%, 57.73%, and 56.01%, respectively; whereas, as shown in **Table 4-6** and **Table 4-7**, for Test Area-2 the OA, KC, and NRODR were 37.80%, 8.32%, and 23.92% respectively. Because of the large pixel size (7.5m), a high level of spectral mixing is encountered. This led to several missed and false detections. Moreover, roofing materials of small buildings were not detected correctly because of the 7.5m pixel size.

4.5.3.3 Roofing material detection using HR SWIR bands

Figure 4.14(d) and **Figure 4.15**(d) the show results of roofing material detection using HR SWIR bands in the Test Area-1 and Test Area-2, respectively. As shown in **Table 4-5** and **Table 4-7**, for Test Area-1, the OA, KC, and NRODR were 78.94%, 63.27%, and 62.89%, respectively; whereas, as shown in **Table 4-6** and **Table 4-7**, for Test Area-2 the OA, KC, and NRODR were 76.04%, 57.29%, and 40.37% respectively. With smaller pixel size, 1.2m, the problem of large pixel size was solved, i.e. HR SWIR bands with 1.2m pixel size reduced spectral mixing significantly as well as roofing materials of smaller residential buildings can also be detected. However, some other non-roofing objects, such as roads and parking lots, which have similar spectrums to that of roofing materials, were falsely detected as roofs. Because of the high-resolution, more such objects became apparent

which led to more false detections. In summary, with HR SWIR bands, true detections were increased; however, false detections were increased as well.

4.5.3.4 Roofing material detection using super spectral bands

Figure 4.14(e) and **Figure 4.15**(e) show the results of roofing material detection using SWIR bands in the Test Area-1 and Test Area-2, respectively. As shown in **Table 4-5** and **Table 4-7**, for Test Area-1, the OA, KC, and NRODR were 83.33%, 70.78%, and 39.18%, respectively; whereas, as shown in **Table 4-6** and **Table 4-7**, for Test Area-2 the OA, KC, and NRODR were 80.56%, 67.21%, and 19.83% respectively. Super spectral bands solve the problem of spectral mixing and reduce the false detection. However, still there were few non-roofing objects such as roads parking lots, and bare earth whose spectrums in super spectral bands are similar to the concrete roof spectrum and therefore they were detected as concrete roofs.

4.5.3.5 Roofing material detection using the proposed method

Figure 4.14(f) and **Figure 4.15**(f) show the results of roofing material detection using SWIR bands in the Test Area-1 and Test Area-2, respectively. As shown in **Table 4-5** and **Table 4-7**, for Test Area-1, the OA, KC, and NRODR were 97.59%, 95.59%, and 16.16%, respectively; whereas, as shown in **Table 4-6** and **Table 4-7**, for Test Area-2 the OA, KC, and NRODR were 93.99%, 88.98%, and 2.07% respectively. The result demonstrated that the use of the proposed method not only reduced the spectral mixing to avoid miss-detections but also significantly reduced the false detections. The false detections were reduced because (1) the SNRO image helped in suppressing most of the non-roofing objects; (2) use of non-target spectrums further reduced the false detections.

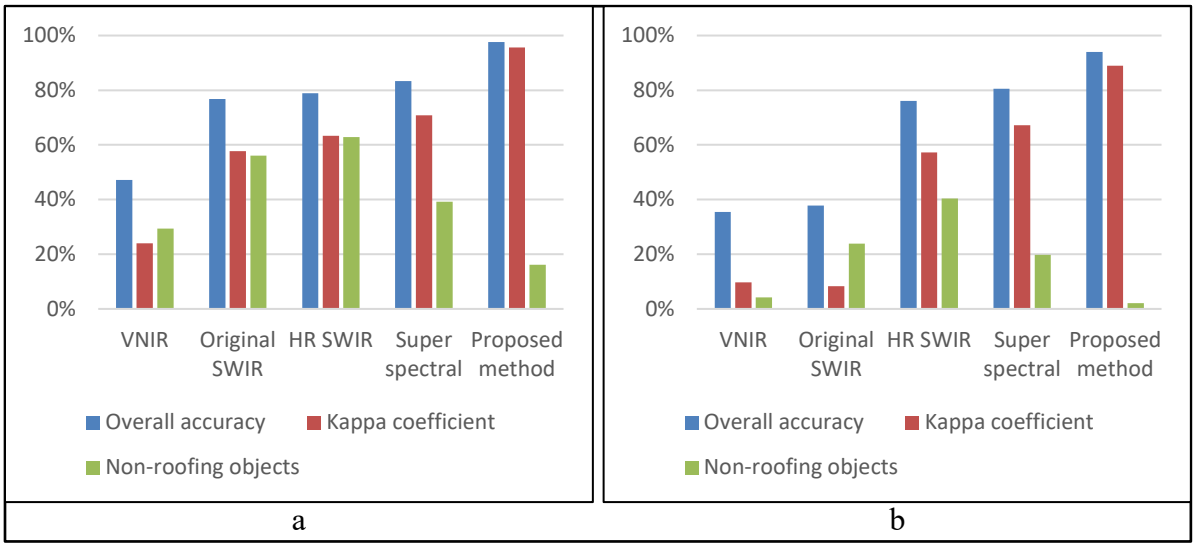

Figure 4.16 Comparison of overall accuracy and Kappa coefficients of roofing material detection in test area-1 (a) and test area-2 (b) using VNIR 1.2m, original 7.5m SWIR, HR 1.2m SWIR, 16 super spectral 1.2m bands and proposed method respectively.

The accuracies of the roofing material detection using the proposed method illustrated the capability of mapping roofing materials using affordable and easily accessible WorldView-3 satellite data.

4.6 Conclusions

The latest high-resolution satellite, WorldView-3, with 1 Pan band, 8 VNIR bands and 8 SWIR bands, significantly increases the potential for detecting different roofing materials in urban environments. However, our experiments found that using only VNIR bands is not sufficient for roofing material detection. Although the available SWIR bands of WorldView-3 can provide additional information for roofing material detection, it is

difficult to detect roofing materials of small size residential buildings due to its low-resolution (7.5m). It is also difficult to differentiate roofs from some non-roof objects such as roads and parking lots, because the spectral information in the original SWIR bands is not sufficient for separating them from each other. In addition, although the detection of roofing materials of small size buildings can be made possible by utilizing the FGSS algorithm to increase the resolution of available SWIR bands from 7.5m to 1.2m, the resolution increase also increases the false detection rate due to its inability to separate roofs from some non-roof objects.

Therefore, this research introduced a novel method to detect roofing materials using WorldView-3 satellite imagery. The proposed method (1) suppresses non-roofing objects by applying the spectral angle mapper (SAM) algorithm on VNIR bands; (2) combines the original 1.2m VNIR bands and the 1.2m HR SWIR bands generated by the FGSS algorithm to form a high-resolution, super spectral image; (3) detects roofing materials by applying the modified SAM algorithm on super spectral bands. The proposed method was tested on both commercial (large size buildings) and residential (small size buildings) areas. The accuracy analysis results show that the proposed method achieved overall accuracy and Kappa coefficient of 97.59% and 95.59% respectively for the commercial area; whereas, for the residential area, overall accuracy and Kappa coefficient of 93.99%, and 88. 98% respectively was achieved. Therefore, the proposed method can be used to detect roofing materials using affordable and easily accessible WorldView-3 satellite data.

The proposed method has achieved a high level of accuracy; however, there are still a few false detections. For example, a very few pixels of roads and parking lots (made with concrete) are detected as concrete. This problem could be eliminated, if elevation data

could be incorporated in the roofing material detection process. Elevation data will be conducted in future research. Furthermore, the proposed method was tested to detect four types of roofing materials. However, in order to detect other types of roofing materials, the proposed method requires spectral signatures of those roofing materials.

4.7 Acknowledgement

The Canada Research Chairs Program funded this research. The original WorldView-3 Pan, VNIR and SWIR images were provided by DigitalGlobe Inc.

4.8 References

Cilia, C., Panigada, C., Rossini, M., Candiani, G., Pepe, M., & Colombo, R. (2015). Mapping of asbestos cement roofs and their weathering status using hyperspectral aerial images. *ISPRS Journal of Photogrammetry and Remote Sensing*, 4(2), 928–941.

Congalton, R. G., Green, K. (2009). Assessing the Accuracy of Remotely Sensed Data. *Principles and Practices*.2nd edition. Boca Raton, FL: CRC Press.

DigitalGlobe, Inc. Exploring the benefits of SWIR satellite imagery, white paper. Accessed 22 February17: http://global.digitalglobe.com/sites/default/files/DG_SWIR_WP.pdf

ENVI. (2016). ENVI ver. 5.3 software help document. Boulder, CO: Exelis Visual Information Solutions. Inc., a subsidiary of Harris Corporation.

Fiumi, L., Campopiano, A., Casciardi, S., & Ramires, D. (2012). Method validation for the identification of asbestos-cement roofing. *Applied Geomatics,* 4(1), 55–64.

Fuze Go. (2016). FuzeGo ver. 3.0 software help document. Fredericton, NB: Scene Sharp Technologies Inc.

Hamedianfar A., Shafri H., Mansor, S., Ahmad, N. (2014). Combining data mining algorithm and object-based image analysis for detailed urban mapping of hyperspectral images. *Journal of Applied Remote Sensing*, 8(1), 085091.

Hamedianfar, A., & Shafri, H. Z. M. (2014). Development of fuzzy rule-based parameters for urban object-oriented classification using very high resolution imagery. *Geocarto International.* 29(3), 268–292.

Hamedianfar, A., & Shafri, H. Z. M. (2015). Detailed intra-urban mapping through transferable OBIA rule sets using WorldView-2 very-high-resolution satellite images." *International Journal of Remote Sensing*, 36(13), 3380–3396.

Hamedianfar, A., & Shafri, H. Z. M. (2016). Integrated approach using data mining-based decision tree and object-based image analysis for high-resolution urban mapping of WorldView- 2 satellite sensor data. *Journal of Applied Remote Sensing,* 10(2), 025001.

Herold, M., Roberts, D. A., Gardner, M. E., & Dennison., P. E. (2004). Spectrometry for urban area remote sensing—Development and analysis of a spectral library from 350 to 2400 nm. *Remote Sensing of Environment*, 91(3–4): 304-319.

Jeffreys, H. (1946). An Invariant for the Prior Probability in Estimation Problems. *Proceedings of the Royal Society of London,* A., Vol. 186, pp. 454-461, 1946.

Kruse, F. A., Baugh, W.M., & Perry, S. L. (2015). Validation of DigitalGlobe WorldView-3 Earth imaging satellite shortwave infrared bands for mineral mapping. *Journal of Applied Remote Sensing*, 9(1), 096044.

Kruse, F.A., Lefkoff, A.B., Boardman, J.W., Heidebrecht, K.B., Shapiro, A.T., Barloon, P.J., & Goetz, A.F.H. (1993). Airbone Imaging Spectrometry The spectral image processing system (SIPS)—interactive visualization and analysis of imaging spectrometer data. *Remote Sensing of Environment*, 44 (2), 145-163.

Richards, J.A. (1999). Remote Sensing Digital Image Analysis. *Springer-Verlag*, Berlin, p. 240.

Samsudin, S. H., Shafri, H. Z. M., & Hamedianfar, A. (2016). Development of spectral indices for roofing material condition status detection using field spectroscopy and WorldView-3 data. *Journal of Applied Remote Sensing,* 10(2), 025021.

Taherzadeh, E., & Shafri, H. Z. M. (2013). Development of a generic model for the detection of roof materials based on an object-based approach using WorldView-2 satellite imagery. *Advanced Remote Sensing*, 2(4), 312–321.

Young, D. (2015). Use cases for SWIR imagery – taking a closer look – part 1 and 2," *DigitalGlobe Inc. Longmont, CO, white paper.*

Zhang, Y. (2004). Understanding image fusion. *Photogrammetric Engineering & Remote Sensing*, 70 (6), 657–661.

Zhang, Y., & Mishra, R.K. (2012). A review and comparison of commercially available pan-sharpening techniques for high resolution satellite image fusion. *Proceedings of IEEE IGARASS 2012*, Munich, Germany, July 22-27, pp.182-185.

Zhang, Y., & Mishra, R.K. (2014). From UNB PanSharp to Fuze Go – the success behind the pan-sharpening algorithm. *International Journal of Image and Data Fusion*, 5 (1), 39–53.

Zhang, Y., Roshan, A., Jabari, S., Khiabani S.A., Fathollahi, F., & Mishra, R.K. (2016). Understanding the quality of pansharpening-A Lab Study. *Photogrammetric Engineering & Remote Sensing*, 82 (10), 748–755.

Chapter 5 : SUMMARY AND CONCLUSIONS

This chapter summarizes the research conducted for this dissertation. The outlines of the research from chapter 2 to 4 as well as the contributions of this research are presented in this section. At the end, some suggestions for future work are provided.

5.1 Summary of research

In this dissertation, the great potential of WorldView-3 satellite imagery is exploited for detecting solar PV panels and roofing materials in an urban environment. Chapter 2 focuses on finding a solution to increase resolution of commercially available WorldView-3 SWIR bands.Chapter 3 and Chapter 4 focus on developing new methods to detect solar PV panels and roofing materials, respectively. A summary of research works performed from Chapter 2 to Chapter 4 are discussed as follows.

5.1.1 Chapter 2

This chapter investigated the capacities of nine industry-adopted pan-sharpening algorithms for increasing the resolution of WV-3 SWIR bands from 7.5m to 1.2m. The general principles of the pan-sharpening algorithms are reviewed. The WV-3 panchromatic (Pan) images are down-sampled from 0.3m to 1.2m to fuse the 7.5m SWIR image. Experiments demonstrated that most commonly used algorithms are not suitable for pan-sharpening SWIR images, whereas the new FGSS algorithm can produce satisfactory results.

5.1.2 Chapter 3

This research introduced a novel HR-SSF-SAM method to detect solar PV panels using WorldView-3 satellite imagery. The method combines the original 1.2m VNIR bands and the 1.2m HR SWIR bands generated by the FGSS algorithm to form a high-resolution, super spectral image; and then utilizes the spectral similarity detection capacity of the SAM algorithm to identify solar PV panels in the high-resolution, super spectral bands.

5.1.3 Chapter 4

This chapter introduced a novel method to detect roofing materials using WorldView-3 satellite imagery. The proposed method (1) suppresses non-roofing objects by applying the spectral angle mapper (SAM) algorithm on VNIR bands; (2) combines the original 1.2m VNIR bands and the 1.2m HR SWIR bands generated by the FGSS algorithm to form a high-resolution, super spectral image; (3) detects roofing materials by applying the modified SAM algorithm on super spectral bands. The proposed method was tested on both commercial (large size buildings) and residential (small size buildings) areas.

5.2 Achievements of the research

Based on the three main chapters of this dissertation, the summary of overall contributions is presented as follows.

5.2.1 WorldView-3 SWIR bands pan-sharpening

The experiments conducted for this research proved that the FGSS pan-sharpening algorithm is capable of producing high quality pan-sharpened SWIR bands without losing their spectral information; whereas other fusion techniques produced poor results, with

obvious spectral distortion, poor spatial quality, and/or colour artifacts. The outcome of this research provides remote sensing researchers and practitioners with an effective tool to utilize WorldView-3 SWIR imagery for advanced applications. Furthermore, as the resolution of SWIR bands can be increased equal to that of VNIR bands, the combination of VNIR and SWIR bands can offer additional information for remote sensing analytics such as material identification, mineral/geology mapping, agriculture, forestry, and wildfire response.

5.2.2 Solar PV panel detection

A novel method is developed to detect solar PV panels using WorldView-3 satellite imagery. The outcome of this research provides an efficient and cost-effective solution to detect solar PV panels as compared to the traditional manual surveys which are expensive, time consuming, and laborious and often yield insufficient information. Therefore, using the proposed method, information about solar PV panel installations can easily be available to energy and environment policy makers in order to make informed decisions. Furthermore, using the proposed method, even solar PV panels and glass roofs can be differentiated from each other, which is difficult for the human eye to achieve.

5.2.3 Roofing material detection

A novel method is developed to detect fiberglass, ethylene propylene diene monomer (EPDM), metal, and concrete roofing materials using WorldView-3 satellite imagery. The outcome of this research provides an efficient and cost-effective solution to detect roofing materials as compared to the conventional on-site surveys which are expensive, time

consuming, and slower in coping with new construction. The proposed method can provide timely and cost-effective information about the roofing materials to city decision makers.

5.3 Suggestions for future work

The proposed method to detect roofing materials has achieved a high level of accuracy; however, there are still a few false detections. For example, a few pixels of roads and parking lots (made with concrete) are detected as concrete. The elevation data can be used to differentiate between roofs and other ground objects such as parking lots and roads. Therefore, the false detections could be eliminated, if elevation data could be incorporated in the roofing material detection process.

The proposed 16 bands super spectral imagery (VNIR+SWIR) with 1.2m resolution can be useful for material identification, agriculture applications, forestry applications, smoke penetration, and mineral/geology mapping. In this research, the focus was on material identification (solar PV panels and roofing materials); however, new methods can be developed for agricultural, forestry, and mineral/geology applications.

5.3.1 Agriculture

Crop stresses replace the green chlorophyll content of the leaves with carotenoids which can be detected in VNIR EMS. In addition, SWIR EMS can be used to detect crop moisture, soil types, and crop residue. Therefore, the proposed 1.2m super spectral imagery can be used to develop solutions for precision agriculture practices.

5.3.2 Forestry

Different tree species have unique spectral signatures in VNIR and SWIR EMS. In addition, tree stress, pest infestation, and forest moisture exhibit unique characteristics in VNIR and SWIR EMS. Therefore, the proposed 1.2m super spectral image can be utilized for forestry applications.

5.3.3 Mining/Geology

Different minerals absorb specific wavelengths and reflect others in the VNIR and SWIR EMS. Therefore, the proposed 1.2m super spectral image can used for precise mineral exploration applications.

Appendix I From UNB PanSharp to Fuze Go – the success behind the pansharpening algorithm

Zhang, Y., & **Mishra, R. K.** (2014). From UNB PanSharp to FuzeGo — the success behind the pan-sharpening algorithm, International Journal of Image and Data Fusion, Vol. 5, No.1, pp. 39-53

Abstract

The pan-sharpening algorithm, known as UNB PanSharp, was adopted by PCI Geomatics in 2002 and by DigitalGlobe (DG) in 2003, resulting in PCI PanSharp and DG PanSharp. Now, UNB PanSharp is developed as a stand-alone software tool, named Fuze Go™, that can be used stand-alone, integrated into ENVI and potentially into other major geo-spatial software packages such as EDARS, ESRI, and SOCET. In addition, it is in the process to integrate Fuze Go into GeoMarketSpace – a new online system that turns all geospatial information into answers. What has made UNB PanSharp successful for the last 10 years and still standing out from millions of research publications in the area? This article will go through the general principles of individual pan-sharpening algorithms that have been adopted by industry and widely used by users globally to find out the differences between UNB PanSharp and the other pan-sharpening algorithms.

Keywords: image fusion; pan-sharpening; algorithms; fusion quality; differences

1 Introduction

More than 70% of optical earth observation satellites and many modern aerial digital cameras simultaneously collect low-resolution multispectral (MS) and high-resolution panchromatic (Pan) images (Zhang, 2010). Many new satellites to be launched in the next

years are also equipped with both MS and Pan sensors. In addition, the number of spectral bands of the MS sensors is increasing, from traditional 4 spectral bands to 8 or more bands, such as WorldView-2 with 8 MS bands and WorldView-3 with 16 MS bands (8 in VNIR and 8 in SWIR).

Therefore, it becomes increasingly important to find a fully automated pan-sharpening algorithm that can constantly produce high quality, high-resolution MS images by fusing the low-resolution MS images and high-resolution Pan images from the same satellite. It is also important that the pan-sharpening quality is independent of sensor, season, and region differences, because (1) different sensor systems may have different spectral bandwidths and different numbers of bands, (2) images collected in different seasons contain different spectral information, and (3) ground surfaces in different regions reflect the sun's radiation differently. All these differences may lead to different pan-sharpening results.

In the late 1980s, research on pan-sharpening was started to fuse the high-resolution Pan (10 m) with low-resolution MS (20 m) images from SPOT-1 (launched in 1986) or fuse the SPOT Pan (10 m) and the Landsat MS (30 m) images. After the launch of IKONOS satellite in 1999, research on image fusion or pan-sharpening has quickly increased. To date, more than 2.2 million publications (including patents) have been published on the topic of image fusion, and more than 47,000 publications have been published on topic of pan-sharpening, according to a Google Scholar search on 17 December 2012.

Until now, only a dozen of most successful pan-sharpening algorithms have been adopted by remote sensing industry. The algorithms adopted by the major commercial software packages such as ERDAS, ENVI, PCI, and ESRI include HPF (ERDAS), IHS

(ERDAS, PCI, and ESRI), PCA (ERDAS, ENVI), Brovey (ERDAS, ENVI, ESRI), Wavelet (ERDAS), Gram Schmidt (ENVI, ESRI), and UNB PanSharp (PCI, Fuze Go). However, discrepant pan-sharpening results have been obtained by users using different software tools or using the same tool but different images. For example:

- Du et al. (2007) compared PCA, Brovey, Multiplicative, Adjusted Multiplicative, Gram Schmidt, and UNB PanSharp for the fusion of one IKONOS Pan and MS image and one QuickBird Pan and MS image. They concluded that Gram Schmidt and UNB PanSharp generated best results when measured using both quality indexes and application algorithms.
- Nikolakopoulos (2008) evaluated nine pan-sharpening algorithms for fusing one QuickBird Pan and MS image scene, namely IHS, Modified IHS, PCA, UNB Pansharp, Wavelet, LMM (Local Mean Matching), LMVM (Local Mean and Variance Matching), Brovey, and Multiplicative algorithm. Based on the quantitative and qualitative measurements – correlation coefficient, histogram statistics, unsupervised classification, and visual analysis – the author concluded that LMVM, UNB Pansharp, and LMM algorithms produced better pan-sharpening results than all other algorithms.
- Padwick et al. (2010) compared IHS, PCA, Gram Schmidt, and HCS (Hyperspherical Color Sharpening) algorithms for fusing WorldView-2 Pan and MS images and confirmed that Gram Schmidt, PCA, and IHS do not produce acceptable pan-sharpened natural colour MS images.
- In a recent study by Zhang and Mishra (2012), 11 different pan-sharpening algorithms adopted by major commercial software packages were used to fuse large

coverage Pan and MS images from IKONOS, QuickBird, GeoEye-1, and WorldView-2. The pan-sharpening results were analysed and evaluated by independent remote sensing professionals. The conclusions reached by all the evaluators were that UNB PanSharp produced the best fusion quality for all types of sensors, images, and spectral bands; Gram Schmidt produced high quality for most images, but poor results for some other images, especially WorldView-2 images; and other algorithms worked well with some images or sensors, but not with others.

What are the reasons that UNB PanSharp produces consistent, good fusion results despite the differences in sensors, seasons, regions, and number of bands, although other pansharpening algorithms produce good fusion results for some sensors, images, or MS bands, but not for others? To answer these questions, we need to understand the general principles of individual pan-sharpening algorithms first, which will be described in Section 2.

2 Pan-sharpening algorithms

The general principles of the nine popular pan-sharpening algorithms used by ERDAS, ENVI, PCI, and ESRI are described below. They were developed based on certain assumptions and need to be operated under certain conditions. They have also associated advantages and limitations. In all the pan-sharpening processes, the low-resolution MS bands need to be up-sampled to the same pixel size of the Pan image before pansharpening process.

2.1 High pass filter

This algorithm is used by ERDAS named HPF Resolution Merge (Gangkofner et al., 2008, ERDAS, 2010). The general principle is to extract high frequency information from the high-resolution Pan image using a high pass filter (HPF). The high frequency information is then added into each band of the up-sampled low-resolution MS image with a specified weight. The weight is relative to the global standard deviation of individual MS image bands.

In the implementation of the HPF algorithm, first the ratio (*R*) of low-resolution MS image pixel size to high-resolution Pan image pixel size is computed. A high pass convolution kernel (HPK) is created to filter the Pan image to generate a HPF image. The size of HPK is dependent on "R". In the next step, the MS image is up-sampled to the pixel size of the high-resolution Pan image. The pan-sharped MS image is computed using Equations (1) and (2). Finally, the mean and standard deviation of pan-sharpened MS image bands are matched with those of the original MS image bands.

$$PSI_{ij} = MSI_{ij} + HPFI_{ij} \times W \quad (1)$$

$$W = \frac{\sigma_{MSI}}{\sigma_{HPFI} \times M} \quad (2)$$

where *PSI* is the Pan-sharped high-resolution MS image; *MSI* is the up-sampled MS image; *HFPI* is the HPF image; *W* is the weighting factor of the HPF image corresponding to

individual MS bands; σ_{MSI} is the standard deviation of the MS band; *M* is the user-adjustable modulating factor to determine the crispness of the output image which depends on *R*.

To achieve a good pan-sharpening result, the size of the HPF filter (HPK) and the weights for each MS band need to be adjusted. The suggested sizes of HPK, suggested weights for individual MS bands, and suggested values of *M* are provided by the user manual.

2.2 IHS

It is used by ERDAS, PCI, and ESRI but with different variations. It utilises the IHS (intensity, hue, saturation) transformation to convert three MS bands from RGB (red, green, blue) into IHS space and then replaces the intensity (*I*) band by the Pan, followed by an inverse IHS transformation.

Several IHS transformation models have been discussed in the literature. One common IHS transformation is based on a cylindrical colour model. The equations used in the cylindrical colour model IHS transformation are given as follows:

$$\begin{bmatrix} I \\ v_1 \\ v_2 \end{bmatrix} = \begin{bmatrix} \frac{1}{\sqrt{3}} & \frac{1}{\sqrt{3}} & \frac{1}{\sqrt{3}} \\ \frac{-1}{\sqrt{6}} & \frac{-1}{\sqrt{6}} & \frac{2}{\sqrt{6}} \\ \frac{-1}{\sqrt{2}} & \frac{1}{\sqrt{2}} & 0 \end{bmatrix} \tag{3}$$

$$H = \tan^{-1}\frac{v_2}{v_1} \tag{4}$$

$$S = \sqrt{v_1^2 + v_2^2} \quad (5)$$

where: v_1 and v_2 are two intermediate values.

However, it can only fuse three MS bands each time. In addition, the fusion quality strongly depends on the degree of spectral overlap between the MS bands and the Pan to be fused.

- To fuse four or more MS bands, ERDAS adopted a modified IHS algorithm named Modified IHS Resolution Merge (Siddiqui, 2003; ERDAS, 2010). It repeats the IHS fusion process twice, each time for three different MS bands. In the end, 4 out of 6 pan-sharpened MS bands are selected as final fusion output. This technique works by assessing the spectral overlap between each MS band and the high-resolution Pan band. The weights are calculated based on the relative wavelengths of the overlapping MS bands.
- To reduce colour distortion, ESRI (ESRI, 2013) suggested altering the Pan image by subtracting certain weighted intensity (*I*) value from the Pan and then replace the intensity (*I*) with the altered Pan. But the weight is not given in the manual. The default weights, 0.33, are set in the software for R, G, and B bands.

2.3 PCA

It is named Resolution Merge (Principal Components) in ERDAS (Chavez et al., 1991; ERDAS 2010) and PC Spectral Sharpening in ENVI (ENVI, 2012). This method uses the principal component (PC) transformation to convert MS bands into PCs according to the eigenvectors of their corresponding covariance matrices. The first principal component (PC-1) is then replaced by the high-resolution Pan image. The pan-sharped MS image is

obtained by applying an inverse PC transformation on the new set of components after PC-1 is replaced by Pan.

To perform a PC transformation, the covariance matrix of the MS bands needs to be computed and then the eigenvalues and eigenvectors of the covariance matrix are determined. The eigenvectors are used to form an eigenvector matrix. The eigenvector matrix is then used to transform the MS bands into PCs using equation (6).

$$\boldsymbol{y} = G\boldsymbol{x} \tag{6}$$

where $\boldsymbol{y}$ is the vector of principal components; $\boldsymbol{x}$ is the vector of original MS image bands; and G is the eigenvector matrix To fuse the Pan image into the MS bands, the Pan image is used to replace the first principal component (PC-1). An inverse PC transformation is then applied to the PCs where the PC-1 is replaced by Pan to produce pan-sharpened MS bands, based on equation (7).

$$\boldsymbol{z} = G^{-1}\boldsymbol{y}' \tag{7}$$

where $\boldsymbol{z}$ is the vector of pan-sharpened MS bands; $\boldsymbol{y'}$ is the vector of the PCs where the PC-1 is replaced by Pan; and G^{-1} is the inverse matrix of G. _To reduce colour distortion, the histogram of the Pan needs to be matched to that of the PC-1 before the inverse principal component transformation. It assumes that the spectral range of the low-resolution MS bands overlap with that of the high-resolution Pan image. Therefore, the fusion quality strongly depends on the degree of spectral overlap between the MS bands and the Pan to be fused. In addition, PC transformation is a computationally intensive process and requires more time to process compared to other pan-sharping methods.

2.4 Brovey

It is used by ERDAS, ENVI, and ESRI with some modifications. The Brovey transformation uses three MS bands and one Pan band to produce three pan-sharpened MS bands. Each pan-sharpened MS band is generated by multiplying the corresponding MS band with the Pan band and then divided by the sum of the three MS bands to be fused. As it is computationally simple, the processing speed is fast.

General equations used to compute the Brovey transformation is given as follows:

$$Red_{out} = \frac{Red_{in}}{Blue_{in} + Green_{in} + Red_{in}} \times Pan \quad (8)$$

$$Green_{out} = \frac{Green_{in}}{Blue_{in} + Green_{in} + Red_{in}} \times Pan \quad (9)$$

$$Blue_{out} = \frac{Blue_{in}}{Blue_{in} + Green_{in} + Red_{in}} \times Pan \quad (10)$$

where Red_{out}, $Green_{out}$, and $Blue_{out}$ are the pan-sharped high-resolution MS bands in RGB; Red_{in}, $Green_{in}$, and $Blue_{in}$ are the low-resolution MS bands in RGB.

However, only three MS bands can be pan-sharpened. In addition, it assumes that the sum of spectral bandwidths of three MS bands overlaps with those of the Pan image. Otherwise, significant colour distortions will be produced. Therefore:

- In ERDAS (ERDAS, 2010), only three MS bands, such as bands 3, 2, 1 from a SPOT or Landsat TM image or 4, 3, 2 from a Landsat TM, are suggested.

- In ENVI, an extension of the Brovey algorithm named Color Normalization is used (Klonus and Ehlers, 2009; ENVI, 2012). The MS bands are grouped into a spectral segment defined by the MS bands falling in the spectral range of the Pan image. The corresponding band segments are processed together in the manner that each MS band is multiplied by the high-resolution Pan band and then divided by the sum of the MS bands in the segment (Vrabel et al., 2002). Only the MS bands that fall within the spectral range of the Pan image can be pan-sharpened, whereas all other MS bands are unchanged in the output.
- In ESRI (ESRI, 2013), it is suggested to use weighted sum of the three MS bands instead of a simple sum of the MS bands. It is also suggested to use near-infrared band if it is available. However, it did not suggest how to find the weights (ESRI, 2013). But, by default, 0.33 is used as the weights for R, G, and B.

2.5 Subtractive fusion

Used by ERDAS (ERDAS, 2010; Ashraf et al., 2012), named Subtractive Resolution Merge, the algorithm produces a low-resolution synthetic Pan image from the weighted sum of the low-resolution MS bands. This synthetic Pan is then up-sampled to the same pixel size of high-resolution Pan and then subtracted from the high-resolution Pan to extract edge details. It also uses a mix of HPF and LPF (low pass filter) to control spatial details. The kernel size of the HPF and LPF is fixed at 3 × 3 and 5 × 5, respectively, and the central weight of the HPF is defined by users.

The synthetic Pan image is computed using following equation:

$$Pan_{Syn} = \frac{(WBS - \mu_{WBS})}{\sigma_{WBS}} \times \sigma_{Pan} + \mu_{Pan} \quad (11)$$

where Pan_{Syn} is the synthetic Pan image; *WBS* is a weighted sum of MS bands; μ_{WBS} is the mean of *WBS;* μ_{Pan} is mean of Pan; σ_{WBS} is the standard deviation of *WBS*; and σ_{Pan} is the mean of Pan.

Once, synthetic Pan image is computed, the pan-sharpened image is computed using following equation:

$$PSI = (LPF * MS) + (HPF * Pan - LPF * Pan_{Syn}) \times PCW \times NF \quad (12)$$

where *PSI* is the pan-sharpened image; *LPF* is the low pass filter; *HPF* is the high pass filter; *PCW* is the Pan contribution weights (ranging from 0.7 to 1.3); *NF* is a normalization function.

A range of weights for producing the low-resolution synthetic Pan are suggested by the software manual so that the user needs to choose proper weights to achieve a balance between spectral fidelity and spatial contrast. In addition, the user also needs to select the central weight (value) of the HPF from a number of suggested values.

2.6 Wavelet

The algorithm is adopted by ERDAS, named Wavelet Resolution Merge (ERDAS, 2010). It is a modification of the work by King and Wang (2001) with extensive input from Lemeshewsky (1999, 2002). It utilises a wavelet transformation to decompose the high-resolution Pan image into one low frequency approximation image and three high frequency feature images. The low frequency approximation image is then replaced by the low-resolution MS bands, respectively and then followed by individual inverse wavelet transformations each for one MS band.

In the implementation of the wavelet-based pan-sharpening, first the DWT (Discrete Wavelet Transform) operation is applied to the high-resolution Pan image, which

transforms Pan image into a set of sub-images comprising one low frequency approximation image and three high frequency images. Equation (13) is used to transform Pan image into the set of four frequency images.

$$WTI = DWT(Pan) \tag{13}$$

where *WTI* is the wavelet transformed image; DWT is the discrete wavelet transform operation; and *Pan* is high-resolution panchromatic image.

Once the set of wavelet transformed images are computed, the low frequency approximation image of the Pan image is replaced by one of the MS bands. This results in a new set of four wavelet transformed images (WTI′) comprising one MS image band and three high frequency images. Finally, individual bands of high-resolution pan-sharpened image is computed using the IDWT (Inverse Discrete Wavelet Transform) operation. Equation (14) is used to transform WTI′ into high-resolution pan-sharpened image.

$$PSI_i = IDWT(WTI_i') \tag{14}$$

where *PSI* is the high-resolution pan-sharpened image; IDWT is the Inverse Discrete Wavelet Transform operation; and *WTI'* is the set of wavelet transformed sub-images after its low frequency approximation image is replaced by a MS band. This inverse wavelet transform is operated repeatedly, each for producing one pan-sharpened MS bands.

However, the algorithm can only down-sample the high-resolution Pan image by a factor of two in each iteration, reducing the resolution of the approximation image by a factor of two. This is suitable to fuse images with a Pan/MS resolution ratio of 1/2 or 1/4, such as Landsat ETM+ Pan and MS and IKONOS Pan and MS. But it has problems to fuse

SPOT Pan (10 m) with Landsat MS (30 m). In addition, obvious artefacts in the fused images are an unavoidable problem of wavelet-based pan-sharpening techniques.

2.7 ESRI pan-sharpening

This is an ESRI pan-sharpening algorithm (ESRI, 2013). It first generates a weighted average image using the MS bands (near-infrared band is an optional). An adjustment image (ADI) is then created by subtracting the grey values of the weighted average image from those of the original Pan image. Finally, the adjustment image (ADJ) is added to each individual MS bands, respectively, to produce individual pan-sharpened MS bands.

ESRI Pan-sharpening uses the following equations to compute a pan-sharpened image:

$$ADJ = Pan - W \tag{15}$$

$$Red_{out} = Red_{in} + ADJ \tag{16}$$

$$Green_{out} = Green_{in} + ADJ \tag{17}$$

$$Blue_{out} = Blue_{in} + ADJ \tag{18}$$

$$NIR_{out} = NIR_{in} + ADJ \tag{19}$$

where ADJ is the adjusted image; W is a weighted average image of the MS bands; Pan is the high-resolution panchromatic image; Red_{out}, $Green_{out}$, $Blue_{out}$, and NIR_{out} are the R, G, B and NIR Pan-sharped high-resolution MS bands; Red_{in}, $Green_{in}$, $Blue_{in}$, and NIR_{in} are the R, G, B and NIR low-resolution MS bands. Several sets of predefined weights for generating the weighted average image are provided by the software package based on the tests with existing images. Each set for one satellite, such as: GeoEye-1: 0.6,

0.85, 0.75, 0.3; IKONOS: 0.85, 0.65, 0.35, 0.9; QuickBird: 0.85, 0.7, 0.35, 1.0; WorldView-2: 0.95, 0.7, 0.5, 1.0.

However, when the spectral characteristics of Pan and MS images are different than those of the tested images, poor fusion results will occur. In addition, only four MS bans can be pan-sharpened.

2.8 Gram Schmidt

It is named Gram Schmidt Spectral Sharpen in ENVI (ENVI, 2012) and Gram Schmidt in the latest ESRI ArcGIS version 10.1 (ESRI, 2013). The original Gram Schmidt fusion (Laben and Brower, 1998) generates a simulated lower resolution Pan image through weighted sum of blue, green, red, and near-infrared MS bands. The weights for the four MS bands are calculated based on the sensor's optical transmittance and spectral response for the four MS bands and the Pan band. A Gram Schmidt transformation is then applied to the simulated low-resolution Pan and the low-resolution MS bands, with the simulated Pan as the first band. The high-resolution Pan image is adjusted to match the first band of Gram Schmidt transformed bands. Then the adjusted high-resolution Pan is used to replace the first band of the Gram Schmidt transformed bands, followed by an inverse Gram Schmidt transformation to produce pan-sharpened MS bands.

The equation for computing the simulated low-resolution Pan image is

$$Pan_{Syn} = (B \times B_w) + (G \times G_w) + (R \times R_w) + (NIR \times NIR_w) \qquad (20)$$

where Pan_{Syn} is the simulated low-resolution Pan image; *B, G, R,* and *NIR* are the MS bands; and B_w, G_w, R_w, and NIR_w are the weights for the B, G, R, and NIR bands, respectively.

Because the simulated low-resolution Pan image from equation (20) is inserted into original MS image as a first band (GS1) for the Gram-Schmidt transformation, if the MS image has *N* bands, after inserting simulated Pan image, the new MS image will have *N*+1 bands. Below is the equation for the Gram-Schmidt Transformation:

$$GS_T(i,j) = (B_T(i,j) - \mu_T) - \sum_{I-1}^{T-1} \varphi(B_T, GS_I) \times GS_I(i,j) \quad (21)$$

where *T* is the band number being transformed; *B* is the original band; μ_T is the mean of band *T* (B_T); $\varphi(B_T, GS_I)$ is the covariance between B_T and GS_I, and GS_I is the simulated low-resolution Pan image.

In equation (21), μ_T is given by:

$$\mu_T = \frac{\sum_{j=1}^{C}\sum_{i=1}^{R} B_T(i,j)}{C \times R} \quad (22)$$

where *C* is the total number of columns in the image; and *R* is the total number of rows in the image.

The covariance $\varphi(B_T, GS_I)$ is given by:

$$\varphi(B_T, GS_I) = \frac{\sigma(B_T, GS_I)}{\sigma(GS_I, GS_I)^2} \quad (23)$$

where $\sigma(GS_I, GS_I)^2$ is the variance of GS_I. Because the sensor's optical transmittance and spectral response are not readily available for most cases, ENVI and ESRI introduced different remedy solutions:

- ENVI uses three different methods to simulate low-resolution Pan image
    - Average the MS bands.

- Simulate a Pan image for the selected sensors such as IKONOS, IRS1, Landsat7, QuickBird, SPOT 5, KOMPSAT-2, RapidEye, and GeoEye-1, and WorldView-2.
- Simulate a Pan image for the selected filter function. This option requires radimetrically corrected data.

- In ESRI, one or two sets of weights are suggested for each satellite. In each set, one weight is specified to one of the four MS bands. Therefore, ESRI Gram Schmidt is unable to pan-sharpen more than four MS bands each time. In addition, it produces very poor results for the MS bands other than blue, green, red, and near-infrared.

On the other hand, even though the optical transmittance and spectral response of each satellite sensor were available to the users, the pan-sharpening quality of Gram Schmidt would vary as well, because seasonal, regional, and atmospheric differences also alter the spectral characteristics of the MS and Pan images. These differences are not taken into account by the Gram Schmidt fusion algorithm. In addition, the Gram Schmidt transformations (forward and reverse) are computationally intensive and hence it takes more time in generating pan-sharpened images.

2.9 UNB PanSharp (Fuze Go™)

Used by PCI, DigitalGlobe and Scene Sharp, named PCI PanSharp, DG PanSharp, and Fuze Go, respectively, the algorithm (Zhang 2004) utilises the least squares technique to find the best fit between the grey values of the Pan band and the MS bands to adjust the contribution of individual bands to the fusion result. It employs a set of statistic approaches to estimate the grey value relationship between all the input bands to eliminate the problem of data set dependency (i.e. reduce the influence of data set variation in the fusion). It is a

fully automated one-step process, producing high quality fusion results regardless of sensor and image variations and number of MS bands.

It has two pan-sharpening modes. The standard mode produces a pan-sharpened MS image with exactly the same spatial detail as that of the original Pan, whereas the enhanced mode produces a pan-sharpened MS image with slightly sharper spatial detail than the original Pan for a better visual effect.

Because it uses the method of least squares to find the best fit between the MS and Pan bands first and then fuse them together. Consistent good fusion results are achieved regardless the variations in sensors, seasons, regions, number of MS bands, and combinations of MS bands. No user-specified parameters or matching between Pan and MS bands is needed.

However, if the MS and Pan images are taken at different times or from different satellites, colour distortion may occur due to seasonal difference and/or miss-registration between the two images. Practically, it may not be viable to fuse Pan and MS images from two high-resolution satellites, because most of the images are off-nadir, and precise coregistration of high-resolution images from different viewing angles is still an unsolved technical problem.

3 Pan-sharpening results

Large coverage Pan and MS images from IKONOS, QuickBird, GeoEye-1, and WorldView-2 were fused using the nine algorithms mentioned above. The images were taken in different years and months and from different regions (San Diego, USA; Beijing, China; Hobart, Australia; and Moncton, Canada). In the pan-sharpening process, the best processing procedure suggested by the user manual of each pan-sharpening technique was

used. It was attempted to pan-sharpen all the MS bands with the corresponding Pan image at once. But some algorithms just allow for the pan-sharpening three MS bands each time. Therefore, two times of fusions were needed to get four pan-sharpened MS bands. The ESRI Gram Schmidt just allows for the fusion of four MS bands each time. At least two times of fusions are needed to pan-sharpen the 8 MS bands of WorldView-2 images.

Figure 1 Subset of WorldView-2 Pan image used for pan-sharpening.

More than 36 pan-sharpened images were produced using the nine different algorithms. Because of space limitation, this article just focuses on the detailed comparison between UNB PanSharp and Gram Schmidt, especially the fusion of WorldView-2 images, because previous research publications have proven that UNB PanSharp is the top one, followed by Gram Schmidt. For the fusion results of other algorithms and/or other satellites, readers can refer to the papers by Du et al. (2007), Nikolakopoulos (2008), Padwick et al. (2010), and Zhang and Mishra (2012).

Figure 1 shows a subset of the WorldView-2 Pan image used for fusion. The original size is 130 MP. **Figure 2** shows the MS images of different band combinations and the

corresponding fusion results of Fuze Go (UNB PanSharp) (FG), ENVI Gram Schmidt (GS1), and ESRI Gram Schmidt (GS2).

Figure 3 shows a few fusion examples of other satellites produced using Fuze Go, that is IKONOS, QuickBird, and GeoEye-1. Each of the fused images is larger than a quarter of the full image scenes.

4 Quality evaluation and analysis

4.1 Quality evaluation

To avoid bias in the fusion quality evaluation, all the images before and after pan-sharpening were displayed under the same visualisation condition in Figures 1–3 (i.e. exactly the same image area was displayed and the same histogram stretching was applied to all the images).

For spatial detail evaluation, readers can clearly see, by comparing Figures 1 and 2, that

- The spatial detail of the Fuze Go (FG) and ESRI Gram Schmidt (GS2) is identical to that of original Pan image, whereas
- The ENVI Gram Schmidt (GS1) results are blurred in all the band combinations.

For spectral quality evaluation, readers can see, by comparing the MS images and the pansharpened images in Figure 2, that

- Fuze Go (FG) produces almost identical colour to that of the original MS image in all the band combinations;
- ENVI Gram Schmidt (GS1) results in obvious colour distortion in all the band combinations and introduces strange artefacts in nature colour and band 1, 2, and 3 combination;

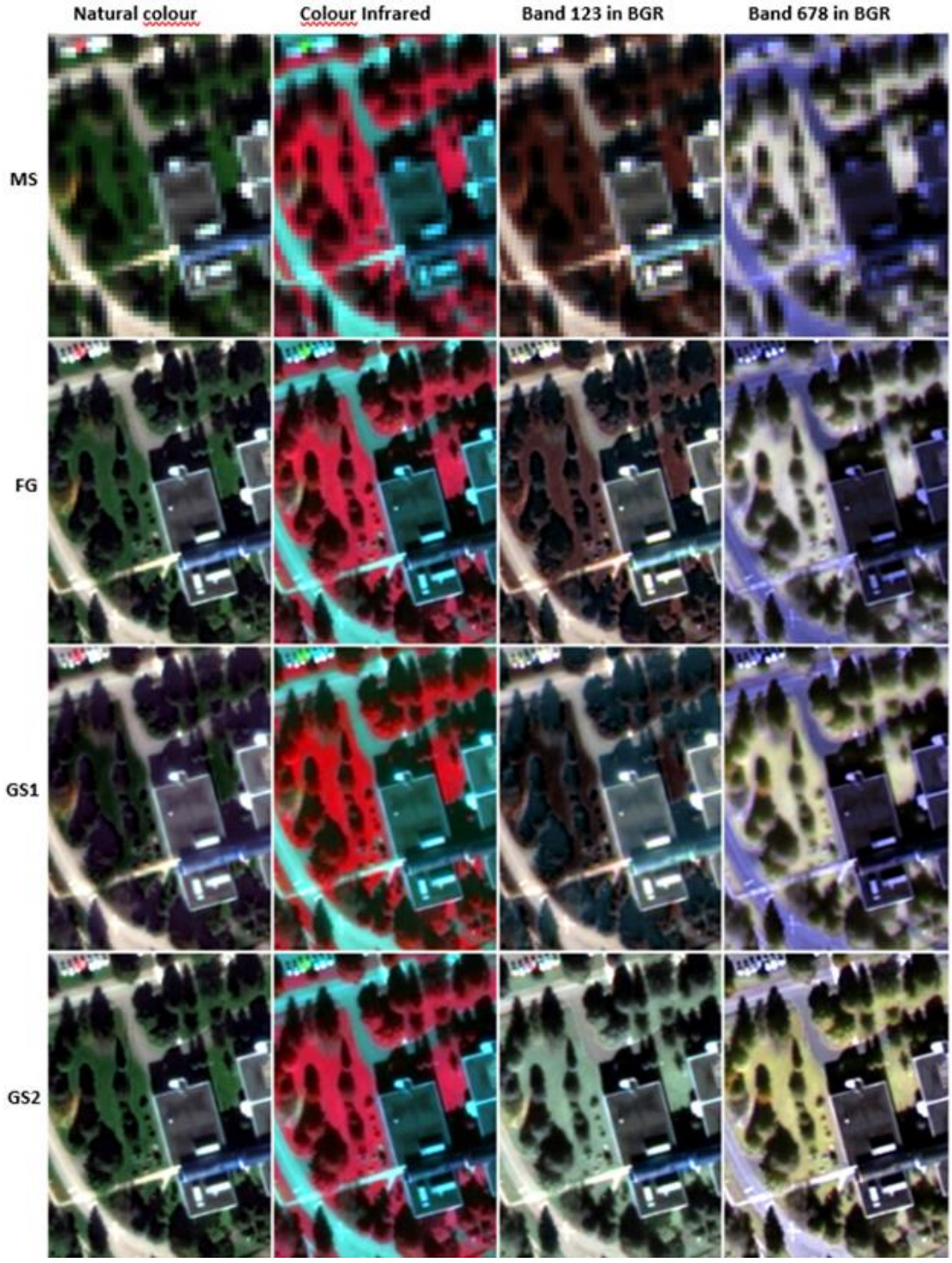

Figure 2 Subset of WorldView-2 MS images with different band combinations and the corresponding pan-sharpened results by Fuze Go (FG) (formerly UNB PanSharp), ENVI Gram Schmidt (GS1), and ESRI Gram Schmidt (GS2).

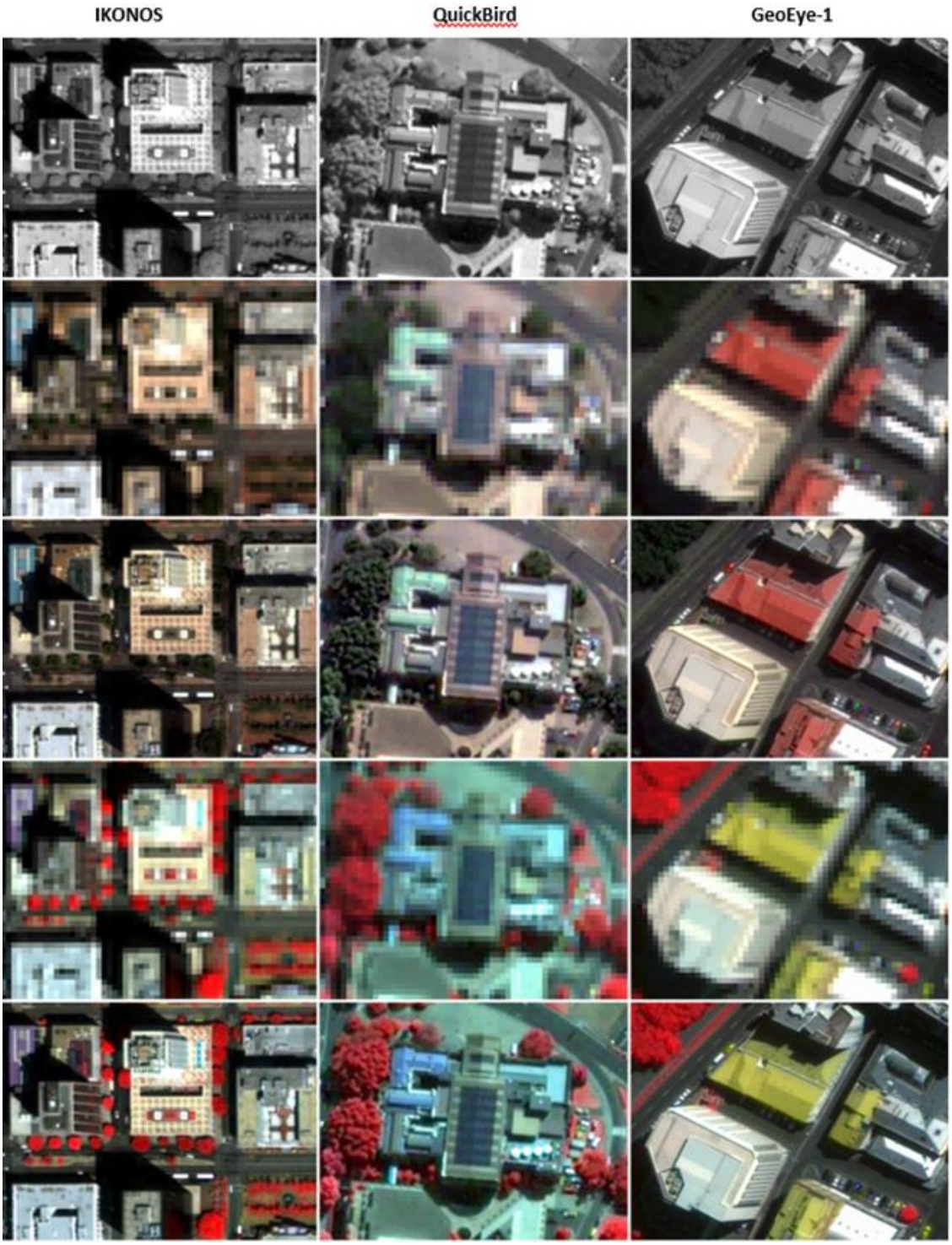

Figure 3 Original Pan and MS images and the pan-sharpened natural colour and colour infrared images of Fuze Go (formerly UNB PanSharp).

- ESRI Gram Schmidt (GS2) produces relative good fusion results for natural colour and colour infrared images with minor colour distortions, but with serious colour distortions for other band combinations.

From Figure 3, readers can also see that Fuze Go produces perfect fusion results, with identical spatial detail of the original Pan and the same colour of the original MS images, for all the band combinations of IKONOS, QuickBird, and GeoEye-1 images.

There are several methods discussed in the literature to evaluate both the spectral and spatial quality of pan-sharped images. However, currently there is no consensus in the literature (Li 2000, Padwick et al. 2010) on the best quality index for Pan-sharpening. In addition, our previous literature review and our previous research (Zhang 2008) also demonstrated that no existing quantitative methods can provide consistent and convincing evaluation results. Therefore, quantitative evaluation methods have not been used to evaluate the quality of Pan-sharped images.

4.2 Differences between Fuze Go and other algorithms

From the principles of the different pan-sharpening algorithms introduced in Section 2, we can see that:

- Most pan-sharpening algorithms (e.g. HPF, IHS, PCA, Brovey, and Wavelet) are developed based on the assumption that, except for the resolution difference, the grey value information of Pan and MS images are similar. Therefore, pan-sharpened results can be achieved by extracting high-resolution information from the Pan image and then adding it into all bands of the MS image.
- Many other pan-sharpening methods (e.g. Gram Schmidt and other modifies/ advanced algorithms) assume that the image difference caused by seasonal and

regional differences does not influence image fusion quality, as long as the sensor differences are taken into account. Therefore, one set of fusion parameters that are successful for some images of a specified sensor can be applied to the fusion of all images of the sensor, without considering the spectral differences caused by seasonal and regional differences.

However, both assumptions are not always true. Therefore, it happens often that a pansharpening algorithm achieves good results with some images, but fails with other images.

On the contrary, Fuze Go treats every set of Pan and MS images individually to find out the best fit between the Pan and MS images and then fuse them together. Therefore, it constantly achieves good fusion results regardless of the differences in sensors, seasons, and regions.

In other words, Fuze Go is an image-oriented pan-sharpening approach. It treats each set of Pan and MS images individually in the fusion. Therefore, it is sensor independent and achieves high quality fusion results for all sensors and all images.

However, other pan-sharpening algorithms are either sensor-oriented or sampleoriented approach, or both. They use a single set of fusion parameters extracted from some sample images to fuse all the images of the same sensor. Therefore, they achieve good fusion results with some images, but fail with other images.

5 Conclusion

Nine different pan-sharpening algorithms and their variations adopted by ERDAS, ENVI, PCI, and/or ESRI were evaluated and analysed in this article. From the tests of this research

and papers published by other researchers, it has been proven that Fuze Go and its predecessor UNB PanSharp produce consistent good fusion results for all sensors and all images. Gram Schmidt produces good fusion results for majority of images, but fails in the fusion of WorldView-2 images. Other pan-sharpening algorithms produce good results with some images and fail with others.

The quality inconsistency problem of Gram Schmidt and other pan-sharpening algorithms is due to the fact that the assumed conditions for developing the pan-sharpening algorithms are not always true in the real world. Therefore, good fusion results can be achieved when the images meet the assumed conditions. Otherwise, visible colours distortions and even strange artefacts will appear.

The reason for consistent good fusion results of Fuze Go is that it treats every set of Pan and MS images individually. It finds out the best fit between the Pan and MS images first and then fuses them together. Therefore, good fusion results can always be achieved regardless of the sensor, season, and region differences.

6 Funding

This research was supported by the GEOIDE MDF fund and Mitacs fund. The original Pan and MS satellite images were supported by DigitalGlobe Inc. and GeoEye Inc.

7 References

Ashraf, S., Brabyn, L., and Hicks, B.J. (2012). Image data fusion for the remote sensing of freshwater environments. *Applied Geography*, 32, 619–628.

Chavez, P.S., Sides, S.C., and Anderson, J.A. (1991). Comparison of three different methods to merge multiresolution and multispectral data: Landsat TM and SPOT panchromatic. *Photogrammetic Engineering and Remote Sensing*, 57 (3), 295–303.

Du, Q., Nicholas, H. Y., King, Rogers., & Shah, V. P. (2007). On the performance evaluation of pan-sharpening techniques. *IEEE Geoscience and Remote Sensing Letters*, 4 (4), 518–522.

ENVI. (2012). ENVI ver. 4.8 software help document. Boulder, CO: ITT Visual Information

Solutions.

ERDAS. (2010). ERDAS Imagine software help document. Norcross, GA: ERDAS.

ESRI ArcGIS Help 10.1. (2013). Fundamentals of panchromatic sharpening. Available from: http:// resources.arcgis.com/en/help/main/10.1/index.html#//009t000000mw000000 [Accessed 3 January 2013].

Gangkofner, U.G., Pradhan, P.S., and Holcomb, D.W. (2008). Optimizing the high-pass filter addition technique for image fusion. *Photogrammetric Engineering and Remote Sensing*, 74 (9), 1107–1118.

King, R. and Wang, J. (2001). A wavelet based algorithm for pan sharpening Landsat 7 imagery. *In: IEEE IGARSS*, Vol. 2, 9–13 July, Sydney, 849–851.

Klonus, S. and Ehlers, M. (2009). Performance of evaluation methods in image fusion. *In: Proceedings of 12th international conference on information fusion*, Seattle, WA, 6–9 July, 1409–1416.

Laben, C.A. and Brower, B.V. (1998). Process for enhancing the spatial resolution of multispectral imagery using pan-sharpening. United States Patent 6,011,875.

Lemeshewsky, G.P. (1999). Multispectral multisensor image fusion using wavelet transforms. *In: SPIE proceedings, Vol. 3716, visual image processing VIII. Reston, VI: US Department of the Interior, US Geological Survey*, 214–222.

Lemeshewsky, G.P. (2002). Multispectral image sharpening using a shift-invariant wavelet transform and adaptive processing of multiresolution edges. *In: SPIE proceedings, Vol. 4736, visual information processing XI*, 31 July.

Li, J. (2000). Spatial quality evaluation of fusion of different resolution images. *International Archives of Photogrammetry and Remote Sensing*, 33 (B2-2), 339–346.

Nikolakopoulos, K.G. (2008). Comparison of nine fusion techniques for very high resolution data. *Photogrammetric Engineering & Remote Sensing*, 74 (5), 647–659.

Padwick, C., Deskevich, M., Pacifici, F., & Smallwood., S. (2010). WorldView-2 Pan-Sharpening. *In: ASPRS 2010 annual conference*, 26–30 April, San Diego, CA.

Siddiqui, Y., 2003. The modified IHS method for fusing satellite imagery. *In: Proceedings of ASPRS 2003 annual conference*, 5–9 May, Anchorage, AK, 1–10.

Vrabel, J., Doraiswamy, P., McMurtrey, J. E., & Stern, A. (2002). Demonstration of the accuracy of improved resolution hyperspectral imagery. *In: SPIE proceedings, vol. 4725, algorithms and technologies for multispectral, hyperspectral, and ultraspectral imagery VIII*, 1 August, 556–567.

Zhang, Y. (2004). Highlight article: understanding image fusion. *Photogrammetric Engineering & Remote Sensing*, 70 (6), 657–661.

Zhang, Y. (2008). Methods for image fusion quality assessment – a review, comparison and analysis. *The International Archives of the Photogrammetry, Remote Sensing and Spatial Information Sciences*, XXXVII (Part B7), 3–11 July, The XXI ISPRS Congress, Beijing, 1101–1109.

Zhang, Y. (2010). Ten years of technology advancement in remote sensing and the research in the CRC-AGIP Lab in GGE. *Geomatica*, 64 (2), 173–189.

Zhang, Y., and Mishra, R.K. (2012). A review and comparison of commercially available pansharpening techniques for high resolution satellite image fusion. *In: Proceedings of IEEE International Geoscience and Remote Sensing Symposium (IGARSS)*, 22–27 July, Munich, 182–185.

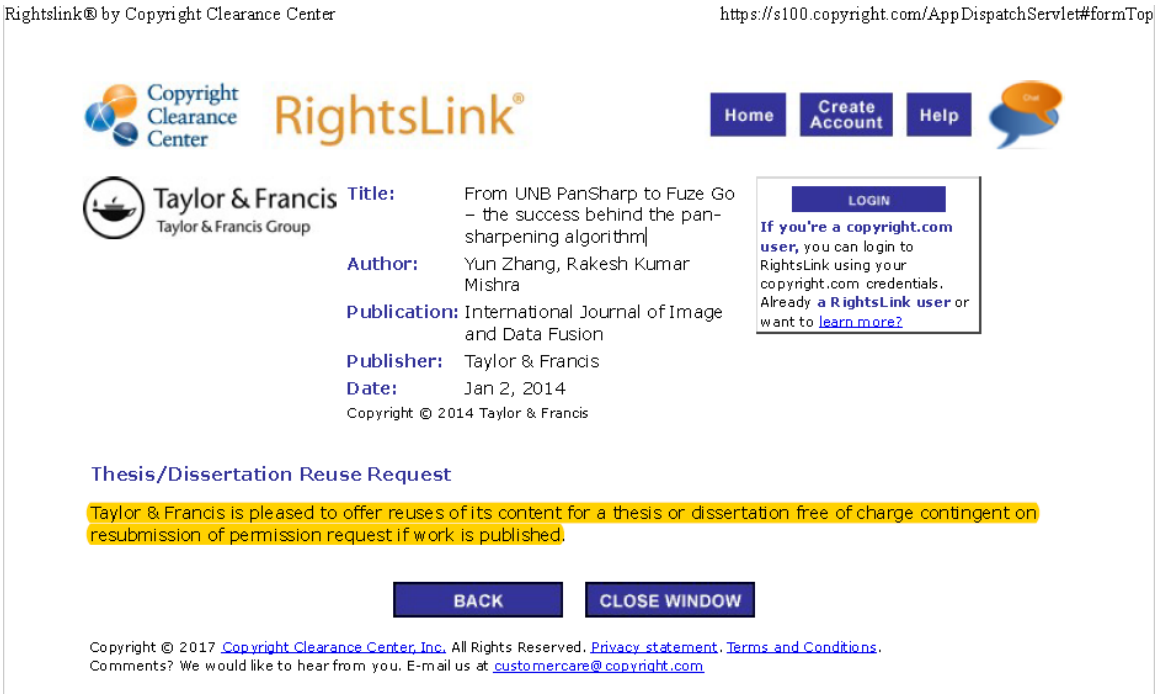

Appendix II A review of optical imagery and airborne LiDAR data registration methods

Mishra, R. K., & Zhang, Y. (2012). A review of optical imagery and airborne LiDAR data registration methods, The Open Remote Sensing Journal. vol. 5, pp. 54-63, 2012.

Abstract

Representing a scene completely from remote sensing data requires both spectral and 3-D-surface information. Integration of spectral information from optical images and 3-D-surface information from LiDAR is important in a number of remote sensing applications such as feature extraction, image classification, image analysis, building extraction, 3-D city modelling, canopy modelling etc. Therefore, numerous methods have been developed in the last decade to align both data sets into a common reference frame to effectively utilize their complementary characteristics. However, due to the significantly different characteristics between optical image and LiDAR data, there are a number of technical challenges in the alignment of both data sets. Different research papers introduced different strategy or methodology to overcome the challenges, reaching different alignment/registration results. This paper presents a review of classical and up to date optical-LiDAR registration methods with the emphasis on control point detection and matching. The aim of this paper is to provide readers with an overview of existing methods, identify their advantages and limitations, and give readers the overall information on what will be useful for researchers and practitioners to realistically select proper method for their application.

Keywords: Registration; Optical image; LiDAR; control point; feature detection; feature matching

1 Introduction

The technological advancement in computer, sensor technology, data processing and communication led to the launch of the new generation of High-Resolution (HR) commercial Earth imaging satellites. The HR satellite image has the advantage of high user interpretability, rich information content, high image clarity, and integrity, which opens the door for many new applications. The recently emerged technique of airborne altimetric LiDAR (Light detection and ranging) provides accurate 3-D surface information which helps in deciphering 3-D geometric information of ground features. However, sudden elevation changes along the surface are not clearly visible in the LiDAR data due to insufficient points. The LiDAR data provides high density surface information in homogenous areas and low density surface elsewhere (i.e. object space break-lines). On the other hand, an optical image provides high quality details along object boundaries with height variations (Kim et al., 2006). Optical images and LiDAR data have unique characteristics that make them preferable in certain applications. The disadvantage of one technology is contrasted by an opposite strength in the other. Hence, integrating of data from these two systems would lead to higher quality surface information (Baltsavias, 1999). Accurate registration of optical images and LiDAR data is important in a number of remote sensing applications such as:

a. Building extraction: In the past, many efforts have been made to automatically extract buildings from optical images or LiDAR derived DSM. Building extraction using either

optical image or LiDAR data has limitations due to the fact that both sensors have some limitations. Integration of these two data sets can overcome the limitations of optical and LiDAR sensors as both sensors have complementary characteristics. Many recent studies to extract buildings, use both optical image and LiDAR data together to improve the accuracy of the building extraction. Rottensteiner and Jansa (2002) have shown that the LiDAR data integration with optical imagery is helpful in building extraction. Integration of optical image with LiDAR data facilitates utilizing the characteristics of both data sets in building extraction. However, the prerequisite of using both data sets together is accurate alignment of both data sets in a common reference frame.

b. Image classification: At present, the image classification algorithms mainly use either spectral or contextual information of optical images for land-cover classifications. The object-oriented image classification method has been found better over the pixel-based image classification methods particularly for HR optical images. However, there is still enough scope in improving the image classification so the results can be used on operational basis. Integration of optical images and LiDAR data can greatly improve the classification accuracy by sharing redundant and complementary information of both data sets (Haitao et al. 2007). A number of research works have been done to utilize LiDAR data to improve the classification of optical images (Haitao et al. ,2007; Cui et al., 2006; Syed et al., 2005; Park et al., 2001). However, to use LiDAR data in image classification, the LiDAR data should be perfectly registered with the corresponding optical image.

c. 3-D City Modelling: 3-D city modelling is useful in understanding a scene of interest (Mastin et al., 2009). This has gained popularity in games and many commercial applications. 3-D city modelling has many valuable applications such as urban planning

and simulation, virtual reality, interpretation, and real-time emergency response. 3-D models are constructed by texture mapping of optical images onto 3D geometry models. These models have traditionally been constructed manually. The LiDAR technology has made the acquisition of high-resolution elevation data more efficient and cost effective. Brenner (2005) reviewed many building reconstruction methods and concluded that combining optical images with LiDAR data is the better way to increase automation and obtain accurate results. However, using LiDAR data in 3-D city modelling needs optical images accurately registered with corresponding LiDAR data.

d. Canopy modelling: Many research works have utilized the spectral characteristics of optical images to detect forest and tree crowns. However, optical images are not good enough to model canopy structure as it does not capture forest structure directly. As LiDAR data provides very accurate and dense horizontal and vertical information, the canopy height can directly be retrieved from LiDAR data. Chen et al. (2005) have shown that the use of LiDAR data with optical images is useful in canopy modelling. The precise canopy modelling requires optical images accurately registered with corresponding LiDAR data.

However, due to the distinguished differences between optical image and LiDAR data, the registration remains challenging.

2 Difficulties in optical image and LiDAR data registration

A complete scene description from remote sensing data requires both spectral and 3-D surface information. However, the complementary information of optical images and LiDAR data can be fully utilized only after precise registration of both data sets. Therefore, registration of optical images and LiDAR data models relative to a common reference

frame (Habib and Schenk, 1999; Postolov et al., 1999) is highly beneficial for many remote sensing applications. The optical image can be aligned with the corresponding LiDAR data manually or automatically through an image registration process using control points. The manual process is performed by selecting control point pairs from both data sets. This process is very time consuming and is prone to human bias given a large area. Therefore, automated registration process is highly desirable to reduce processing time. An optical image and corresponding LiDAR data are shown in Figure 1. In Figure 1, the potential control points, building corners are highlighted with yellow circles. There are various important issues which make optical image and LiDAR data registration a quite difficult task (Wong and Orchard, 2008). These are given as follows:

a. Control-Point Detection: To register a pair of images with each other, a set of conjugate control-points must be detected from both images to compute the registration parameters. However, there are substantial differences in characteristics of optical images and LiDAR data. Therefore, it is very difficult to determine the same points of interest in both data sets.

b. Difference in characteristics of optical image and LiDAR intensity image: There are substantial differences between an optical image and a LiDAR intensity image due to their very different processes of intensity recording. This makes it difficult to perform a direct similarity comparison between a LiDAR intensity image and an optical image. However, the intensity image from LiDAR sensor can be used to improve the registration accuracy. Further, the elevation image (DSM) obtained by LiDAR data has also very different characteristics than the optical image.

c. Different Structure: As the optical and LiDAR sensors capture data in entirely different environments, the structural characteristics recorded by optical image may not be present

in LiDAR data or vice-versa. This makes it difficult to perform comparisons of structures appearing in both data sets such as edges and shapes.

d. Relief displacement: In the HR optical images relief displacement is highly apparent. Relief displacement shifts the position of an object's image caused by the relief of the object. There is no relief displacement in LiDAR data. Therefore, shift of objects (control-points) in optical images makes it difficult to associate control-points of optical images with control-points in LiDAR data.

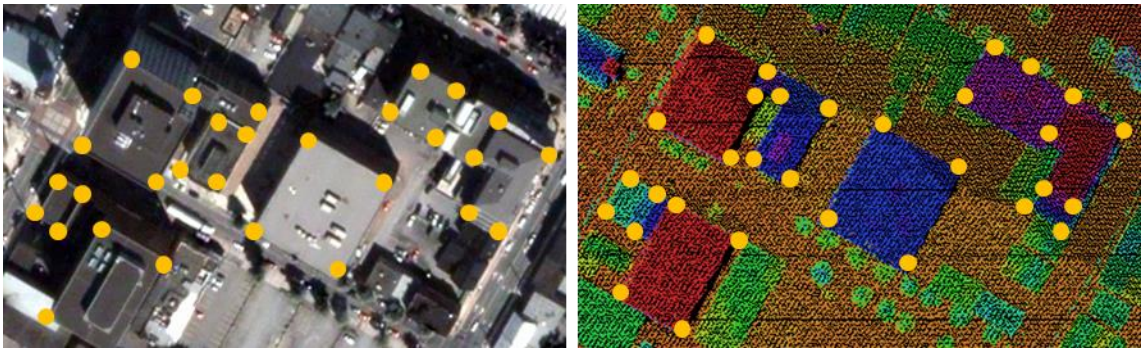

Figure 1 Optical image (left) and corresponding LiDAR data (right). Notes: The yellow circles in this Figure represent the building corners. These corners are the potential control points for optical image and LiDAR data registration.

3 Optical image and LiDAR data registration methodology

The optical images and LiDAR data registration methods consist of following three steps:

a. Feature Extraction: Salient and distinctive features (homogenous regions, edges, object boundary, lines, line intersection, corners, etc.) are manually or automatically detected from optical images and LiDAR data. These features can be represented by their lines, corners, center of gravity, etc. which are called control points.

c. Feature matching: This step determines correspondence between the control points detected in optical images and LiDAR data. Many similarity measures and feature descriptors are used for matching the control points.

d. Transformation model: Image transformation parameters are computed using correspondence between the matched control points from optical images and LiDAR data.

The above steps are similar to steps required for image-to-image registration (Zitova and Flusser, 2003). Many successful methods have been developed for the registration of the optical images. However, given the substantially different imaging principles between optical and LiDAR sensors, the captured data sets exhibit substantially different characteristics. Therefore, the method proposed for image-to-image registration cannot be directly applied to register optical images and LiDAR data. Intensity based methods for image registrations are not suitable for optical images and LiDAR data registration since there are substantial differences in their data characteristics. The 3-D surface can be generated using photogrammetry techniques and then registration of optical images and LiDAR data can be done (Shenk and Castho, 2002); however, it requires overlapping optical images and processes are not automatic. Feature-based techniques are suitable for this type of registration as features can be extracted both from optical images and LiDAR data. The result of featured-based technique depends on the similarity of image features determined by feature extraction algorithms. The main problem with optical images and LiDAR data registration is to determine correct control points from both data sets and then their accurate matching. As discussed above, due to the importance of optical image and LiDAR data registration in many remote sensing applications, several methods have been developed over time to solve the problems of this type of registration. These methods are categorized as per their types and discussed as follows in detail:

3.1 Featured based registration

Feature-based methods have been found better than the intensity based registration methods as many similar features are present in both optical images and LiDAR data sets. These methods depend on the features determined by feature extraction algorithms. The detection of control-points depends on feature extraction as control points that correspond to positions of image fragments with particular features (Zitova and Flusser, 2003). Therefore, feature extraction is crucial for successful optical image and LiDAR data registration. Linear features, corners, lines and polygons are considered as features here.

3.1.1 Corner: Corners are the most common features used for image-to-image registration (Zheng et al., 1999). The advantages of using corner points are their uniqueness and high precision in their localization. Wong and Orchard (2008) were used modified Harris corner detector (Noble 1989) to detect corners (control points) from the optical image and then corresponding control points from the LiDAR data was extracted through exhaustive search.

3.1.2 Straight lines: An optical image and LiDAR data registration method proposed by Habib et al. (2004) utilizes straight line features extracted from both data sets and 3-D similarity transformation for aligning the optical image relative to the corresponding LiDAR data reference frame. The straight line features are used due to the fact that the straight lines can be reliably, accurately and automatically extracted from both optical images and LiDAR data. In this approach, first, planer surfaces from LiDAR data are extracted and adjacent planes are intersected to determine 3-D straight line segments. Secondly, linear features from optical images are obtained through aerial triangulation. A mathematical model for expressing the necessary constraints for the alignment of conjugate

optical images and LiDAR data straight lines is established. This model ensures that the corresponding straight lines are collinear after registering two data sets relative to a common reference frame.

Habib et al. (2005) introduced another approach which starts by manipulating the photogrammetric imagery to produce a 3-D model, including a set of linear features along object space discontinuities, relative to an arbitrarily chosen coordinate system. Then, conjugate photogrammetric and LiDAR straight line features are used to establish the transformation between the arbitrarily chosen photogrammetric coordinate system and the LiDAR reference frame.

Habib et al. (2006) proposed an alternative method for the purpose of integrating LiDAR data into photogrammetric triangulations. Two methodologies are introduced that utilize straight line and aerial features derived from both data sets as primitives. The first methodology directly incorporates LiDAR lines as control information in the photogrammetric triangulation, while in the second methodology, LiDAR patches are used to geo-reference the photogrammetric model.

Deng et al. (2008) proposed a registration procedure in which first straight lines are detected using Canny edge detection. Then pair-wise correspondence of detected straight lines is achieved by matching the straight-line pairs detected from LiDAR point clouds and optical images using generalized point photogrammetry. In the generalized point photogrammetry, all kinds of features are treated as generalized points and incorporated into extended collinearity equations (Zhang, et al, 2008). The collinear condition is applied in generalized point photogrammetry to match straight lines.

3.1.3 Sensor invariant features: Schenk and Csatho (2002)fused aerial images with LiDAR data to obtain better scene description of topography. This method utilizes the sensor invariant features found in both data sets at the registration stage. Such features correspond to the same object space phenomena, for example breaklines and surface patches. Matched sensor invariant features have been used to establish a common reference frame. Feature-level fusion has been performed with sensor specific features that are related to surface characteristics.

3.1.4 Building roofs: Building roofs are frequently used for optical images and LiDAR data registration as building roofs are linear features and available in both data sets. A method for optical images and LiDAR data registration has been proposed by Kwak et al., (2006) which uses centroids of plane roof surfaces as control information. This research was done on scenes where roofs are plane. The centroids of the plane roofs were extracted from the optical image using Canny edge detector. Then, Local Maximum Filter was used to extract centroids of the plane roofs from the LiDAR data. The extracted centroids from the LiDAR data were used as control information to compute exterior orientation parameters of optical (aerial) imagery. For verification purposes, exterior parameters were computed using GCPs (Ground Control Points) and the accuracy of registration is evaluated. This research shows that the centroid of a building roof is a useful source of control information.

Shorter and Kasparis (2008) were proposed a registration method which uses building roofs resent in optical image and LiDAR data. In this method, first, buildings present in an optical image and LiDAR data were detected. Then, the LiDAR data was interpolated to a fixed point spacing (DSM) to produce a binary building mask. In the binary building mask image, the bright pixels correspond to buildings and dark pixels to everything else. In the

next step, buildings from the optical image were detected and then the binary building mask was generated. The 2-D Fourier transform and 2-D log polar Fourier transform of both images were computed. The computed 2-D Fourier transforms and phases of the log polar 2-D Fourier transforms of the optical image and LiDAR data were used to compute parameters for translation, rotation and scaling geometric transformations (Reddey et al. 1996). The computed transformation parameters were then used to register optical images and LiDAR data.

3.1.5 Displacement correction method: A two-step displacement correction method for LiDAR point cloud and aerial images registration is proposed by Wu et al. (2010). This is a linear registration approach for LiDAR data and aerial images registration without using orientation parameters. Pre-processing is performed on LiDAR data to classify the point cloud into ground-points, building points, and above ground points. These classified LiDAR point clouds are used in two displacement correction steps to select control points for the registration. These two displacements corrections are tilt displacement corrections and height displacement corrections. The tilt displacement is defined as displacement caused by the non-parallelity of the image plane and the datum plane in the object space. An algorithm has been developed to remove tilt displacement which creates a functional relationship to map the datum plane to the image plane. The height displacement correction algorithm has been developed to remove the displacement caused by the perspective geometry of the camera and the height difference of each LiDAR point relative to the datum plane. The control points are selected manually in the LiDAR point cloud and aerial image respectively. The control points are divided into two groups; one group is ground points which are used for tilt displacement correction. Another type of control points are object

points. Object points are mainly roof corners, which are used for height displacement correction.

3.1.6 Summary: As per the above discussions, it has been investigated that the feature-based registration method is relatively well suited for optical images and LiDAR data as these data sets contains enough distinctive and easily detectable objects required for registration. Registration of optical images and LiDAR data has been often performed by using building roofs as control information; however, the use of roof as control information is limited by the fact that many natural scenes do not contain buildings. Mostly remote sensing data contains both manmade objects such as buildings, roads, etc. and natural objects such as rivers, forests, etc. The feature-based registration methods are not very effective for the natural settings. Furthermore, the main problem with feature based registration is that the optical image and LIDAR data often capture different feature characteristics that make feature-based techniques less effective. A two-step displacement correction algorithm for optical image and LiDAR data registration without using orientation parameters proposed by Wu et al. (2010) have achieved the same accuracy level as the traditional photogrammetric space resection algorithm. However, the problem associated with this approach is that the selections of control points are manual. The advantages and limitations of feature based algorithms are discussed in Table 1.

Table 1 Advantages and limitations of feature-based algorithms

Category	Advantages	Limitations
Corners	• Uniqueness and high precision in their localization • Suitable for urban environment • Fast computation	• Same corners may not be present in optical images and LiDAR data • Not suitable for natural environment
Straight lines	• Can be reliably, accurately and automatically extracted from both optical image and LiDAR data • Suitable for urban environment	• Need overlapping optical images to generated 3-D model • Not suitable for natural environment
Sensor invariant features	• Breaklines and surface patches are common in optical images and LiDAR data • Suitable for both urban and natural environment	• Need stereopair aerial images to orient aerial images with LiDAR data • Computationally expensive
Building roofs	• Suitable for urban environment • Excellent source of information for control points	• Same building structures may not be present in optical images and LiDAR data • Performance is poor if building roofs are complex • Not suitable for natural environment
Displacement correction method	• Better registration accuracy • There is no need of orientation parameters	• Manual selection of control points from optical images and LiDAR data • Not suitable for natural environment

3.2 Mutual information based registration

As discussed in aforesaid registration methods, the majority of feature based registration methods utilizes only one type of features. However, as characteristics of optical images

and LiDAR data are very different and many features available in one data set may not be available in others, registration using single features does not produce accurate registration results. To overcome this problem, statistical and information-theoretic methods have been extensively used for multi-modal image registration. This method is called mutual information (MI) registration, which provides a means to measure statistical dependence between two random variables or the amount of information that one variable contains about other. The basic concept behind the use of MI for registering images is that MI (similarity matrix) calculated from the two images will reach its maximum MI when the images are perfectly geometrically aligned (Viola and Wells, 1997). A MI based approach to register optical images with LiDAR data has also been proposed by Mastin et al, (2009). This approach evaluates registration statistics in the 2-D image plane via projection of LiDAR features within the constraints of a camera model for comparison with the image features. MI based registration methods seek the camera matrix that maximizes the MI between the distribution of image features and projected LiDAR features.

MI is defined in terms of entropies of the optical image features, LiDAR data features and their joint entropy (Mastin et al., 2009):

$$I(u; v_T) = H(u) + H(v_T) - H(u, v_T) \qquad (1)$$

where u is the features in an optical image and v_T is the features in projected LiDAR data in 2-D space.

The entropy of optical image features remains constant and the entropy of the LiDAR features remains approximately constant. The registration algorithm discussed in Mastin et al. (2009) renders 3-D LiDAR data points onto the optical image plane for evaluating statistics. The three different methods for evaluating MI between optical image and

projected LiDAR data have been proposed. The first method simply uses the mutual information between elevation in the LiDAR point cloud and luminance in the optical image. The point cloud is rendered with height intensities, where the brighter point indicates a higher elevation. Only image pixels that have corresponding projected LiDAR points are used for calculating registration statistics. The reason for doing this is that the visual appearance of urban scenes tends to vary structurally by height for architectural regions. Also, there is measurable dependence between the optical appearance and the measured LiDAR height. A scene shown by both modalities is shown in Figure 2(a) and Figure 2(b). The second method uses the mutual information between luminance in the optical image and intensity values in the LiDAR point cloud. A LiDAR intensity image is shown in Figure 2 (c). The walkway between the buildings can easily be seen in the LiDAR intensity image. Finally, the third method calculates entropy among optical image luminance, LiDAR elevation and LiDAR intensity values. It is assumed that the LiDAR intensity image is statistically independent of the LiDAR elevation image. This leads to the following joint entropy:

$$\boldsymbol{H}(\boldsymbol{u}, \boldsymbol{v_e}, \boldsymbol{v_i}) = \boldsymbol{H}(\boldsymbol{u}, \boldsymbol{v_e}) + \boldsymbol{H}(\boldsymbol{u}, \boldsymbol{v_i}) \qquad (2)$$

where u is the image luminance, v_e is the LiDAR elevation, and v_i is the LiDAR intensity values.

Based on the joint entropy the registration statistics is calculated. The oblique aerial photographs are used in this research since this research is aimed to produce 3-D models of urban scenes.

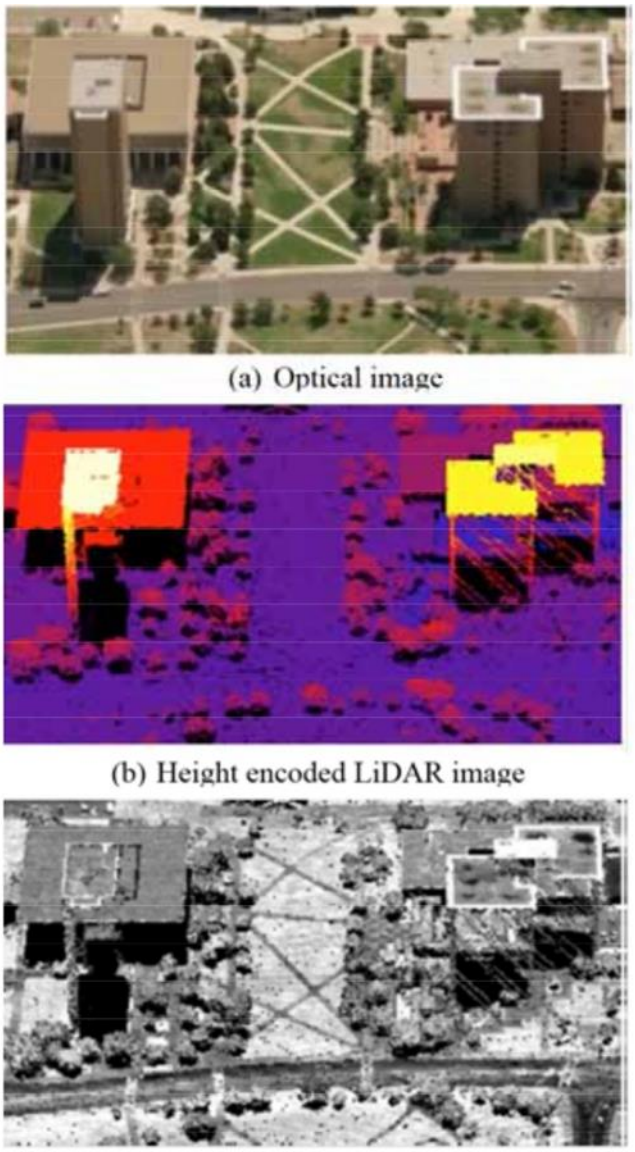

Figure 2 Detail of optical and LiDAR data. Note: (a) Shows an optical image of two buildings with pathways in between, (b) shows the registered LiDAR data set of the same scene with intensity encoded, while (c) shows the LiDAR data with the Pdet attribute. Courtesy: (Mastin et a., 2009), Computer Vision and Pattern Recognition, CVPR 200, IEEE Conference.

3.2.1 Summary: From the MI based registration methods, it can be concluded that the mutual information based methods are better than the feature based methods as they include

different features at the same time. The mutual information based registration method proposed by Mastin et al. (2009) has been achieved using 3D-2D rendering of height and probability of detection attributes of the LiDAR system. The registration accuracy is shown on average to be 90% when both LiDAR elevation and a LiDAR intensity images are used in registration. The registration accuracy is slightly less when only LiDAR elevation image is used which shows that the use of a LiDAR intensity image can improve registration accuracy. The mutual based registration methods have shown their effectiveness for urban scenes; however, it is ineffective for natural scenes as information-theoretic methods cannot be applied to natural scenes.

3.3 Frequency based registration

Frequency based methods have been frequently used in optical image registration (Castro and Morandi, 1987;, Reddy and Chatterji, 1996; Zavorin and Moigne, 2005). Frequency based methods use phase to determine the alignment between two images. One of the popular frequency based method is phase correlation, which has been extended to handle geometric distortions such as rotation and scaling (Reddy and Chatterji, 1996). These frequency based methods cannot be applied directly to register optical images and LiDAR data due to differences in data characteristics. An improved version of the frequency based method to register optical images and LiDAR data has been developed by Wong and Orchard (2008). In this proposed algorithm, the control points are extracted only from an optical image. To extract control points, this algorithm applies local normalization on an optical image to compensate for non-uniformity in image illumination and contrast. Then a modified Harris corner detector is applied (Noble, 1980). Only the strongest control points are selected based on threshold values. Once control points from optical image are

detected, an exhaustive region correspondence search algorithm is applied to find the optimal correspondence between regions from an optical image to a LiDAR image. Fourier transform (FFT) (Cooley and Tukey, 1965) has been used to reduce the cost of an exhaustive search. The problem of different intensity image characteristics of optical and LiDAR images has been solved through an integrated local intensity mapping transformation optimization process.

Figure 3: Final set of detected control points (as indicated by crosses). (Left) Optical image. (Right) LiDAR image. Note: This Figure shows the effectiveness of the methodology developed by Wong and Orchard [13] in control point detection. Courtesy: (Wong and Orchard 2008), IEEE transactions on Geoscience and Remote Sensing.

Wong and Orchard (2008) used the 4th random sample consensus (RANSAC) algorithm to remove incorrect control-point pairs to improve registration process. A final set of control points in the optical and the LiDAR intensity image are shown in Figure 3.

The method proposed by Wong and Orchard (2008) determines the image transformation model and estimates the transformation parameters from the initial sample of control-points. This method calculates close values of transformation parameters (e.g. sift, rotation, and scale) for the corresponding control-points.

3.3.1 Summary: The frequency based method used for optical image and LiDAR data registration uses only LiDAR intensity images which contain less information about the topography as compared to LiDAR elevation images. A LiDAR intensity image can be used to improve registration accuracy; however, using only LiDAR intensity images for registration purposes is not enough to produce accurate registration results. The registration method produced by Wong and Orchard (2008) has introduced the region correspondence search that uses Fourier transform (FFT) (Cooley and Tukey 1965) to reduce the cost of an exhaustive search. Wong and Orchard (2008) claims that the developed methodology for optical images and LiDAR data registration produces good level of accuracy under various difficult optical and LiDAR image pairs. Wong and Orchard (2008) have used orthorectified low-resolution optical images to test the developed algorithms; however, today very high-resolution satellite imagery is available which is more useful for various remote sensing applications.

3.4. Salient-point based registration

The optical image and LiDAR data registration techniques discussed in the above section are mostly suitable for man-made settlements and are not well suitable for the natural scenes where building, roads, etc. are not present. Considering the general type of features present in remote sensing data a salient point approach with combination of multiscale image analysis (Zheng et al., 1999) is helpful to improve overall registration accuracy. The

general overview of a salient-point detector in the context of image matching is given in (Sebe, 2003; Lindeberg, 1998). Salient points in images refer to image locations with distinctive features providing discrimination between objects of interest and the background (Palenichka and Zaremba, 2010). A salient-point detector is a visual operator used to find image locations or regions containing object of interests (Kadir and Brady, 2001; Itti, et al., 1998; Reisfeld, et al., 1995; Tagare et al., 2001; Lowe 2004, Harris and Stephens, 1998). A salient-point visual operator can detect various types of salient features such as corners, lines, junctions, intensity blobs, and homogenous regions (Zheng et al., 1999; Itti et al., 1998; Alhichri and Kamel, 2003; Palenichka and Zaremba 2005). Although, these techniques have proven their effectiveness for control-point extraction, there are, however, many weaknesses (Palenichka and Zaremba, 2010). Feature extraction and salient point detection using these techniques gives poor results at a large scale during image analysis. Irrelevant sharp edges may become more highlighted than salient regions and corners (Lindeberg, 1998; Kadir and Brady, 2001; Lowe, 2004). Difficulties in salient-points detection appear when edges in images are not sharp or corrupted by noise.

To overcome the aforesaid shortcomings (Palenichka and Zaremba, 2010) proposed a new method of control point extraction using a salient visual operator. The purposed solution was designed with the intention to register optical images and LiDAR data automatically with high accuracy. The development of control point extraction schemes starts with an extraction of image fragments which satisfy given requirements for intensity and shape features (local features). The centers of these image fragments were considered as control points. The control point extraction was realized using the concept of multiscale salient image discs (SIDs). The multiscale SID concept is an extension of a salient point

method of feature extraction for multiscale high-contrast homogenous regions (Kadir and Brady, 2001; Itti and Niebur, 1998). A SID is defined (Palenichka and Zaremba ,2010) as a circular image fragment of a variable diameter, which is inscribed into a homogeneous region (i.e., is tangent to the background in at least two points) and has the local maximum of contrast-to-homogeneity ratio. Three SID image descriptors were introduced: 1) planar pose characteristics (e.g. center coordinates, local scale, and local orientation); 2) planar shape descriptors; and 3) image intensity descriptors. The control points selected are the centers of those SIDs.

In the approach of Palenichka and Zaremba (2010), a multiscale isotropic matched filtering (MIMF) was developed to effectively identify candidate SID positions. MIMF was used to extract SIDs from images in a way that is invariant to translation, scale and rotation. The MIMF operator was originally developed by Palenichka and Zaremba (2005) to detect individual trees in LiDAR images. This MIMF operator was modified to detect SIDs both from optical images and LiDAR data. This operator does not require pre-segmentation images. The MIMF operator produces two sets of detected control points from optical images and LiDAR data.

Intersection matching distance (IMD) algorithm was developed to establish pair wise correspondence between two sets of extracted SIDs. This algorithm is based on the minimization of a dissimilarity measures (i.e. a distance between two sets of descriptor vectors) over all possible subsets of control point SIDs detected from optical image and LiDAR data.

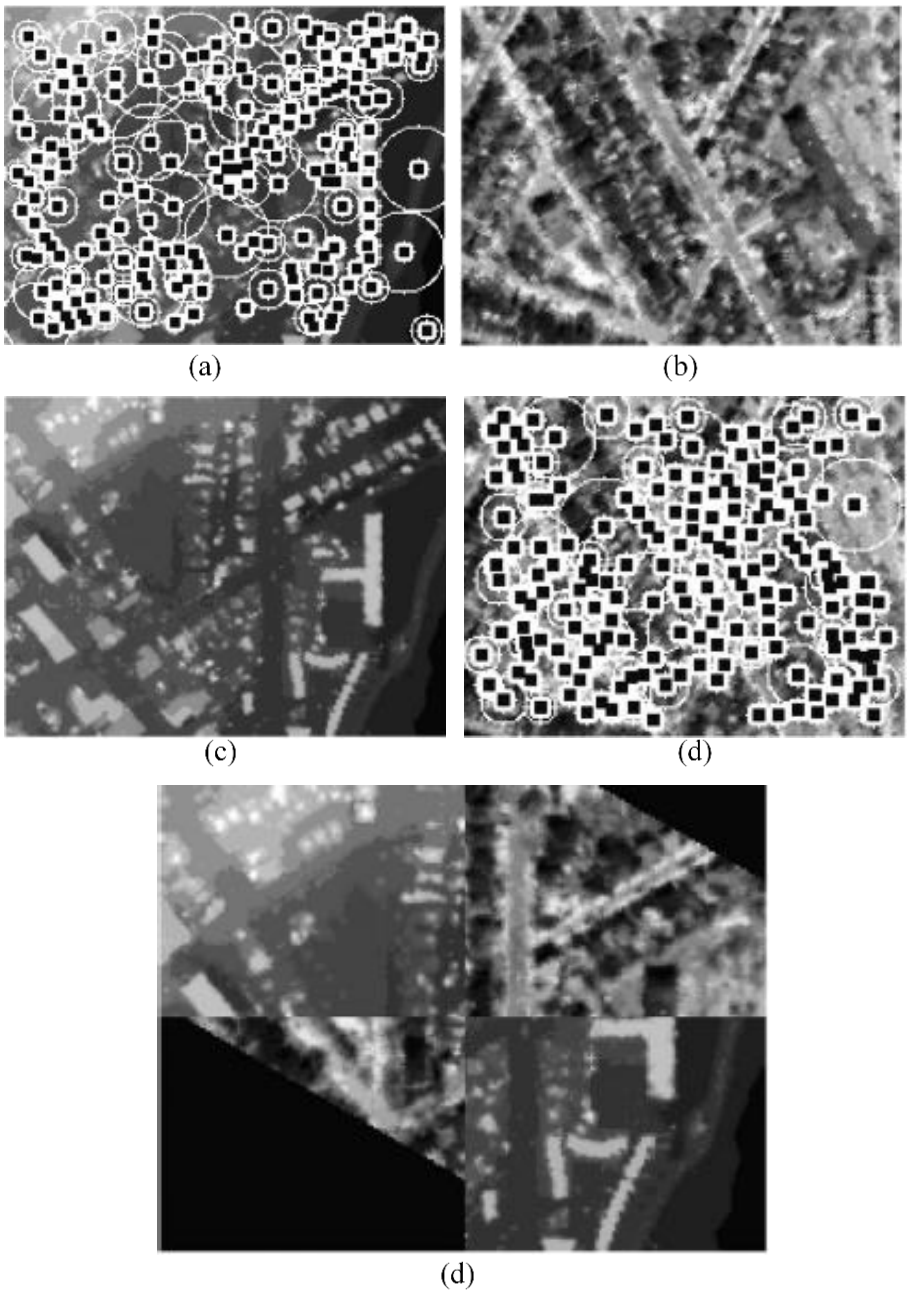

Figure 4: Example of a heterogeneous image registration (Ottawa test area). (a) A LiDAR height image. (b) A rotated and shifted panchromatic image. (c) SID extraction from a LiDAR image. (d) SID extraction from a panchromatic image. (e) An image registration result. Courtesy: (Palenichka and Zaremba, 2010) IEEE transactions on Geosciences and Remote Sensing.

Experiments of the developed algorithms were done using Quickbird imagery and LiDAR generated DSM images. Optical images and LiDAR data for the forest and urban areas were registered to show the effectiveness of the developed algorithm. The performance of the SID extraction is evaluated by the receiver operating characteristics (ROC) method. The similarity transformation mapping method was used to estimate transformation models using SIDs pair correspondence. Figure 4 shows the registration result with four quadrants: two diagonal quadrants from the LiDAR image and other two from the transformed optical image.

3.4.1 Summary: The multiscale version of a salient point approach is suitable when combining optical images with LiDAR data as both data sets may have different resolution. This technique facilitates automatic selection of multiple control points even for images of natural scenes. Moreover, multitude of control points with their relative location enhances the accuracy of registration. Location saliency ensures the uniqueness of control points in images which is important for control point extraction. The old saliency based methods have problems: a lack of explicit saliency conditions, poor results on feature extraction, and a high computational cost. The saliency based approach proposed by Palenichka and Zaremba (2010) to register optical images with LiDAR data aims to overcome these problems of saliency based methods. This approach automatically extracts control points from optical images and LiDAR data using transformation-invariant detection of image discs (SIDs). Pair-wise correspondence between two sets of extracted SIDs is determined by the calculation of the IMD. Finally, registration of optical images and LiDAR data is performed using a similarity transformation model. This technique has shown good accuracy in control point extraction from both optical images and LiDAR data. Also, the

registration results are relatively good particularly for natural scenes. However, the problem of relief displacement, which is apparently present in HR imagery, has not been addressed. Moreover, the developed technique is complex and is computationally expensive thus difficult to implement for real world applications.

3.5 Analysis of the advantages and limitations of different approaches

Many research works have been done on accurate registration of optical images with LiDAR data since integration of these two data sets is important for various remote sensing applications. In conclusion advantages and disadvantages of existing methods to register optical images with LiDAR data are listed in the Table-2 and discussed as follows.

3.5.1 Feature-based methods: Feature-based methods have been considered effective for the alignment of optical images with LiDAR data as optical and LiDAR sensors capture distinguishable features. Feature-based methods have been widely used for image-to-image registration. The feature-based methods have been modified to register optical images and LiDAR data. However, the main problem with feature based registration is that the optical images and LIDAR data often capture different feature characteristics that make feature-based techniques less effective. Also, the majority of feature based registration methods utilizes only one type of features. Furthermore, mostly remote sensing data contains both manmade and natural objects such as buildings, roads, and rivers, forests respectively. The feature-based methods are less effective for the regions where natural objects (river, lakes, forest, etc.) are present.

Table 2: Advantages and limitations of optical images and LiDAR data registration methods.

Category	Advantages	Limitations
Feature-based methods	• Distinguishable features are available in optical images and LiDAR data • Suitable for urban environment • Fast computation	• Optical images and LIDAR data often capture different feature characteristics • Not suitable for natural environment
Mutual information based methods	• It includes different features at the same time • Suitable for urban environment	• Not suitable for natural environment
Frequency-based methods	• Fast computation	• Uses only LiDAR intensity images • Low registration accuracy
Salient point based methods	• Suitable for urban and natural environment • Better registration accuracy	• Computationally expensive • Do not consider relief displacement present in HR imagery

3.5.2 Mutual information (MI) based methods: The methodology developed by Mastin et al. (2009)[8] to register optical images and LiDAR data shows that the MI-based methods are better compared to the feature-based methods as it includes different features at the same time. The registration accuracy was shown on average to be 90% when both LiDAR

elevation and LiDAR intensity images are used in registration. The mutual based registration has shown its effectiveness for the urban scenes, however, it is ineffective for the natural scenes as information-theoretic methods cannot be applied to natural scenes.

3.5.3 Frequency-based methods: Most of the frequency based method used for optical images and LiDAR data registration uses only intensity images of LiDAR which contain less information about the topography compared to LiDAR elevation images. Also, the nature of optical images and LiDAR intensity images are very different in nature. The LiDAR intensity images can be used to improve registration accuracy; however, using only LiDAR intensity images for registration purpose is not enough to produce accurate registration result.

3.5.4 Salient point based methods: A salient point approach with a combination of multiscale image analysis suggested by Palenichka and Zaremba (2010) has shown relatively better result than the earlier registration techniques particularly for natural scenes. However, the problem of relief displacement present in HR optical images has not been addressed. Moreover, this technique includes complex algorithms which are computationally expensive and hence difficult to implement for real world applications.

4. Conclusion

Optical images and LiDAR data registration is a prerequisite to utilize the complementary characteristics of both data sets. Accurate registration between optical image and LiDAR data is vital for many remote sensing applications such as; feature extraction, image classification, 3D city modelling, and canopy modelling. This paper did a survey of the classical and up-to-date registration methods developed to register optical images and

LiDAR data. The registration methods are grouped into different categories according to the nature of their calculation principles. Although many methods have been developed in the last decade for the registration of optical image and LiDAR data, however:

- In spite of different characteristics of optical images and LiDAR data, many methods are still using the previously developed algorithms for image-to-image registration.
- Automatic and accurate registration of these data sets still remains an open problem.
- No techniques have been found that can register optical images and LiDAR data automatically with the required accuracy and efficiency for practical applications.

5. Future outlook

As per the review of the existing registration methods, it has been found that the use of a multiscale saliency based approach is best suited to detect control points from both data sets. The interest point matching algorithm (Xiong and Zhang, 2009), which provide accurate and efficient matching of image control points in optical images may have potential to be extended to match detected control points from optical images and LiDAR data. The problem of relief displacement of HR imagery is another issue for accurate registration between optical image and LiDAR data. It is also important to incorporate sensor information of optical and LiDAR sensors to solve the relief displacement problem.

To achieve the goal of automatic and accurate registration of optical images and LiDAR data, it is worth to explore the appropriate algorithms from existing registration methods and develop new algorithms.

6. Acknowledgement

This research was funded by the Canada Research Chairs Program.

7. References

Alhichri, H. S., and Kamel, M. (2003). Virtual circles: A new set of features for fast image registration. *Pattern Recognition Letter*, vol. 24, no. 9/10, pp. 1181–1190, Jun.

Antonarakis, A.S., Richards, K.S. and Brasington,J. (2008). Object-based land cover classification using airborne LiDAR, *Remote Sensing of Environment*, Volume 112, Issue 6, Pages 2988-2998, ISSN 0034-4257.

Baltsavias, E. (1999). A comparison between photogrammetry and laser scanning. *ISPRS Journal of Photogrammetry & Remote Sensing*, 54(1):83–94.

Brenner, C. (2005). Building reconstruction from images and laser scanning. *International Journal of Applied Earth Observation and Geoinformation*, 6(3–4): 187–198.

Castro, E., and Morandi, C. (1987). Registration of translated and rotated images using finite Fourier transforms. *IEEE Transactions of Pattern Analysis and Machine Intelligence*, vol. PAMI-9, no. 5, pp. 700–703, Sep.

Cooley, J., and Tukey, J. (1965.) An algorithm for the machine calculation of complex Fourier series. *Mathematics of Computations*, vol. 19, no. 90, pp. 297–301, April.

Cui, L.L., Tang, P., and Zhao Z.M. (2006). Study on object-oriented classification method by integrating various features. *Journal of Remote Sensing*, 10(1), pp. 104-110.

Deng, F., Hu, M., and Guan, H. (2008). Automatic registration between LiDAR and digital images, *International Archives of photogrammetry, Remote Sensing and Spatial Information Sciences*, 37(B1):487–490

Fischler, M. A. and Bolles, A. C. (1981). Random sample consensus: A paradigm for model fitting with applications to image analysis and automated cartography. *Communications ACM*, vol. 24, no. 6, pp. 381–395, Jun.

Habib, A., Ghanma, MS., Morgan, MF., and Mitishita, EA. (2004). Integration of laser and photogrammetric data for calibration purposes. *International Archives of XXth ISPRS Congress,*12-23 July 2004 Istambul, Turkey, Commission I.

Habib, A., and Schenk, T. (1999). New approach for matching surfaces from laser scanners and optical sensors. *International Archives of Photogrammetry and Remote Sensing*, 32(3W14):55-61.

Habib, A., M. Ghanma, M. Morgan, and R. Al-Ruzouq. (2005). Photogrammetric and LiDAR data registration using linear features, *Photogrammetric Engineering & Remote Sensing*, 71(6):699–707.

Habib, A., Shin, S., Kim, C., and Al-Durgham, M. (2006). Integration of photogrammetric and LiDAR data in a multi-primitive triangulation environment. *Innovations in 3D Geo Information Systems,* Springer, Berlin, Part 2, pp.29–45.

Haitao, LI., Haiyan, GU., and Jinghui YANG. (2007). Fusion of High-Resolution Aerial Imagery and LiDAR data for Object-oriented Urban Land-Cover Classification, *ISPRS Workshop on Updating Geo-spatial Databases with Imagery & The 5the ISPRS Workshop on DMGISs*, Urumchi, Xingjiang, China.

Harris, C., and Stephens, M. (1988). A combined corner and edge detector. in *Proc. 4th ALVEY Vis. Conf.*, pp. 147–151.

Itti, L., Koch, C., and Niebur, E. (1998). Amodel of saliency-based visual attention for rapid scene analysis. *IEEE Transactions of Pattern Analysis and Machine Intelligence*, vol. 20, no. 11, pp. 1254–1259, Nov.

Kadir, P., and Brady, M. (2001). Saliency, scale and image description. *International Journal of Computer Vision*, vol. 45, no. 2, pp. 83–105, Nov.

Kim, C., Ghanma, M., and Habib, A. (2006). Integration of Photogrammetric and LIDAR data for realistic 3D model generation, [Online]. Available from: http://regard.crg.ulaval.ca/2006/proceedings/13-kim_et_al.pdf [Accessed 27 October 2011].

Kwak, T.-S., Kim, Y., Yu, K.-Y., and Lee, B.-K. (2006). Registration of aerial imagery and aerial LiDAR data using centroids of plane roof surfaces as control information. KSCE J. Civil Eng., vol. 10, no. 5, pp. 365–370, Sep.

Lindeberg, T. (1998). Feature detection with automatic scale selection. *International Journal of Computer Vision.* vol. 30, no. 2, pp. 77–116, Nov.

Lowe, D. G. (2004). Distinctive image features from scale-invariant key-points. *International Journal of Computer Vision*, vol. 60, no. 2, pp. 91–110, Nov.

Mastin, A., Kepner, J. Fisher, J. (2009). Automatic registration of LIDAR and optical images of urban scenes. *Computer Vision and Pattern Recognition, 2009. IEEE Conference*, vol., no., pp.2639-2646, 20-25 June.

Noble, A. (1989). Descriptions of image surfaces, Ph.D. dissertation, Oxford Univversity, Oxford, U.K., 1989.

Palenichka, R. M. and Zaremba, M. B. (2010). Automatic extraction of control points for the registration of optical satellite and LiDAR images. *IEEE Transactions of Geosciences and Remote Sensing*. 48(7), pp. 2864-2879.

Palenichka, R. M., and Zaremba, M. B. (2005). Object shape extraction based on the piecewise linear skeletal representation, in *Proc. Int. Conf. ICIAR*, vol. 3656, *LNCS*, pp. 464–472.

Park, J.Y., Shrestha, R.L., Carter, W.E., and Tuell, G.H. (2001). Land-cover classification using combined ALSM (LIDAR) and color digital photography. *Presented at ASPRS conference,* St. Louis, Missouri, April, pp. 23-27.

Postolov, Y., Krupnik, A., and McIntosh. K. (1999). Registration of airborne laser data to surfaces generated by photogrammetric means. *International Archives of Photogrammetry and Remote Sensing*, 32(3W14):95-99.

Reddey, B,. Srinivasa, and Chatterji, B.N. (1996). An FFT-Based Technique for Translation, Rotation, and Scale-Invariant Image Registration. *IEEE Transactions on Image Processing*, Vol. 5., No. 8, August.

Reddy, B., and Chatterji, B. (1996). An FFT-based technique for translation, rotation, and scale-invariant image registration. *IEEE Transaction of Image Processing*, vol. 5, no. 8, pp. 1266–1271, Aug. 1996.

Reisfeld, D., Wolfson, H., and Yeshurun, Y. (1995). Context-free attentional operators: The generalized symmetry transform. *International Journal of Computer Vision*, vol. 14, no. 2, pp. 119–130, Mar.

Rottensteiner, F., Jansa, J. (2002). Automatic extraction of building from LIDAR data and aerial images. *In: Proc. Internat. Society for Photogrammetry and Remote Sensing*, vol. 34, No. 4, pp. 295–301.

Schenk, T., Csatho, B. (2002). Fusion of Lidar data and aerial imagery for a more complete surface description. *In: ISPRS. Photogrammetry and Computer Vision*, Graz, Austria, 9–13 September, pp. A-310 ff.

Sebe, N., and Lew, M. S. (2003). Comparing salient point detectors. *Pattern Recognition Letters*, vol. 24, no. 1–3, pp. 89–96, Jan.

Shenk, T., and Castho, B. (2002). Fusion of LiDAR data and aerial imagery for a more complete surface description. *ISPRS International Archives*, vol. 34, no. 3A, pp. 310–331.

Shorter, N., Kasparis, T. (2008). Autonomous Registration of LiDAR Data to Single Aerial Image. *Geoscience and Remote Sensing Symposium, 2008. IGARSS 2008. IEEE International*, vol.5, no., pp.V-216-V-219, 7-11 July.

Syed, S., Dare, P. and Jones, S. (2005). Automatic classification of land cover features with high resolution imagery and lidar data: an object-oriented approach. *Proceedings of SSC2005 Spatial Intelligence, Innovation and Praxis: The national biennial Conference of the Spatial Sciences Institute*, Sept.

Tagare, H. D., Toyama, K., and Wang, J. G. (2001). A maximum-likelihood strategy for directing attention during visual search *IEEE Transactions of Pattern Analysis and Machine Intelligence*, vol. 23, no. 5, pp. 490–500, May.

Viola, p., Wells, W. (1997). Alignments by maximization of mutual information. *International Journal of Computer Vision*, 24(2): 137-154

Wong, A., Orchard, J. (2008). Efficient FFT-Accelerated Approach to Invariant Optical–LIDAR Registration, *Geoscience and Remote Sensing, IEEE Transactions on*, vol.46, no.11, pp.3917-3925, Nov.

Wu, H., Li, Yong., Li, J., and . Gong, J. (2010). A Two-step Displacement Correction Algorithm for Registration of LiDAR Point Clouds and Aerial Images without Orientation Parameters, *Photogrammetric Engineering & Remote Sensing*, 76(10):1135–1145.

Zavorin, I., and Le Moigne, J. (2005). Use of multiresolution wavelet feature pyramids for automatic registration of multisensor imagery. *IEEE Transaction of Image Processing*, vol. 14, no. 6, pp. 770–782, Jun.

Zheng, Z. Wang, H. and Teoh, E. K. (1999). Analysis of gray level corner detection. *Pattern Recognition Letters*, vol. 20, no. 2, pp. 149–162, Feb.

Zitova, B. and Flusser, J. (2003). Image registration methods: A survey. *Image and Vision Computing.* vol. 21, no. 11, pp. 977–1000.

Xiong Z., and Zhang, Y. (2010). A critical review of image registration methods. *International Journal of Image and Data Fusion*, 1, pp. 137–158

Meaning of Open Access

In accordance with major definitions of open access in scientific literature (namely the Budapest, Berlin, and Bethesda declarations), MDPI defines *open access* by the following conditions:

- peer-reviewed literature is freely available without subscription or price barriers,
- literature is immediately released in open access format (no embargo period), and
- published material can be re-used without obtaining permission as long as a correct citation to the original publication is given.

Open Access Explained!

Until 2008, most articles published by MDPI contained the note: "© *year* by MDPI (http://www.mdpi.org). Reproduction is permitted for noncommercial purposes". During 2008, MDPI journals started to publish articles under the Creative Commons Attribution License and are now using the latest version of the CC BY license, which grants authors the most extensive rights. All articles published by MDPI before and during 2008 should now be considered as having been released under the post-2008 Creative Commons Attribution License.

http://www.mdpi.com/about/openaccess

Curriculum Vitae

Candidate's full name: Rakesh Kumar Mishra

Universities attended:

2009-Present PhD Candidate, University of New Brunswick, NB, Canada

2005, MCA, Computer Science, UP Technical University, UP, India

2000, BSc, Mathematics and Physics, University of Allahabad, UP, India

Publications:

Mishra, R. K., & Zhang, Y. (2017). Effects of industry adopted fusion methods on pan-sharpening WorldView-3 short wave infrared (SWIR) imagery, Journal of Applied Remote Sensing – Letters (under review).

Mishra, R. K., & Zhang, Y. (2017). Solar photovoltaic panel detection using WorldView-3 satellite imagery, Journal of Photogrammetric Engineering & Remote Sensing (under review).

Mishra, R. K., & Zhang, Y. (2017). Roofing material detection using WorldView-3 satellite imagery, International Journal of Remote Sensing (under review).

Zhang, Y., Roshan, A., Jabari, S., Khiabani S.A., Fathollahi, F., & **Mishra, R.K.** (2016). Understanding the quality of pansharpening-A Lab Study. *Photogrammetric Engineering & Remote Sensing*, 82 (10), 748–755.

Zhang, Y., & **Mishra, R. K.** (2014). From UNB PanSharp to FuzeGo — the success behind the pan-sharpening algorithm, *International Journal of Image and Data Fusion*, Vol. 5, No.1, pp. 39-53

Mishra, R. K., & Zhang, Y. (2012). A review of optical imagery and airborne LiDAR data registration methods, *The Open Remote Sensing Journal*. vol. 5, pp. 54-63, 2012.

Mishra, R.K., and Zhang, Y. (2012). Object-Oriented Approach for Remote Sensing Image Processing using Java Advanced Imaging, *Journal of Earth Science and Engineering*, Vol. 2 Issue 5, p302.

Mishra, R.K., & Zhang, Y. (2013). Moving target detection using single pass WorldView-2 satellite imagery. *Proceedings of ASPRS 2013 Annual Conference*, Baltimore, Maryland, March 24-28.

Mishra, R.K. & Y. Zhang (2013): Remote sensing image processing using Java Advanced Image (JAI). Proc. of ASPRS 2013 *Annual Conference, Baltimore,* Maryland, March 24-28.

Mishra, R. K. (2012). Automatic moving vehicle information extraction from one-pass worldview-2 satellite imagery, *Int. Arch. Photogramm. Remote Sens. Spatial Inform. Sci.*, vol. XXXIX-B7, pp.323 -328 2012

Zhang, Y., & **Mishra, R. K.** (2012). A Review and Comparison of Commercially Available Pan-Sharpening Techniques for High Resolution Satellite Image Fusion, *IEEE International Geoscience and remote sensing Symposium*, 22-27 Jul.

Mishra, R. K., Zhang, Y. (2012). Moving Vehicle Extraction from One-Pass WorldView-2 Satellite Imagery, *GSDI Conference* -2012, 13-17 May.

Lohani, B., & **Mishra, R. K.**, (2009). LAS and LASUtility, GIM International, Volume 23, Issue 8, August.

Lohani, B., **Mishra, R. K.**, & Biswas S. (2008). Development of airborne altimetric LiDAR simulator and its evaluation, ISPRS Archive of XXI ISPRS congress, Beijing, China, 3-11 July.

Mishra, R. K., Lohani, B. (2007). An object-oriented software development approach to design simulator for airborne altimetric LiDAR, *National conference on emerging trends in information technology 2007,* SGSITS Indore, India, December 18-20.

Mishra, R. K., Lohani, B. (2007). The reality behind a LiDAR simulator, *Geospatial Today*, November, pp 45-49.

Lohani, B., **Mishra, R. K.** (2007). Generating LiDAR data in laboratory: LiDAR simulator, *International Archive of Photogrammetry and Remote Sensing, XXVI(3)W52 of Laser Scanning 2007 and SilviLaser 2007, Espoo,* Finland, September 12-14.

Lohani, B., Reddy, P., & **Mishra, R. K.** (2006). Airborne Altimetric LiDAR Simulator: An education tool, *International Archives of the Photogrammetry, Remote Sensing and Spatial Information Science, XXXVI(6),* Tokyo, Japan.

Conference Presentations:

Mishra, R. K., & Zhang Y. (2014). Performance Evaluation of Pan-sharpening techniques on HR Satellite imagery, *ASPRS 2014 Annual Conference*, Louisville, Kentucky USA, March 23-28.

Mishra, R. K., and Zhang, Y. (2014). Advanced Image Processing Using Image I/O-Ext and Java Advanced Imaging (JAI), *ASPRS 2014 Annual Conference*, Louisville, Kentucky USA, March 23-28.

Mishra, R.K., & Zhang, Y. (2013). Moving target detection using single pass WorldView-2 satellite imagery. *Proceedings of ASPRS 2013 Annual Conference*, Baltimore, Maryland, March 24-28.

Mishra, R.K., & Zhang, Y. (2013). A comparison of commercial Pan-sharpening techniques for HR Satellite imagery. *ESRI International User Conference*, San Diego, CA, July 8-12.

Mishra, R.K. & Y. Zhang (2013): Remote sensing image processing using Java Advanced Image (JAI). Proc. of ASPRS 2013 *Annual Conference, Baltimore*, Maryland, March 24-28.

Zhang, Y., & **Mishra, R. K.** (2012). A Review and Comparison of Commercially Available Pan-Sharpening Techniques for High Resolution Satellite Image Fusion , *IEEE International Geoscience and remote sensing Symposium*, 22-27 Jul.

Mishra, R. K., & Zhang, Y. (2012). Moving Vehicle Extraction from One-Pass WorldView-2 Satellite Imagery, *GSDI Conference* -2012, 13-17 May.

Mishra, R. K., & Zhang, Y. (2012), Automatic vehicle detection and speed computation from one-pass WorldView-2 imagery, *GSDI Conference* -2012, 13-17 May.

Mishra, R. K., & Zhang, Y. (2011). Object-oriented approach for remote sensing image processing using Java Advanced Imaging, *32 Canadian Symposium on Remote Sensing-2011*, 13-16 June.

Mishra, R. K., Zhang, Y. (2010). Component-Based Software Design for Image Processing, *Geomatics Atlantic-2010*, 28-29 October.

Lohani, B., **Mishra, R. K.**, & Biswas, S. (2008). Limulator2.0: A simulator for LiDAR Education, *The XXI Congress, The International Society for Photogrammetry and Remote Sensing*, 3-11 July, Beijing, China (**Own Silver Award**).

Lohani, B., **Mishra, R. K.**, & Biswas S. (2008). Development of airborne altimetric LiDAR simulator and its evaluation, ISPRS Archive of XXI ISPRS congress, Beijing, China, 3-11 July.

Mishra, R. K., Lohani, B. (2007). An object-oriented software development approach to design simulator for airborne altimetric LiDAR, *National conference on emerging trends in information technology 2007*, SGSITS Indore, India, December 18-20.

Mishra, R. K., Lohani, B. (2007). Object oriented software engineering for designing an aerial survey LiDAR, *Spatial India 2007-IT and GIS strategy for infrastructure*, Jaipur, INDIA, October 25-26.

Lohani, B., **Mishra, R. K.** (2007). Generating LiDAR data in laboratory: LiDAR simulator, *International Archive of Photogrammetry and Remote Sensing, XXVI(3)W52 of Laser Scanning 2007 and SilviLaser 2007, Espoo,* Finland, September 12-14.

Lohani, B., **Mishra, R. K.** (2007). Modeling airborne altimetric LiDAR system to simulate data capture process, *Proc. Of GI Forum International Conference*, 3 – 6 July, 2007, Salzburg, Austria. (**Poster rated among 10 best papers**).

Lohani, B., Reddy, P., & **Mishra, R. K.** (2006). Airborne Altimetric LiDAR Simulator: An education tool, *International Archives of the Photogrammetry, Remote Sensing and Spatial Information Science, XXXVI(6)*, Tokyo, Japan.